Title
Cross-activating c-Met/β1 integrin complex drives metastasis and invasive resistance in cancer

Author
Jahangiri, Arman

Publication Date
2018

Peer reviewed|Thesis/dissertation

Cross-activating c-Met/β1 integrin complex drives metastasis and invasive resistance in cancer

by

Arman Jahangiri

DISSERTATION

Submitted in partial satisfaction of the requirements for the degree of

DOCTOR OF PHILOSOPHY

in

Biomedical Sciences

in the

GRADUATE DIVISION

of the

UNIVERSITY OF CALIFORNIA, SAN FRANCISCO

COPYRIGHT

ACKNOWLEDGEMENTS

I owe a great deal of gratitude to a number people during my time in San Francisco. What started out as a Howard Hughes Medical Institute fellowship for a medical student who could hardly run a western blot, soon transitioned to a scientific journey of understanding molecular interactions in cells that were a death sentence to patients just on the other side of the city. I am forever indebted to both of my mentors and principle investigators Dr. William A. Weiss, and Dr. Manish K. Aghi for their continuous support and unending love, working with me to create a nontraditional trajectory that may have not been the most fruitful for their individual labs. I learned a great deal from both of my mentors and hope to be able to follow in their footsteps as I march forward towards my goal of becoming a physician scientist.

There were a number of mentors at the bench that showed me the ropes on my path to becoming a true scientist. I want to especially thank Dr. Kan Lu who always answered my questions and was patient with me during my time at the lab. I want to thank Mike De Lay, who was my best friend in the lab for two years and really supported me to follow my dreams of obtaining my PhD. Lastly, I want to thank Maxim K Sidorov, who volunteered in the lab, working 12-14 hours a day, 7 days a week for over two years and helped me geek-out about science and make this project become a reality.

The support of my father Jim, my mother Zary, and my brother Allen were central in my success as I left Texas and medical school to embark on my journey of becoming a scientist. Their patience, endless love, and continuous support while I delayed medical school graduation for 6 years gave me hope and the strength necessary to keep my head up. Through their love, I was continuously reminded that *Finis Coronat Opus*, the end crowns the work every time I was discouraged. Their sacrifice will not be forgotten and I hope that I can one day repay them with my future success.

ABSTRACT

Cross-activating c-Met/β1 integrin complex drives metastasis and invasive resistance in cancer

By

Arman Jahangiri

The molecular underpinnings of invasion, a hallmark of cancer, have been defined in terms of individual mediators but crucial interactions between these mediators remain undefined. In xenograft models and patient specimens, we identified a c-Met/β1 integrin complex that formed during significant invasive oncologic processes: breast cancer metastases and glioblastoma invasive resistance to antiangiogenic VEGF neutralizing antibody, bevacizumab.

Inducing c-Met/β1 complex formation through an engineered inducible heterodimerization system promoted features crucial to overcoming stressors during metastases or antiangiogenic therapy: migration in the primary site, survival under hypoxia, and extravasation out of circulation. c-Met/β1 complex formation was up-regulated by hypoxia, while VEGF binding VEGFR2 sequestered c-Met and β1 integrin, preventing their binding.

Complex formation promoted ligand-independent receptor activation, with integrin-linked kinase phosphorylating c-Met and crystallography revealing the c-Met/β1 complex to maintain the high-affinity β1 integrin conformation. Site-directed mutagenesis verified the necessity for c-Met/β1 binding of amino acids predicted by crystallography to mediate their extracellular interaction. Far-Western blotting and sequential immunoprecipitation revealed that c-Met displaced α5 integrin from β1 integrin, creating a complex with much greater affinity for fibronectin (FN) than α5β1. Thus, tumor cells adapt to microenvironmental stressors induced by metastases or bevacizumab by co-opting receptors, which normally promote both cell migration modes: chemotaxis, movement toward concentrations of environmental chemoattractants, and haptotaxis, movement controlled by the relative strengths of peripheral adhesions. Tumor cells then redirect these receptors away from their conventional binding partners, forming a powerful structural c-Met/β1 complex whose ligand-independent cross-activation and robust affinity for FN drive invasive oncologic processes.

TABLE OF CONTENTS

LIST OF TABLES

LIST OF FIGURES

CHAPTER 1

INTRODUCTION

Invasion is a major cause of cancer mortality, as exemplified by metastatic spread of systemic malignancies or local intracranial invasion of glioblastoma. While individual mediators of invasion are identified, functional or structural interactions between these mediators remain undefined. We identified a structural cross-activating c-Met/β1 integrin complex that promotes breast cancer metastases and invasive resistance of glioblastoma to the antiangiogenic therapy bevacizumab. We show that tumor cells adapt to their microenvironmental stressors by usurping c-Met and β1 integrin, with c-Met displacing α5 integrin from β1 integrin to form a c-Met/β1 complex with far greater fibronectin affinity than α5β1 integrin. These findings challenge conventional thinking about integrin–ligand interactions and define a molecular target for disrupting metastases or invasive oncologic resistance.

Cooperation between integrins and receptor tyrosine kinases (RTKs) contributes to migration in normal and cancer cells. Previous studies have demonstrated colocalization of RTK c-Met with α5 or β1 integrin (1, 2) but the mechanisms and biologic consequences of these interactions remain undetermined. Invasion of tumor cells is directed by haptotaxis, cellular locomotion in response to concentration gradients of adhesive molecules in the extracellular matrix (ECM), and chemotaxis, cellular locomotion in response to concentration gradients of diffusible factors. Given the

ability of integrins and c-Met to mediate haptotaxis and chemotaxis, respectively, these complementary functions suggest that interaction between c-Met and integrins could have a significant biologic impact on tumor cell migration.

While chemotactic c-Met and haptotactic integrins like α5 or β1 each contribute individually to tumor cell migration, the mechanism through which they interact to regulate migration and the specific aspects of cancer cell biology that rely on their interaction remain uncertain. Here, we demonstrate that c-Met and β1, not α5, integrin interact physically and functionally during two invasive cancer processes: metastases, the cause of 90% of cancer deaths (3), and glioblastoma (GBM) resistance to VEGF neutralizing antibody bevacizumab, a common occurrence after short-lived response to this agent (4-9).

CHAPTER 2

c-Met/β1 COMPLEX IN BREAST CANCER

Physical Interaction Between c-Met and β1 Integrin Increases During Metastases

To determine which integrins interacted with c-Met in breast cancer cells, we performed a Western blot in cultured HCC1143, HCC3153, and MDA-MB-231 human breast adenocarcinoma cells, which revealed that c-Met was expressed in all three lines, while, of a panel of screened integrins, αV, α3, α5, β1, β3, and β5 integrins were expressed in all three lines **(Appendix A, Figures S1 and S2).** Immunoprecipitation then revealed that, of these six integrins, β1 integrin was the most oncologically pertinent one (5, 10) that bound c-Met in all three lines (**Figure 1A and Appendix A, Figure S3)**.

To determine if this c-Met/β1 integrin interaction increased during metastases, we implanted MDA-MB-231 cells into the mammary fat pads of immunodeficient mice (n = 5), after which spontaneous metastases arose in one mouse. Using proximity ligation assays (PLAs), we detected c-Met/β1 integrin complex formation at the invasive front in all four primary tumors, particularly in the primary tumor with gross metastases **(Figure 1B and Appendix A, Figure S4)**. PLA revealed more signal (red dots indicative of c-Met/β1 integrin complex) in gastric **(Figure 1C and Appendix A, Figure S5)** and **brain (Figure 1C and Appendix A, Figure S6)** metastases relative to the primary tumor that metastasized, with quantification revealing more than double the amount of PLA signal

in the gastric metastasis (P = 0.0006) and nearly fivefold more PLA signal in the brain metastasis (P = 0.01) relative to the primary tumor (Figure 1D). Similarly, immunoprecipitation (IP) of lysates from MDA-MB-231-BR, an MDA-MB231 derived cell line selected through serial propagation in vivo for its propensity for brain metastases (11), exhibited greater c-Met/β1 integrin complex in culture than MDA-MB-231 cells **(Figure 1E)**, suggesting durability of the complex within the metastatic phenotype.

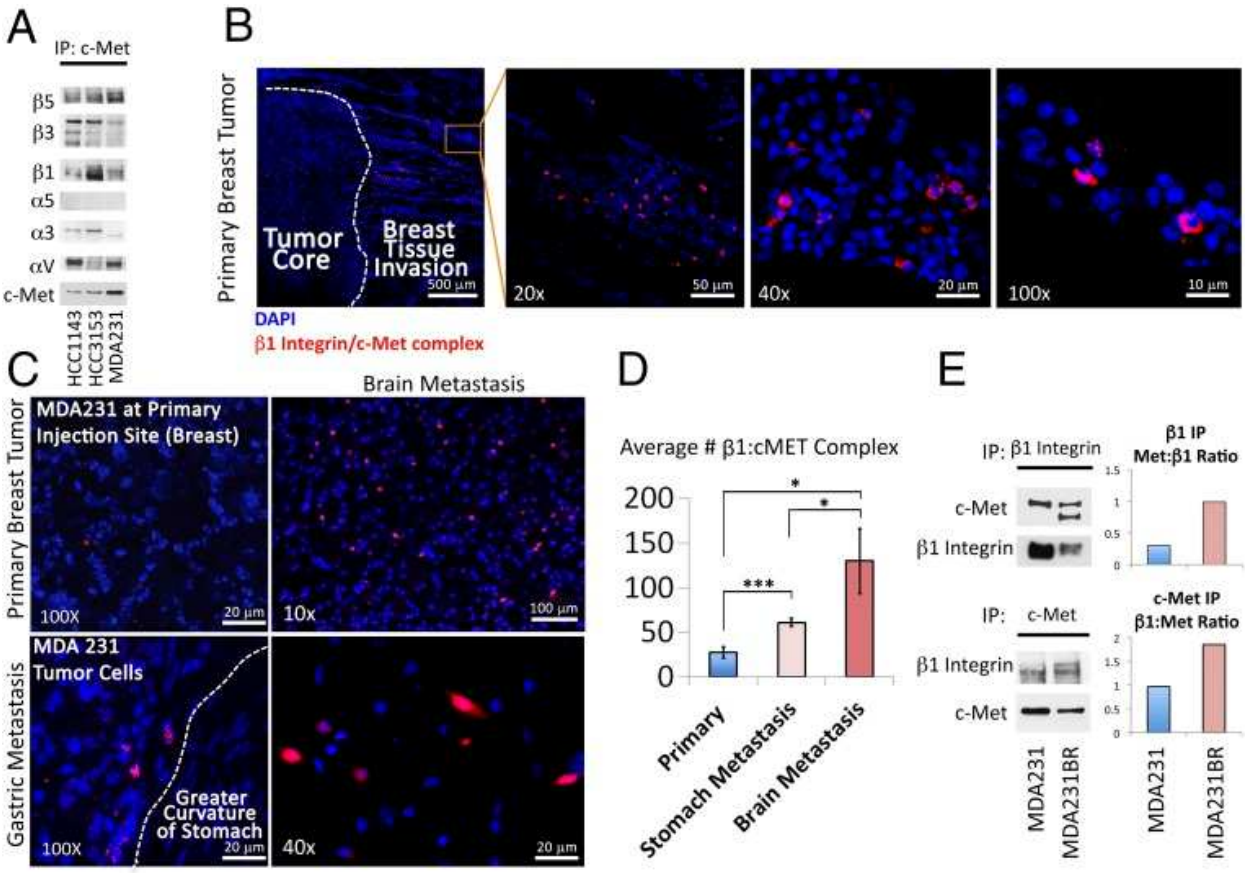

Figure 1: A c-Met/β1 integrin complex forms in breast cancer metastases in a xenograft model. (*A*) c-Met IP of HCC1143, HCC3153, and MDA-MB-231 breast cancer cells to assess binding of ubiquitously expressed integrins (see ***Appendix A*, Figure S2** for Western blot of full integrin panel in all three lines) to c-Met in each cell line. **(*B*)** PLA revealed c-Met/β1 integrin complex formation at the invasive edge of a

MDA-MB-231 mammary pad xenograft. **(*C*)** Representative PLA images of c-Met/β1 complexes in the primary mammary pad tumor (*Upper Left*), gastric metastasis (*Lower Left*), and brain metastasis (*Upper* and *Lower Right*). **(*D*)** Quantification revealed over double the number of PLA signals per 100× field in the gastric metastasis ($P = 0.0006$) and nearly fivefold more signal in the brain metastasis ($P = 0.01$) versus primary tumor ($n = 4$ fields per tumor). **(*E*)** c-Met and β1 integrin IPs each revealed more c-Met/β1 integrin complex in cultured MDA-MB-231-BR brain-seeking cells versus MDA-MB-231 cells. *$P < 0.05$; ***$P < 0.001$.

The c-Met/β1 Complex Promotes Breast Cancer Cell Migration

In order to establish whether the c-Met/β1 complex detected in metastases promotes tumor cell motility, we engineered MDA-MB-231 cells to express β1 integrin and c-Met fused to FRB (DmrC) and FKBP (DmrA), respectively, creating MDA-MB-231-iDimerize-c-Met-β1 cells, which enabled us to increase c-Met/β1 complex formation using AP21967 (A/C ligand heterodimerizer), a derivative of rapamycin (12) **(Figure 2 A and B and Appendix A, Figures S7 and S8)**. AP21967 treatment changed morphology of MDA-MB-231-iDimerize-c-Met-β1 cells by giving rise to extensive protrusions emanating from the cytoplasm, pushing the cells toward the stellate morphology that is seen in invading mesenchymal cells (13), as evidenced by decreased circularity shape factor ($P = 6 \times 10{-}7$) **(Figure 2C)**. Consistent with altered morphology being conducive to increased cell migration, AP21967 increased motility of MDA-MB231-iDimerize-c-Met-β1 cells in scratch assays ($P = 0.001$ at 5 hrs, $P = 0.02$ at 24 hrs) **(Figure 2D)** and increased invasion in Matrigel chambers ($P = 0.007$) **(Figure 2E and Appendix A, Figure S9).**

We then determined if inducing c-Met/β1 integrin binding promoted extravasation of MDA-MB-231 cells out of the circulation, a crucial step of the metastatic cascade. MDA-MB-231-iDimerize-cMet-β1 cells were preincubated with AP21967 for 2 hrs and

then injected i.v. via tail vein injection. Animals were killed 2 hrs and 7 days after injection, with increased human MDA-MB-231-iDimerize-c-Met-β1 cells detected in the lungs of mice receiving cells that were pretreated with AP21967 by two independent methods: immunostaining the lungs for human vimentin and PCR for the FKBP-c-Met fusion sequences, which would be unique to the implanted tumor cells. Two hours after tail vein injection of tumor cells, lung immunostaining revealed increased human vimentin staining when injecting cells pretreated with AP21967 versus those pretreated with vehicle (P = 0.02; **Figure 2F** and **Appendix A, Figure S10**) and PCR for the FKBP-cMet fusion sequences revealed no detectable signal in all mice receiving cells pretreated with vehicle, compared with consistent signal in all mice receiving cells pretreated with AP21967 **(Figure 2F)**. Seven days after tail vein injection of cells, there was increased lung human vimentin staining relative to 2 hrs when injecting cells pretreated with AP21967 compared with no detectable staining when injecting cells pretreated with vehicle (**Figure 2G** and **Appendix A, Figure S11**). PCR at this 7-day time point revealed dramatic increase in the FKBP-c-Met fusion sequence transcript in all mice 7 days after receiving cells pretreated with AP21967 while only two of five mice receiving cells pretreated with vehicle had detectable transcript at this time point **(Figure 2G).** Thus, while baseline MDA-MB-231 cells failed to establish metastases

after initial circulatory passage through the lungs, inducing c-Met/β1 integrin complex formation in these cells caused them to reliably establish pulmonary metastasis.

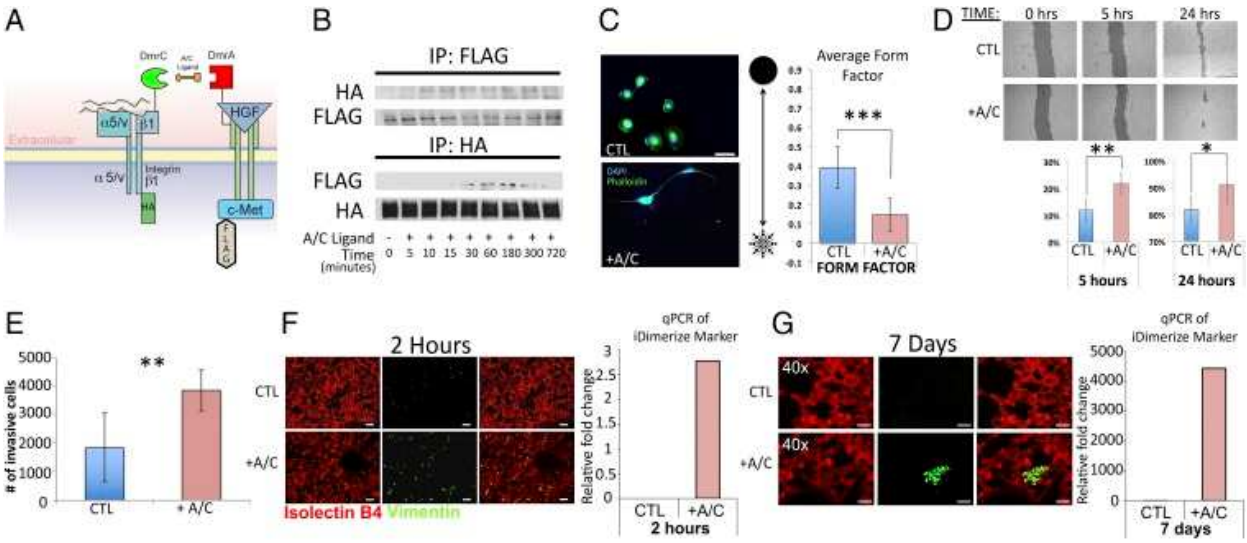

Figure 2. Inducing c-Met/β1 integrin binding in breast cancer cells increases tumor cell migration and extravasation out of circulation. **(*A*)** MDA-MB-231 cells were engineered to express HA-tagged β1 integrin and FLAG-tagged c-Met fused to FRB (DmrC) and FKBP (DmrA), respectively, and treated with AP21967 (A/C heterodimerizer) to induce c-Met/β1 binding. **(*B*)** MDA-MB-231-iDimerize-c-Met-β1 cells were treated with AP21967 or vehicle (control), after which HA and FLAG IP confirmed that AP21967 induces c-Met/β1 binding. **(*C*)** MDA-MB-231-iDimerize-c-Met-β1 cells were assessed for morphology via a form factor plugin on ImageJ, revealing decreased circularity shape factor after AP21967 treatment ($P = 6 \times 10^{-7}$; $n = 12$ cells per group). **(*D*)** MDA-MB-231-iDimerize-c-Met-β1 cells were scratched at time = 0 and assessed after 5 and 24 h via mosaic imaging and analyzed using T-Scratch software to confirm that AP21967 induced migration ($P = 0.001$ at 5 h, $P = 0.02$ at 24 h) ($n = 8$ per group). **(*E*)** AP21967 also increased MDA-MB-231-iDimerize-c-Met-β1 invasion in Matrigel ($n = 6$ per group; $P = 0.007$). **(*F*)** MDA-MB-231-iDimerize-c-Met-β1 cells were pretreated for 2 h with or without AP21967, followed by tail vein injection into NSG mice ($n = 6$ mice per group). After 2 h, mice receiving AP21967-pretreated cells exhibited more human vimentin staining by immunohistochemistry versus those pretreated with vehicle, as shown in representative images here and quantified in ***Appendix A*, Figure S9** ($P = 0.02$), with qPCR revealing the FKBP–c-Met fusion sequence in lungs of all mice receiving AP21967-pretreated cells, with the lack of PCR signal in all vehicle-treated

mice precluding statistical comparison. **(*G*)** Analysis of lungs from the same experiment as *F* at 7 days post injection revealed further increased human vimentin staining after tail vein injection of cells pretreated with AP21967 compared with no staining when injecting vehicle-pretreated cells (lack of staining in control group prevented statistical comparison). Similarly, qPCR at 7 days revealed increased tumor-specific FKBP–c-Met fusion sequence in mice receiving AP21967-treated cells, with lack of signal in most mice receiving vehicle-treated cells precluding statistical comparison. $*P < 0.05$; $**P < 0.01$; $***P < 0.001$.

CHAPTER 3

c-Met/β1 COMPLEX IN GLIOBLASTOMA

c-Met/β1 Complex Formation Increases During Invasive Resistance in Glioblastoma

Each organ has unique extracellular matrix milieus that could be variably receptive to invasion by tumor cells with c-Met/β1 integrin complex formation. Due to the particularly significant levels of c-Met/β1 integrin complex we noted in brain metastases **(Figure 1 C and D and Appendix A, Figure S6)**, we investigated the role of the c-Met/β1 complex in the invasiveness of GBM, the most common malignant primary brain tumor. Unlike other aggressive cancers, GBM does not metastasize but rather invades locally. Because resistance to the antiangiogenic agent bevacizumab is a common driving event promoting transformation of GBM to a highly invasive phenotype, we investigated the role of the c-Met/β1 complex in bevacizumab resistance in GBM.

We analyzed c-Met/β1 complex formation in two GBM xenograft models of bevacizumab resistance created by our group. Our first model transfers the effects of prolonged antiangiogenic therapy directly from the patient to the mouse in the form of patient-derived xenografts (PDXs) that maintain the sensitivity or resistance to bevacizumab found in the patient tumor they derive from, while our second model recapitulates prolonged antiangiogenic therapy in mice. In the first model, bevacizumab caused a 5-fold increase in c-Met/β1 complex formation by PLA in intracranial resistant

PDXs (SF7796) (P = 0.003), while bevacizumab also increased c-Met/β1 complex formation in intracranial responsive PDXs (SF7227 or SF7300) (P = 0.004–0.02), but by a lesser 2- to 3-fold factor **(Figure 3A and Appendix A, Figure S12)**. The second model involved U87-BevR and U87-BevS, isogeneic models of invasive bevacizumab resistance and sensitivity, respectively, that we have described (5, 6)(5, 6). Similar to the PDX findings, immunoprecipitated lysates of intracranial xenografts revealed robust physical c-Met/β1 integrin interactions in resistant U87-BevR xenografts treated with bevacizumab, compared with the sensitive bevacizumab-treated U87-BevS xenografts, and to control IgG-treated U87-BevR or U87-BevS xenografts **(Figure 3B)**. We confirmed this complex formation using PLAs, which revealed that bevacizumab increased c-Met/β1 complex formation in U87-BevS (P = 0.02) and U87-BevR (P = 0.02) xenografts, but the 19-fold increase in U87-BevR xenografts was far greater than the 3-fold increase in U87- BevS xenografts **(Figure 3C)**. Formation of the c-Met/β1 complex therefore increased with bevacizumab resistance in both in vivo models. The models also offered insight into the time course of complex formation, as the smaller increases noted in responsive xenografts treated with bevacizumab until progressing could represent a precursor to entrenched resistance, while continued treatment of resistant xenografts led to a much more robust increase in complex formation.

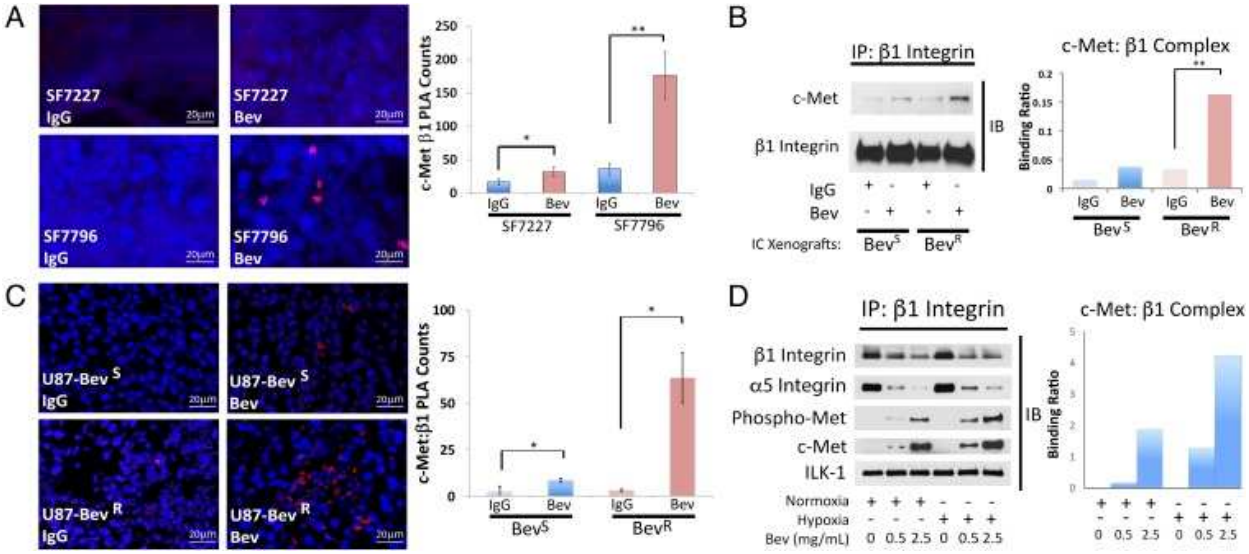

Figure 3. A c-Met/β1 complex forms in tumors that have evolved resistance to antiangiogenic therapy (*A*) PLAs of GBM PDXs revealed more c-Met/β1 complex with bevacizumab treatment of resistant PDX SF7796 (*P* = 0.003), with a lesser increase occurring with bevacizumab treatment of intracranial responsive PDXs (SF7227) (*P* = 0.02). IP **(*B*)** and PLA **(*C*)** of U87-Bev^S and U87-Bev^R intracranial xenografts treated with IgG or bevacizumab revealed increased c-Met/β1 complex with bevacizumab treatment, particularly in resistant xenografts (*P* = 0.003 U87-Bev^R IP; *P* = 0.02 PLA for U87-Bev^S and U87-Bev^R). **(*D*)** U87 cells were cultured with increasing bevacizumab concentrations in normoxia and hypoxia for 48 h (*Upper* row). Cell lysates were immunoprecipitated with β1 and blotted for total and phosphorylated c-Met to assess their binding to β1 (*Left*). The ratio of c-Met binding to immunoprecipitated β1 based on band intensities is in the graph. **P* < 0.05; ***P* < 0.01.

CHAPTER 4

THE COMPLEX AND THE TUMOR MICROENVIRONMENT

The c-Met/β1 Integrin Complex Is Driven by the Tumor Microenvironment

Bevacizumab depletes VEGF, resulting in decreased vascularity and hypoxia in resistant tumors (8). Thus, we analyzed the impact of VEGF depletion and hypoxia on c-Met/β1 integrin complex formation. Complex formation was increased in U87 GBM cells in a dosedependent manner by bevacizumab-induced depletion of all VEGF isoforms in culture **(Figure 3D and Appendix A, Figure S13)** and in vivo **(Appendix A, Figure S14)** and by hypoxia in culture **(Figure 3D and Appendix A, Figure S13)**, with VEGF depletion and hypoxia in combination cooperating to increase c-Met/β1 complex formation in cultured cells even further than either factor did individually **(Figure 3D)**.

We then investigated the impact of vascular factors that would be altered during antiangiogenic therapy on complex formation. We assessed the impact of conditioned medium (CM) from endothelial cells, which decrease in abundance after VEGF-targeted antiangiogenic therapy, on complex formation in tumor cells. CM from human umbilical vein endothelial cells (HUVECs) decreased complex formation in cultured U87 cells **(Figure 4A and Appendix A, Figure S15)**.

We then looked at how VEGF isoforms affect complex formation. While VEGF165, the predominant VEGF isoform, reduced complex formation, complex formation was not affected by VEGF189, an isoform that binds neuropilin-1 not

VEGFR2 (14), and VEGF165b, an isoform that binds VEGFR2 without activating downstream pathways (15) **(Figure 4B and Appendix A, Figures S16 and S17)**. Binding of integrin-linked kinase (ILK), a protein associated with the integrin cytoplasmic domain, and α5 integrin, the predominant β1 heterodimer partner, to β1 did not change under conditions in **Figure 4 A** and **B**, indicating that not all β1 binding partners were affected by these conditions. Formation of this complex thus occurs due to interactions among therapeutic stressors in the microenvironment, rather than by passive binding of up-regulated individual components.

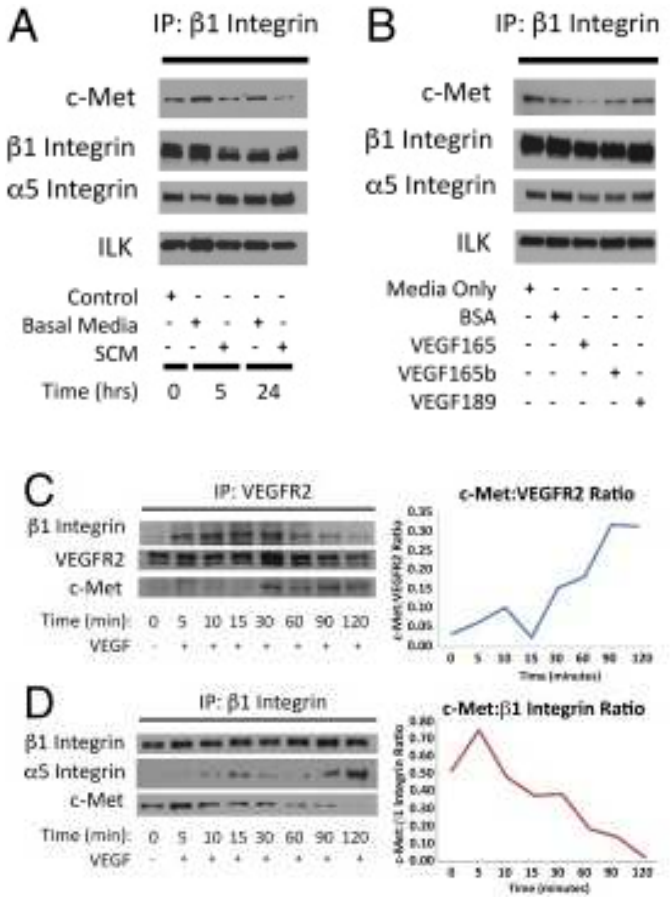

Figure 4. VEGF binding to VEGFR2 sequesters c-Met and β1 integrin, preventing c-Met/β1 integrin complex formation. (*A* and *B*) U87 cells were cultured in **(*A*)** conditioned media (CM) from HUVEC cells and **(*B*)** with 100 ng/mL of VEGF isoforms 165, 165b, and 189. c-Met/β1 complex formation was then analyzed via IP. (*C* and *D*) U87 cells were treated with 100 ng/mL VEGF and (*C*) VEGFR2 binding to β1 and c-Met and (*D*) β1 integrin binding to c-Met were analyzed by IP at various time points. (*E*) Proposed mechanism by which VEGF binding to VEGFR2 sequesters c-

E

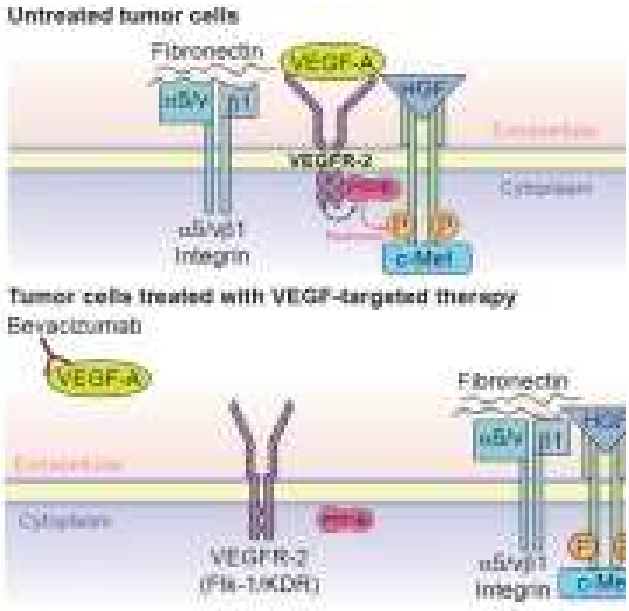

formation was then analyzed via IP. **(*C* and *D*)** U87 cells were treated with 100 ng/mL VEGF and **(*C*)** VEGFR2 binding to β1 and c-Met and **(*D*)** β1 integrin binding to c-Met were analyzed by IP at various time points. **(*E*)** Proposed mechanism by which various time points. **(*E*)** Proposed mechanism by which VEGF binding to VEGFR2 sequesters c-Met and β1 integrin, preventing c-Met/β1 complex formation.

VEGF Suppresses the c-Met/β1 Complex Through VEGFR2-Mediated Sequestration

To define the mechanism by which VEGF suppressed the formation of the c-Met/β1 integrin complex, we investigated the association of VEGFR2 with c-Met and β1 integrin. In cultured U87 cells, increasing duration of exposure to VEGF165 led to increased binding of VEGFR2 to β1 integrin and c-Met **(Figure 4C and Appendix A, Figure S18)** and reduced formation of the c-Met/β1 complex **(Figure 4D and Appendix A, Figure S18)**. These findings suggest that VEGF binding to VEGFR2 sequesters c-Met and β1 integrin, preventing them from binding to each other, while bevacizumab-induced VEGF depletion liberates c-Met and β1 integrin from VEGFR2, allowing them to form a complex **(Figure 4E)**.

The c-Met/β1 Integrin Complex Promotes GBM Cell Migration

To determine if the c-Met/β1 complex influences the GBM cell migration that defines resistance to antiangiogenic therapy, we utilized the same technology we employed in **Figure 2A** for engineering cells with inducible c-Met/β1 integrin heterodimerization. As described above, by expressing β1 and c-Met fused to FRB (DmrC) and FKBP (DmrA), respectively, in U87 and U251 GBM cells, we were able to induce c-Met/β1 complex formation using AP21967 (12) **(Appendix A, Figures S7 and S19–S21A)**. Complex induction with AP21967 led to increased c-Met phosphorylation, demonstrating that c-Met/β1 complex formation alone was sufficient for c-Met activation **(Appendix A, Figure S21B)**.

As with MDA-MB231 cells, complex induction with AP21967 affected U87 and U251 GBM cell morphology by decreasing circularity shape factor ($P = 1.6 \times 10^{-6}$, 2.1×10^{-7} **) (Appendix A, Figure S22A)**, giving rise to the stellate morphology (13) seen in invading mesenchymal cells and bevacizumabresistant GBM cells (5). Furthermore, complex induction with AP21967 increased migration ($P = 0.006$ at 5 and 25 h; **Appendix A, Figure S22B**) and invasion ($P = 0.004$–0.007; **Appendix A, Figure S22C**) but not proliferation ($P = 0.2$; **Appendix A, Figure S23A**) in GBM cells. Complex induction with AP21967 also promoted tumor cell survival in the hypoxia, but not the

nutrient deprivation, associated with antiangiogenic therapy (three way ANOVA: P = 0.008 for AP21967–hypoxia interaction, P = 0.4 for AP21967-nutrient deprivation interaction; **Appendix A, Figure S23B**).

These findings suggest that the c-Met/β1 complex contributes to migration and adaptation to the stress of devascularization in tumors that become resistant to antiangiogenic therapy.

c-Met/β1 Integrin Binding Drives Ligand-Independent Cross-Activation

Having shown that c-Met/β1 integrin complex formation drives these two distinct invasive oncologic processes, we next sought to determine if c-Met-β1 integrin binding occurs exclusively between their extra- or intracellular domains. To do so in a manner free of the confounding influence of cells, we performed far-Western blotting, a technique derived from Western blotting to detect protein–protein interaction in vitro (16).

Unlike Western blots, in which an antibody binds its target on a membrane, far-Western blotting utilizes either a tagged, or antibody-detectable protein (bait) to bind and detect a target protein (prey) that is denatured and renatured to conform to its 3D structure on the membrane (16). Thus, whereas Western blotting detects proteins, far-Western blotting detects protein:protein interactions. By far-Western blotting, binding of c-Met and β1 integrin occurred exclusively in their extracellular domains **(Figures 5A and B)**, and β1 integrin in lysates from U87-Bev^{R} xenografts exhibited more robust binding to the c-Met extracellular, not intracellular, domain, compared with U87-Bev^{S} lysates **(Appendix A, Figure S24)**. To determine if this binding of c-Met to β1 integrin first occurred before or after protein translocation to the cell membrane, we biotinylated U87 cellular proteins, allowing specific labeling of the extracellular portions of all cell

membrane proteins, followed by column purification and elution of biotinylated proteins. IP revealed that the c-Met/β1 complex was not detected in the nonbiotinylated proteins, suggesting that complex formation occurred after protein translocation to the cell membrane **(Figure 5C)**.

We then investigated whether this extracellular binding of c-Met and β1 integrin allowed ligand-independent cross-activation. Increasing HGF concentrations increased c-Met/β1 integrin complex formation and increased β1 activation in U87 cells, indicating ligand-induced complex formation and ligand-independent cross-activation of one complex member by the other **(Figure 5D)**. Corresponding to this ability of HGF to activate β1, increasing concentrations of HGF increased adhesion of U87 cells to fibronectin (FN) ($P = 0.02$; **Appendix A, Figure S25**), without altering β1 levels **(Appendix A, Figure S26)**, suggesting increased β1 functional activity. We confirmed that the converse ligand-independent cross-activating relationship also existed by showing that β1 activation by its ligand fibronectin dramatically increased ligand-independent phosphorylation of c-Met in U87 cells **(Figure 5E)**. We then investigated the role of ILK, a mechanosensor which binds integrins for structural support (17), in this cross-activation of c-Met by activated β1. We confirmed by far-Western blotting that ILK binds the c-Met cytoplasmic domain **(Appendix A, Figure S27)**, and showed that

shRNA depletion of ILK **(Figure 5F)** or treatment with Cpd 22, an ILK inhibitor **(Figure 5G)**, blocked ligandindependent phosphorylation of c-Met in the presence of fibronectin in U87 cells.

We then investigated whether the necessity of ILK for ligand-independent phosphorylation of c-Met in the presence of fibronectin reflected true intrinsic kinase activity of ILK, a subject of debate in the literature (17), or if it reflected other functions of ILK, such as our finding that Cpd22 changed the morphology of U87 cells to more circular and reduced adhesion to fibronectin **(Appendix A, Figure S28)**, consistent with the capacity described by others of ILK to act as a mechanosensor (17). We found that coincubating recombinant ILK with recombinant intracellular c-Met led to c-Met phosphorylation **(Figure 5H)**, a likely mechanism of the fibronectin-induced c-Met phosphorylation we observed. Further evidence supporting kinase activity of ILK and a mechanism by which this kinase could influence the c-Met signaling cascade was identified when we demonstrated that ILK phosphorylates AKT, a shared downstream mediator of c-Met and β1 integrin **(Appendix A, Figure S29)**. Collectively, data in **Figure 5** indicates reciprocal ligand-independent cross-activation between c-Met and β1 integrin, demonstrating the power of their complex.

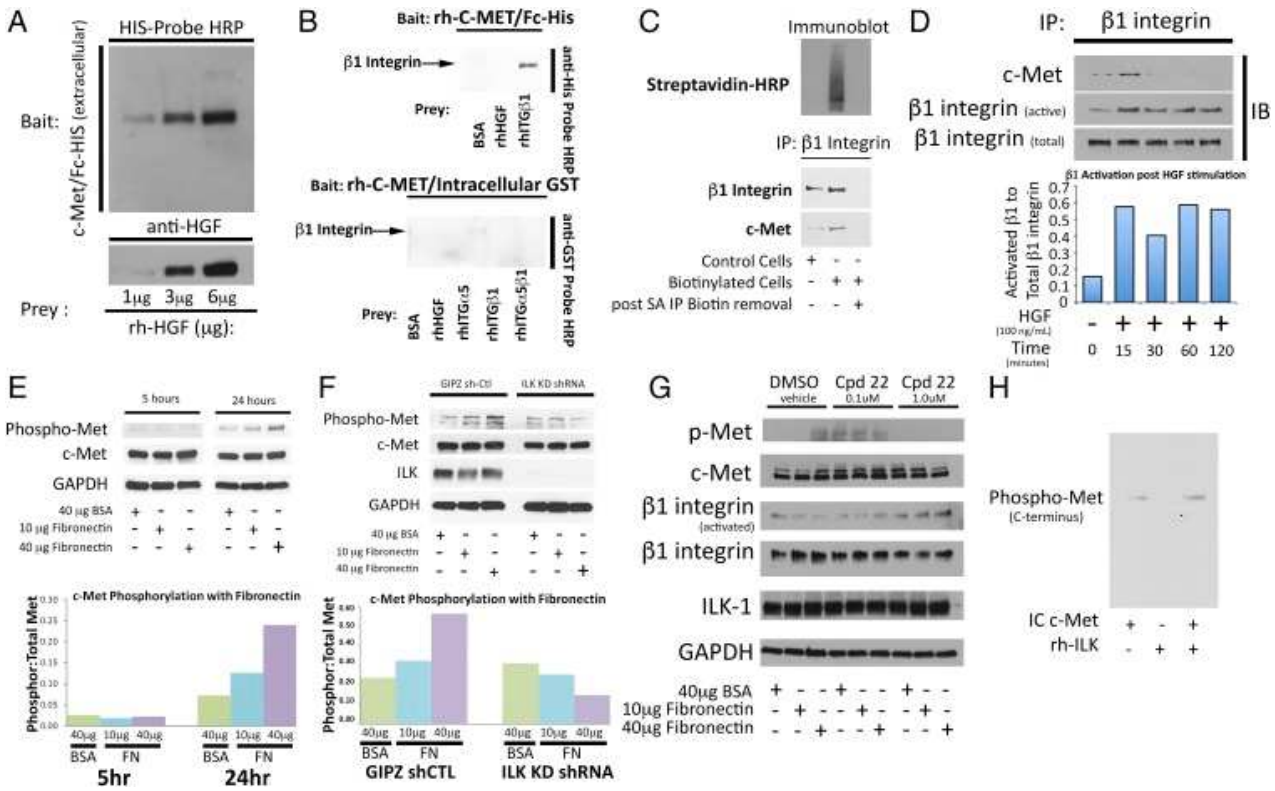

Figure 5. Localizing c-Met/β1 binding and identifying its consequences (*A*) Far-Western blot of control bait (recombinant human extracellular His-tagged c-Met = rh-cMet) and prey (recombinant human HGF) with known interaction: HGF bound rh-cMET in a dose-dependent manner. **(*B*)** Far-Western blot of extracellular (EC) vs. intracellular (IC) c-Met to assess β1 binding. (*Upper*) His-tagged EC rh-cMet was the bait and preys were BSA (negative control), HGF (positive control), or recombinant β1. Band density reflects binding to EC rh-cMet, with binding of β1 to EC c-Met found. (*Lower*) Using BSA (negative control), HGF, recombinant α5, β1, and α5β1 as prey with GST-tagged IC rh-cMet as bait, lack of binding of IC c-Met to β1 was found. **(*C*)** To determine if c-Met/β1 binding occurred intracellularly, extracellular U87 proteins were selectively biotinylated, after which cell lysates were incubated with avidin-conjugated beads and eluted. (*Upper*) Nonbiotinylated proteins in the eluant and biotinylated proteins bound to beads were blotted with HRP-conjugated streptavidin, revealing signal only in proteins bound to beads, confirming biotinylation effectiveness. (*Lower*) Nonbiotinylated proteins in the eluant and nonbiotinylated whole cell lysates underwent β1 IP followed by blotting of the precipitant for β1 and c-Met, revealing c-Met/β1 complex only in whole cell lysates.

Proteins bound to beads could not undergo IP as the acidic eluting solution disrupted protein–protein bonds. **(*D*)** U87 cells treated with HGF exhibited increased β1 activation and increased c-Met/β1 integrin complex formation. **(*E*)** U87 cells were plated on BSA or increasing FN concentrations for 5 and 24 h. Cells were blotted for total and phosphorylated c-Met. Bar graph represents ratio of phosphorylated c-Met to total c-Met for each condition. **(*F*)** U87 cells transduced with ILK shRNA or vector control were stimulated with FN. While cells with vector control maintained increased c-Met phosphorylation in response to increasing FN concentrations, cells with ILK shRNA lost this response. **(*G*)** U87 cells were treated with ILK inhibitor Cpd 22, which eliminated the ability of FN to drive c-Met phosphorylation. **(*H*)** Recombinant ILK was incubated with IC c-Met and adenosine 5′-O-(3-thiotriphosphate) (ATPγS), with c-Met phosphorylation detected by Western blot. While c-Met autophorphorylation occurred without ILK, c-Met phosphorylation was increased with ILK.

c-Met/β1 Complex Excludes α5 Integrin and Has Greater Fibronectin Affinity than α5β1 Integrin.

We then determined the relative affinities of β1 integrin for c-Met versus its predominant natural heterodimer partners α5 or αV integrin. In U87 GBM cells, c-Met could bind αV but not α5 integrin **(Figure 6A)**, similar to what we observed in breast cancer cells **(Figure 1A)**. We next devised a unique technique to isolate the c-Met/β1 complex to assess proteins specifically bound within the complex and to eliminate carried over protein bound to each protein when utilizing traditional IP techniques, a protocol we termed "sequential immunoprecipitation." In this protocol, we immunoprecipitated agarose beads bound to β1 integrin antibody followed by IP of c-Met integrin antibody bound to magnetic beads as demonstrated in the schematic of **Figure 6B**. This technique revealed almost no α5 or αV integrin in the β1+ c-Met+ double immunoprecipitate **(Figure 6C)**, suggesting displacement of α5 and αV integrin by c-Met during c-Met/β1 integrin complex formation. Importantly, nearly all fibronectin, VCAM, and osteopontin, ECM proteins known to bind α5β1 and αvβ1, were bound to the β1+ c-Met+ double IP, containing the c-Met/β1 complex, rather than the β1+ c-Met− portion of the β1 integrin immunoprecipitate that failed to be pulled down in the second c-Met IP and therefore contained α5β1 and αvβ1 **(Figure 6C)**. This finding suggests that the c-

Met/β1 complex binds fibronectin, the primary substrate along which cancer invasion occurs, along with VCAM and osteopontin, with greater affinity than α5β1 or αvβ1, the natural receptors for these ECM proteins. Consistent with these data, using dot blotting, we found that coincubated c-Met and β1 integrin bound recombinant fibronectin more efficiently than coincubated α5 and β1 integrin or coincubated α4 and β1 integrin **(Figure 6D)**.

To define c-Met/β1 integrin binding sites, we performed PyMOL modeling of c-Met/β1 integrin binding based on the crystal structures of each protein (18, 19). Both c-Met and α5 integrin contain sevenbladed β-propeller domains, with sequence identity of 15% between them (Cα rmsd 2.9 Å). α5 integrin interacts with β1 integrin through these β-propeller domains. Therefore, we modeled c-Met/β1 interaction based on the α5/β1 structure (Protein Data Bank 4wk4) using structural alignment. This analysis suggested that c-Met and α5 integrin share a common binding site on β1 integrin **(Appendix A, Figure S30 A and B)**. The resulting complex was consistent with membrane orientation, as the C-terminal ends of c-Met and β1 integrin point in the same direction. These findings reveal that β1 integrin forms a complex with α5 or c-Met but never both at the same time, as both bind the same region of β1 integrin. This is further demonstrated by the superimposition of α5 integrin and c-Met in **Appendix A, Figure**

S30C to demonstrate the similarity between the binding regions of these two proteins, allowing for β1 integrin's exclusivity for a single partner in exchange for the other. Fibronectin, the primary ligand for α5/β1, binds α5/β1 through an Arg-Gly-Asp motif (20). Most of the contact with fibronectin is through β1 integrin, although there is limited contribution from α5. When c-Met replaces α5, PyMOL modeling predicts better contact with fibronectin **(Appendix A, Figure S31)**. An explanation for this improved contact derived from our modeling, which revealed that the closed conformation of β1, known to have low affinity for fibronectin, has steric clash with the first IPT domain of c-Met **(Figure 6E)**. To resolve this clash, PyMOL modeling suggests a mechanism whereby c-Met overcomes this clash by keeping β1 in its high-affinity open conformation, providing a structural foundation for our sequential IP results and a functional explanation for why cancer cells benefit by replacing α5 with c-Met as a β1 binding partner.

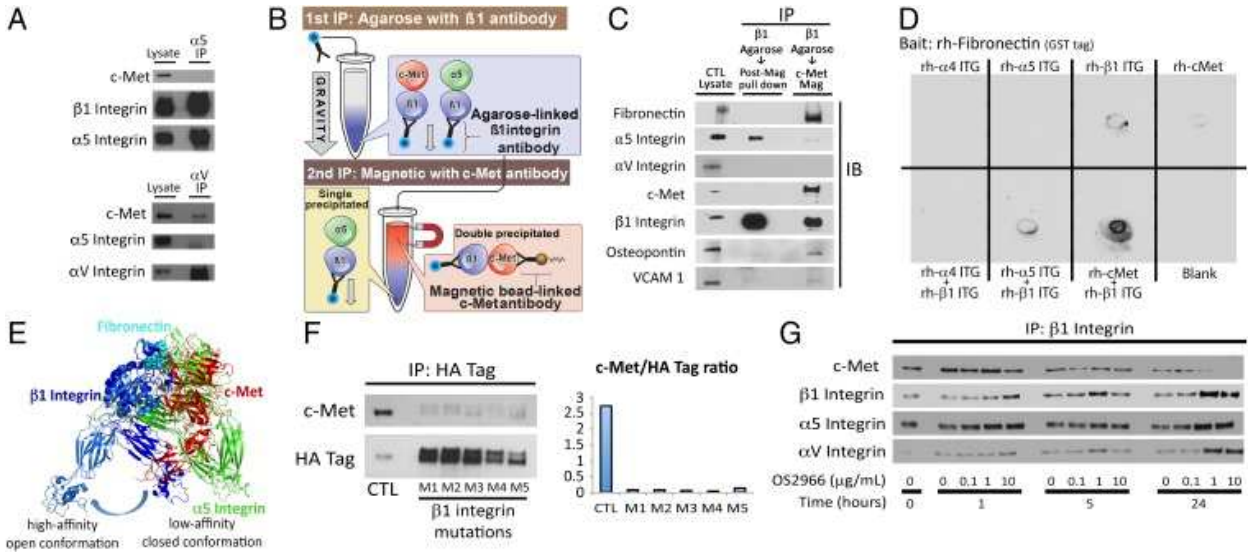

Figure 6. c-Met/β1 integrin complex affinities and modeling (A) IP revealed that αV but not α5 integrin bound c-Met in U87. **(B)** Sequential IP schematic: isolating the c-Met/β1 complex by binding β1 via agarose beads, followed by magnetics beads binding c-Met in complex with β1. **(C)** Sequential IP of β1 followed by c-Met revealed that a c-Met/β1 double IP contained far more fibronectin (FN), VCAM, and osteopontin and far less α5 than a β1 integrin single IP, with αV in neither, suggesting that c-Met displaces α5 from its β1 binding site and that c-Met/β1 integrin binds FN better than α5/β1 integrin. **(D)** Dot blotting revealed that co-incubated c-Met+β1 bound FN far better than c-Met, α4, α5, or β1 alone; α5+β1; or α4+β1. **(E)** PyMOL analysis defined steric constraints causing c-Met to preferentially bind β1 in its high-affinity open conformation. **(F)** Five amino acids in β1 integrin predicted by ALA scanning as crucial to c-Met/β1 binding were changed to alanine by mutagenesis of a β1–HA fusion protein. HA IP of HEK cells expressing these constructs revealed decreased c-Met binding to each of five mutants versus wild-type β1–HA fusion protein. **(G)** Treating cultured U87 cells with variable concentrations of β1 neutralizing antibody OS2966 for 1, 5, and 24 h decreased c-Met/β1 complex formation as assessed by β1 IP.

CHAPTER 5

DISRUPTING THE COMPLEX

Genetic or Pharmacologic Targeting of c-Met/β1 Integrin Binding

Based on this PyMOL data, we investigated genetic and pharmacologic approaches to disrupt c-Met/β1 interaction. The ability of the smaller β1 molecule to bind c-Met proved readily targetable by site-directed mutagenesis of five individual amino acids identified as crucial for binding from our PyMOL modeling using the Rosetta ALA scanning method (21) **(Figure 6F and Appendix A, Figures S32 and S33 and Table S1)** and OS2966, a therapeutic humanized β1 integrin neutralizing antibody **(Figure 6G)**. When targeting the ability of c-Met to bind β1 via sitedirected mutagenesis of four regions of amino acids in the loops on the top of the c-Met propeller structure, regions suggested by PyMOL modeling to be important for c-Met/β1 binding, some reduction in complex formation occurred with three of the four analyzed mutations **(Appendix A, Figures S34 and S35 and Table S1)**, but less robustly than seen with single amino acid changes in β1 integrin.

When targeting c-Met pharmacologically via therapeutic artificial ligand NK4, co-administering NK4 and HGF reduced c-Met phosphorylation and c-Met/β1 complex formation **(Appendix A, Figures S36 and S37)**. When targeting c-Met via onartuzamab, a neutralizing therapeutic antibody blocking four amino acids in the extracellular β-propeller Sema domain of c-Met **(Appendix A, Table S1)**, this antibody

reduced the ability of some β1 antibodies to detect their epitopes, which may have been obscured by onartuzamab **(Appendix A, Figure S38 and Table S1)**.

CHAPTER 6

ROLE OF c-Met/β1 COMPLEX IN CANCER VERIFIED IN PATIENT SPECIMENS

c-Met/β1 Complex Formation Increases in Metastatic Breast Cancer Patients

We then determined if formation of the c-Met/β1 complex is relevant to breast cancer metastases in patient samples. Using PLA, we found increased c-Met/β1 complex formation in patient breast cancer metastases to the brain compared with paired primary breast tumors from the same patients (P = 0.0006, 0.004) **(Figure 7A)**. This finding was in contrast to the fact that neither c-Met (P = 0.3) nor β1 integrin (P = 0.4) expression individually increased in archived microarray analysis (22) of paired primary breast tumors and metastases from eight patients **(Appendix A, Figure S39)**. These findings indicate that increased formation of the complex is a more specific mechanistic biomarker of breast metastases than upregulation or activation of each individual factor.

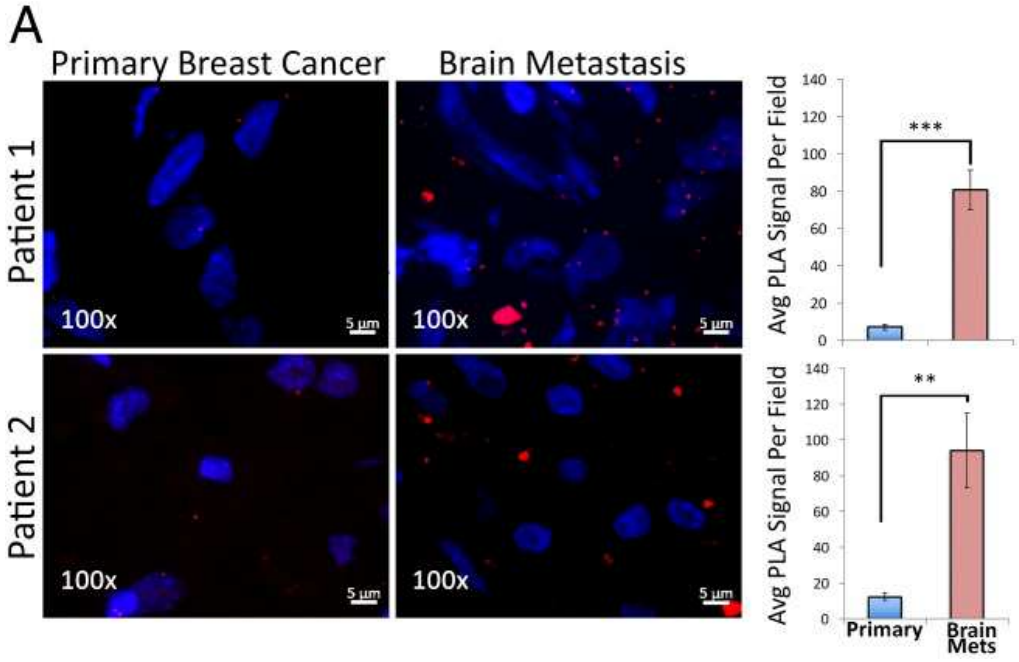

Figure 7A. In breast cancer patients, the c-Met/β1 integrin complex is associated with metastases (A) Increased c-Met/β1 complex levels by PLA noted in brain metastases versus primary breast tumors from the same patients (P = 0.0006 patient 1; P = 0.004 patient 2; n = 5 fields per tumor).

c-Met/β1 Complex Formation Increases in Bevacizumab-Resistant GBMs

We then analyzed c-Met/β1 integrin complex formation in nine bevacizumab-resistant GBMs (5-7). PLAs detected 20-fold more c-Met/β1 complexes in bevacizumab-resistant GBMs compared with prebevacizumab ($P < 0.05$; Figure 7B), greater than the 2-fold increase in recurrent GBMs not treated with bevacizumab **(Figure 7B)**. As with metastases, the increased c-Met/β1 complex formation in bevacizumab-resistant GBMs was far more than the 2- to 3-fold individual increase in phosphorylated c-Met or β1 integrin we previously reported in these tumors (5-7). These findings indicate that, similar to breast metastasis, increased formation of the complex is a more specific mechanistic biomarker of bevacizumab resistance, than upregulation or activation of each individual factor.

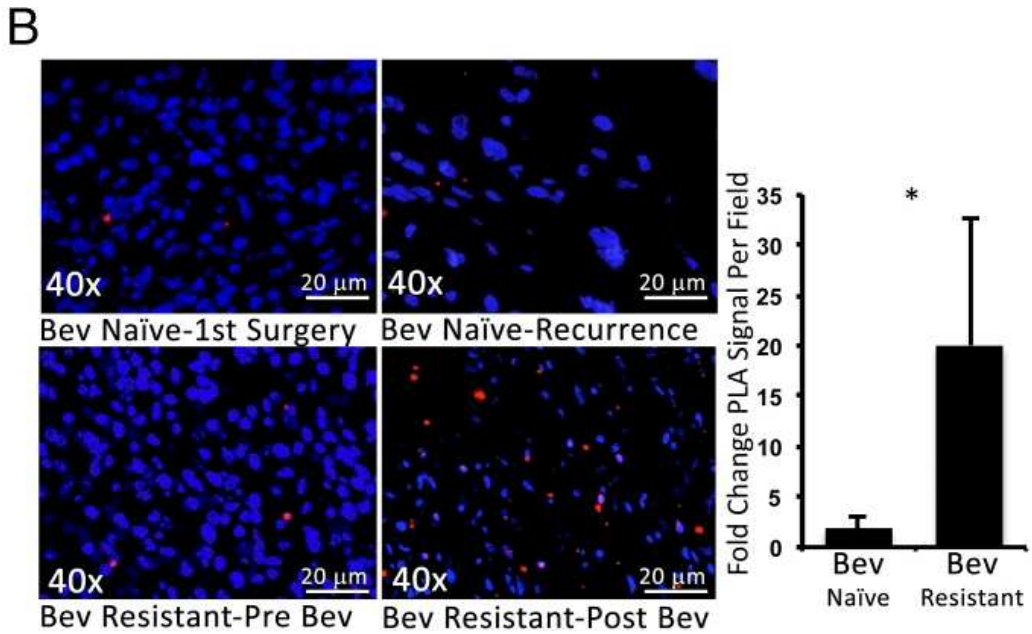

Figure 7B. In GBM patients, the c-Met/β1 integrin complex is associated with bevacizumab-resistance. (B) c-Met/β1 integrin complex levels in nine GBM patients developing bevacizumab resistance and nine control GBM patients naïve to bevacizumab at diagnoses and recurrence were assessed with PLA. Representative PLA images from "Bev-naïve" and "Bev-resistant" patients with fold-change in PLA complex numbers after versus before tumor recurrences graphed ($P < 0.05$ Bev-resistant versus Bev-naïve). *$P < 0.05$; **$P < 0.01$; ***$P < 0.001$.

To define the regional variability in c-Met/β1 complex formation in patients, we obtained site-directed biopsies from a bevacizumab-resistant GBM **(Figure 8A)**. This technique allows the successful sampling of various regions of tumor, capturing the spectrum of hypoxia and nutrient deprivation occurring in GBM after evolving anti-angiogenic therapy resistance. The c-Met/β1 integrin complex was detected in five regional biopsies from bevacizumab-resistant GBM. Increased complex formation occurred in invasive cells beyond the enhancing tumor edge **(Figure 8A and Appendix A, Figure S40)**, with the complex also harboring phosphorylated c-Met **(Figure 8A and Appendix A, Figure S41)**. Complex formation and bevacizumab resistance proved durable, as both were maintained in PDXs derived from this bevacizumab-resistant GBM, with the complex increasing further when the PDXs were treated with bevacizumab, to which they showed resistance **(Figure 8 B** and **C** and **Appendix A, Figure S42)**. We did not observe complex formation in a patient GBM treated with low-dose bevacizumab (5 rather than 10 mg/kg) **(Appendix A, Figure S43)**, confirming the

dose-dependent increase in c-Met/β1 integrin associated with bevacizumab treatment of cultured cells **(Figure 3D)** and xenografts **(Appendix A, Figure S14)**. The presence of small quantities of c-Met/β1 integrin complex in bevacizumab-naïve GBMs seen via PLA before the robust increase occurring with bevacizumab resistance led us to analyze c-Met/β1 integrin complex levels in GBMs at diagnosis to determine its impact on patient survival. The percent of β1 integrin bound to c-Met via IP ranged from 0 to 17% in lysates from GBMs taken at diagnosis. This percent correlated inversely with survival ($P < 0.05$; **Appendix A, Figures S44 and S45**). Thus, the c-Met/β1 integrin complex associated with bevacizumab resistance portended the poor prognosis that these patients experience (22).

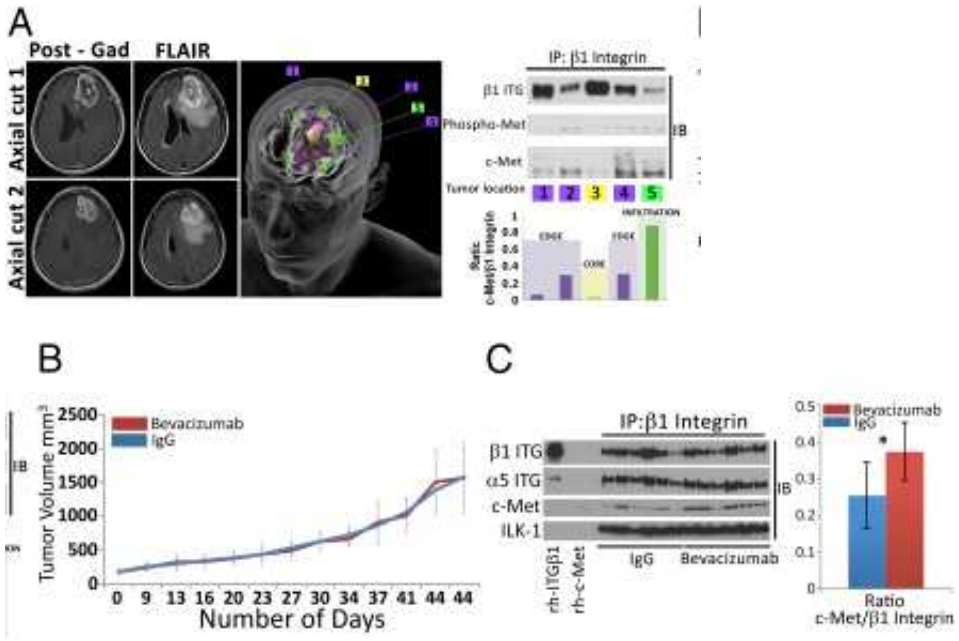

Figure 8. Regional variation and durability of c-Met/β1 complex in bevacizumab-resistant GBM. (**A**, Left) Locations on axial MRIs of five site-directed biopsies from a bevacizumab-resistant GBM. First column is T1 post-gadolinium, and second is FLAIR imaging. Top row is axial cut 1, with biopsies 3 (tumor core), 4 (edge), and 5 (infiltration) shown. Bottom row is axial cut 2 with biopsies 1 and 2 (both edge) shown. (**A**, Middle) Artist's 3D rendition of locations of the five site-directed biopsies taken from the bevacizumab-resistant GBM. (**A**, Right) Lysates from each location were used for IP with β1 integrin and immunoblotted for c-Met and phospho-Met. Quantified c-Met/β1 complex levels from each location graphed in the Lower Right categorized as tumor core, tumor edge, or infiltration. **(B)** The tumor from the patient in A was passaged into 10 SCID mice and treated with IgG (n = 5) or bevacizumab (n = 5). Tumor volume (in cubic millimeters) is plotted versus time. PDXs remained bevacizumab resistant and **(C)** c-Met/β1 integrin complex formation increased following treatment as shown by the β1 integrin IP of PDXs with blotting for c-Met. *P < 0.05.

CHAPTER 7

DISCUSSION

CONCLUSION

We describe a complex between c-Met and β1 integrin that forms during cancer metastases and the evolution of invasive resistance to antiangiogenic therapy. These two invasive processes are examples of aggressive cancer biology contributing to severely worsened patient prognosis (7, 22) whose mechanisms have yet to be fully defined The power of the c-Met/β1 integrin complex we identified in driving these invasive oncologic processes lies in its robust affinity for fibronectin, a crucial component of the extracellular matrix that guides tumor cell invasion (23), and its ability to integrate and promote ligand-independent cross-activation of two receptors mediating chemotaxis and haptotaxis **(Figure 9)**. While c-Met and β1 integrin are each known to individually contribute to metastases (24, 25) and invasive bevacizumab resistance in GBM (5, 6, 26), the mechanisms through which these drive metastases or invasive resistance remain uncertain, as their high baseline expression levels do not change tremendously during acquisition of metastases (24, 25) or invasive resistance (5-7). The increase in c-Met/β1 integrin complex formation that we observed in metastases and bevacizumab-resistant GBM was more dramatic than the increase in the levels of c-Met and β1 integrin individually, suggesting that the complex drives these invasive processes more than the biology of the individual factors.

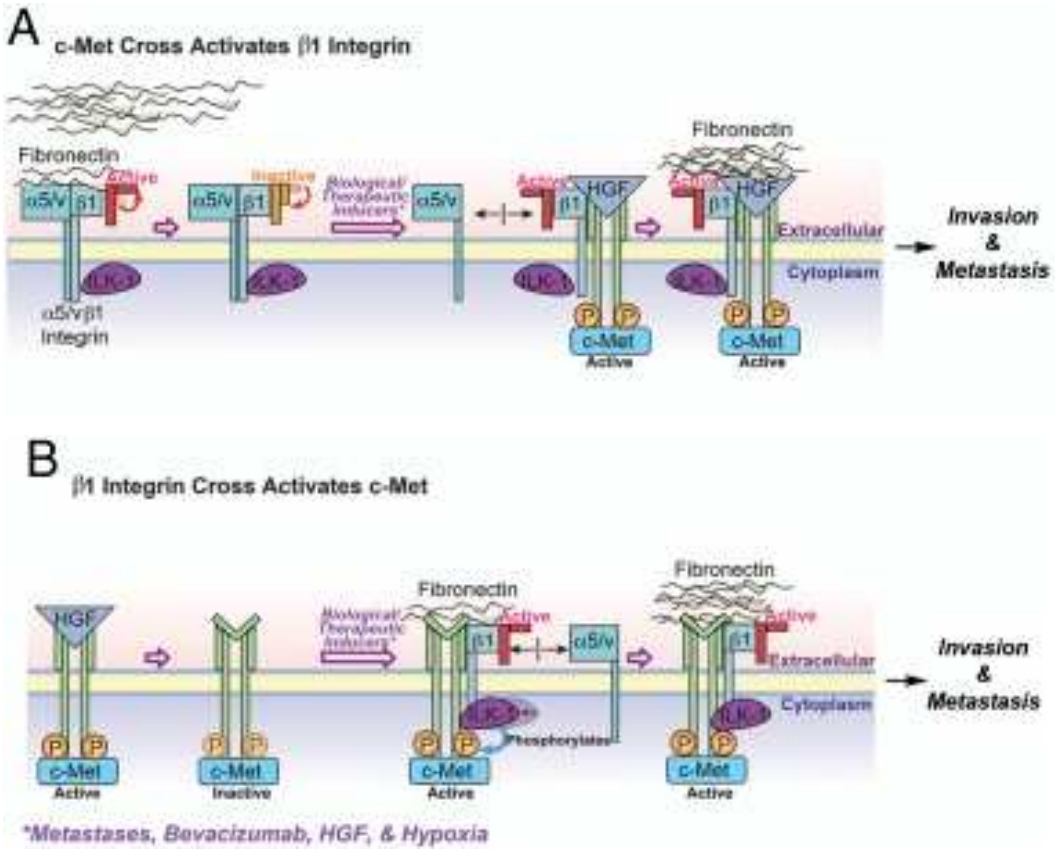

Figure 9. Stimuli driving c-Met/β1 complex formation promote ligand-independent cross-activation of each receptor and enhance cancer cell invasion. **(A)** Biologic and therapeutic stimuli (metastases, bevacizumab resistance, HGF, and hypoxia) promote c-Met/β1 integrin complex formation, which maintains β1 integrin in its activate state even without fibronectin (FN), with the c-Met/β1 complex exhibiting greater FN affinity than β1 bound to its conventional heterodimer partners αV or α5. **(B)** Stimuli described in A promote c-Met/β1 complex formation, with the c-Met/β1 complex exhibiting greater affinity for FN than β1 bound to its α-heterodimer partners and FN promoting ILK-mediated c-Met phosphorylation even in the absence of HGF.

Integrin-Receptor Tyrosine Kinase Interactions

Integrin-mediated adhesion and motility may be modulated by growth factors (27), while growth factor signaling can be modulated indirectly by integrins (28). Previous studies have demonstrated colocalization of c-Met and β1 integrin by immunostaining (1) and interaction of c-Met and α5 or β1 integrin by immunoprecipitation (1, 2). Our work demonstrates a true interaction between c-Met and β1 integrin with the utilization of far-Western blotting of recombinant proteins free of other cellular components, overcoming the limitation of colocalization studies, which provide indirect evidence, or immunoprecipitation, which sometimes artificially detects binding that can occur with micelles in immunoprecipitation of cell lysates. Furthermore, our work also expands the implications of c-Met binding β1 integrin beyond those described for other integrin–RTK interactions by demonstrating that the RTK c-Met displaces the α-heterodimer partner of β1 integrin to form a complex with β1 integrin, and that the resulting c-Met/β1 integrin complex is significantly more efficient at binding β1 integrin's natural ligand fibronectin, a major substrate along which cancer invasion occurs. This switching of the β1 integrin binding partner from α5 integrin to RTK c-Met to increase fibronectin affinity is an efficient means of increasing tumor cell migration, which depends more on turnover of integrins in focal adhesions and affinity for extracellular matrix than cell surface

expression of integrins (29). We also added molecular insight by defining residues critical for c-Met/β1 integrin binding in the loops on top of the c-Met propeller structure and the βI domain of β1 integrin. Finally, in showing the formation of this complex during metastases and therapeutic resistance, its regulation by factors in the microenvironment associated with metastases and resistance, and the ability of the complex to drive invasion and survival during hypoxia, we lend therapeutic implications to RTK–integrin interactions.

Role of VEGF in Complex Formation

We integrated our finding that VEGF165 inhibits c-Met/β1 complex formation with the previous finding that binding of VEGF to VEGFR2 leads to formation of a VEGFR2/c-Met complex in which VEGFR2 inhibits c-Met phosphorylation (26). We found that VEGF bound to VEGFR2 independently sequesters c-Met and β1 integrin, with c-Met and β1 integrin free to form their complex in the absence of VEGF, as occurs during prolonged bevacizumab treatment. The resulting c-Met/β1 complex drives invasive resistance through the ligand independent cross-activation and more efficient fibronectin binding we demonstrated. Thus, c-Met may have context-dependent binding partners whose effects need to be balanced when administering bevacizumab. Further work will be needed to determine whether the effects of VEGF on the complex also drive the role of the complex in metastases, which would be consistent with previous work suggesting that VEGF suppresses cancer metastases (8, 30).

c-Met/β1 Complex Formation Drives Ligand-Independent Activation of both Receptors

Constitutive ligand-independent activation of RTKs such as c-Met (31) and EGFR (32) has been described in cancers through genetic alterations. Here, we identified an alternative mode of ligand-independent c-Met activation, as c-Met/β1 integrin complex formation allowed fibronectin binding to β1 integrin to drive c-Met phosphorylation. Indeed, PyMOL analysis revealed c-Met to sterically keep β1 integrin in its high-affinity open conformation, allowing the converse effect of c-Met driving ligand-independent β1 activation to occur as well. Further work will be needed to determine if the converse holds true, namely if the active β1 conformation keeps c-Met in a conformation that promotes auto-phosphorylation.

ILK: Functionally Linking β1 Integrin and c-Met

Given that integrins lack enzymatic activity, their signaling depends on recruiting adaptor proteins (33). One of the best described of these proteins is ILK, which binds some β integrin cytoplasmic domains. ILK contributes to actin rearrangement, cell polarization, migration, proliferation, and survival (34). Some have suggested that the kinase-like domain of ILK lacks catalytic activity (35), while others have identified kinase activity and reported that, while the atypical protein kinase domain of ILK lacks some amino acids considered essential for phosphotransferase activity, similar deficiencies are present in the catalytic domains of other known kinases (36). Our investigation supported kinase activity of ILK that phosphorylated c-Met, allowing the ligand-independent activation we found to occur in the complex, and AKT, a downstream mediator of c-Met. These findings link β1 signaling via ILK to c-Met and its associated downstream pathways.

Therapeutic Implications

There are numerous therapeutic implications of our validation of the c-Met/β1 complex as a mechanism of metastases and invasive resistance. ILK inhibitors have been investigated as anticancer therapies (37) and our demonstration of their ability to decouple the receptor cross-talk in the c-Met/β1 complex may be an added advantage of this approach. Furthermore, in the case of resistance to antiangiogenic therapy, the tendency for the c-Met/β1 complex to form at higher doses of these therapies suggests a role for investigating the impact of anti-angiogenic therapy's dosage on efficacy and resistance evolution. Such studies could determine that the notion that the maximum tolerable dose is most effective, while applicable to conventional chemotherapy targeting tumor cells, may not be applicable for antiangiogenic therapy targeting the tumor microenvironment. Instead, for antiangiogenic treatments, we may find that "less is more" (38). The power of the c-Met/β1 complex could also be harnessed therapeutically by screening for small-molecule inhibitors that disrupt the extracellular binding of the residues we identified in the loops on top of the c-Met propeller and the βI domain of β1 integrin. Since complex up-regulation occurs more robustly in metastases and resistant tumors than increased activation of either individual factor, such an approach may prove more effective at targeting metastases or invasive resistance than

c-Met or β1 integrin inhibition alone, which have produced concerns about toxicity or failed to produce meaningful results when used alone or in the setting of antiangiogenic therapy resistance (39, 40).

MATERIALS AND METHODS

Study Approval.

Human tissue research was approved by the University of California San Francisco (UCSF) institutional review board (approval 11- 06160). Animal experiments were approved by the UCSF institutional animal care and use committee (approval AN105170-02).

Cell Culture.

U87-MG (HTB-14, ATCC) and U251 (09063001, Sigma) human GBM cells and MDA-MB-231, HCC1143, and HCC3153 human breast cancer cells were passaged for fewer than 6 mo, verified by short tandem repeat (STR) profiling, and confirmed to be Mycoplasma-free. MDA-MB-231-BR brain-seeking cells were generated as described (11) and provided by S. K. Srivastava, Texas Tech University, Lubbock, TX. Cells were cultured in DMEM/F-12 supplemented with 10% FBS and 1% P/S and maintained at 37 °C. Hypoxia studies used an incubator that reduced oxygen from 20% (normoxia) to 1% (hypoxia).

Western Blot.

Human tissue samples and cell preparations were harvested in 1× radio immunoprecipitation buffer (10× RIPA; 9806, Cell Signaling) and one tablet each of PhoStop and Complete Mini (04906845001 and 04693124001, Roche). Insoluble materials were removed by centrifugation at 300 × g for 20 min at 4 °C. Protein concentration was determined using the bicinchronic acid (BCA) assay (23225, Thermo Scientific). Samples were prepared with 10–30 µg of protein in RIPA buffer with 4× LDS loading buffer (LP0001, Life Technologies). Samples were electrophoresed on SDS/PAGE gels, transferred to PVDF membranes, and probed with primary antibodies (Appendix A, Table S2) overnight at 4 °C. Membranes were detected using HRP-conjugated secondary antibodies and imaged using radiographic film.

Immunoprecipitation.

Samples were prepared in 500 µL RIPA buffer containing 150–500 µg of protein. For β1 IP, 50 µL of protein A magnetic bead slurry (8740, Cell Signaling) were aliquoted per sample and washed with 500 µL of cell lysis buffer (9803, Cell Signaling). Beads were incubated with mouse monoclonal anti-β1 antibody (1:50; ab7168, Abcam) in 200 µL of 0.1% Triton-X 100 PBS for 15 min at room temperature (RT). Beads were

magnetically precipitated and resuspended with sample lysate for incubation on a rotator (4 °C overnight). Antibody-bound beads were magnetically separated from the lysate supernatant and washed three times in 500 µL cell lysis buffer. Samples were eluted by precipitating beads on a magnetic rack and resuspending in 40 µL of 3× blue sample buffer 30× reducing agent: 1.25 M DTT (1:30; 7722s, Cell Signaling). Resulting samples were heated at 95 °C (5 min), centrifuged at 300 × g at RT, and magnetically precipitated. The supernatant was used for SDS/ PAGE electrophoresis. Blots were probed with primary and secondary antibodies **(Appendix B, Table S2)**.

Engineering Cells with Inducible β1 Integrin and c-Met Interaction.

Plasmid information is in **Appendix B, Table S3**. Our inducible protein–protein interaction system was the Lenti-X iDimerize heterodimer system (Clontech), which uses FKBP12 and FKBP rapamycin-binding domains altered to specifically bind the A/ C heterodimerizer (AP21967) ligand. ITGB1 cDNA was amplified from pRK5 β1 vector (31786, Addgene) using Pfx50 high-fidelity Taq (Invitrogen) targeted for insertion into the 3′ multiple cloning site of the pLVX-Het1-DmrC vector. The PCR product was produced using B1-NotI-FW and B1-BamHI-HA RV primers **(Appendix B, Table S4)**, subcloned into pCR4-Blunt-TOPO, and inserted into pLVX-Het1-DmrC. Clones were

screened with restriction digest and sequencing. The cMET coding region was amplified from p-ENTR-cMET (16042, Addgene) with primers in **Appendix B, Table S4**. The PCR fragment was cloned into pCR4- Blunt-TOPO. The resulting pCR4-Blunt-TOPO-cMET(HIS) vector was digested with NotI and BglI and run on 0.75% low melting point agarose. The insert was ligated into NotI linearized pLVX-Het2. Lentiviral particles harboring constructs with an N-terminally DmrC-fused ITGB1 and N-terminally DmrA-fused Met coding sequences were generated using HEK293T cells and a third generation packaging system, with supernatants used to transduce MDA-MB-231, U87, or U251 cells for 24 h, followed by antibiotic selection.

Proximate Ligation Assay (PLA).

We utilized the Duolink Detection System (Sigma) on (i) cells with and without the iDimerize system on chamber slides and (ii) paraffin-embedded human tumor tissue and frozen tissue from intracranial U87-BevS , U87-BevR , SF7227, SF7300, or SF7796 xenografts, established as described (5, 6). Primary antibodies were mouse monoclonal anti-integrin β1 (1:50; ab52971, Abcam) and rabbit monoclonal anti–c-Met (1:250; ab51067, Abcam). Secondary antibodies were anti-mouse and anti-rabbit IgG Duolink in situ PLA probes (DUO92002/4, Sigma), respectively, per manufacturer instructions.

PLA signal was assessed using Duolink in situ detection reagents (DUO92008, Sigma) and imaged using a Zeiss AxioObserver Z1 system equipped with an AxioCam MRm CCD and AxioVision software (Release 4.8). Images were quantified by counting dimerizations (red dots) per cell for chamber slides or per 100× field for tissue from four representative selections using the ImageJ cell counter plugin.

Assessment of c-Met and β1 Interaction in Cultured Cells.

U87 or MDA-MB231 cells were cultured, in bevacizumab (Genentech), HGF (294-HGN-005/CF, R&D Systems), hypoxia, conditioned HUVEC media, or serum-free media containing VEGF165 (584501, Biolegend), VEGF165b (3045VE025CF, R&D Systems), or VEGF189 (8147VE025CF, R&D Systems) and complex formation was assessed via IP. c-Met activation through β1 signaling was assessed by plating U87 cells on increasing fibronectin amounts (sc-29011, Santa Cruz Biotechnology) and blotting for phosphorylated c-Met**.**

Migration and Proliferation Assays.

Transduced MDA-MB-231 or U87 cells were plated in six-well plates at 90% confluency. Cell monolayers were wounded using p200 pipette tips scratching the plastic surface from 12 to 6 o'clock. The wound was divided into four quadrants and

imaged at 0, 5, and 24 h. Images were collated and analyzed using TScratch software (41). In parallel, the same cells were plated into black 96-well clear-bottom plates and analyzed using CyQuant cell proliferation assay kits (c7026, Thermo Scientific).

Animal Work.

For mammary xenografts, 1 × 105 MDA-MD-231 cells were injected unilaterally into the fourth mammary fat pad in 10 μL. For tail vein injections, 106 MDA-MB-231-iDimerize-c-Met-β1 cells in 100 μL were injected via tail veins. Some tumor cells were pretreated with 500 nM AP219667 in complete DMEM 2 h before tail vein injection. For intracranial xenografts, we intracranially implanted cells from previously described (5, 6) bevacizumab-resistant or sensitive xenografts into severe combined immunodeficient (SCID) nude mice. Animals were treated intraperitonially with IgG (I4506, Sigma) or Avastin (bevacizumab, Genentech) at designated doses. Resulting tumors were harvested and lysed into RIPA buffer and prepared for IP as described above. The s.c. tumors were established by injecting 5 × 105 cells s.c. into the flanks of SCID nude mice. Tumor volume was V = (Y × X2)/2, where Y is the longest diameter and X is the diameter perpendicular to that.

Sequential Immunoprecipitation.

U87-BevR xenograft lysates were immunodepleted for β1 integrin using anti-β1 integrin agarose-bound complex under nondenaturing conditions in cell lysis buffer on a rotator overnight at 4 °C (Cell Signaling). The resulting β1 integrin complex was harvested from solution by centrifugation at 300 × g for 1 min and eluted from agarose beads with Pierce IgG elution buffer (21004, Thermo Scientific). The eluent was mixed with magnetic beads coupled to anti-cMet antibody and incubated on a rotator overnight at 4 °C. We then used magnetic precipitation to produce the sequentially precipitated fraction. The immune-complexed β1 integrin/c-Met moieties were then eluted under denaturing conditions in 187.5 mM Tris·HCl (pH 6.8 at 25 °C), 6% (wt/vol) SDS, 30% glycerol and 0.03% (wt/vol) bromophenol blue with 0.125 M DTT and resolved by standard SDS/PAGE.

Modeling c-Met and β1 Integrin Interaction

c-Met and β1 integrin extracellular crystal structures were available at resolutions of 2.80 Å (PDB 2uzx) and 1.85 Å (PDB 4wk4), respectively. β1 integrin was cocrystallized with integrin α5 (PDB 4wk4; Appendix A, Figure S30A). In this structure, α5 interacts with β1 integrin through the seven-bladed β-propeller. The extracellular domain of c-Met also contains a seven-bladed β-propeller domain. Therefore, we

rationalized that c-Met may interact with β1 integrin through a β-propeller domain interface similar to the one between α5 and β1 integrin (Appendix A, Figure S30B). The two propellers, with 15% sequence identity, were superimposed using MultiProt software (42) with rmsd of 2.9 Å for the 292 aligned Cα positions (Appendix A, Figure S30C). The docking method was template based, which, when template is available, is considered more accurate (43). Template was from the known α5β1 integrin structure due to the structural similarities of c-Met and α5 integrin. To model the complex, c-Met was structurally aligned on α5 using MultiProt software. As a result of template-based modeling, only one docking model was obtained. We further repacked the interface to optimize side-chain positions and remove steric clashes using FireDock web server. For study approval; morphology; immunofluorescence; qPCR; far-Western blotting; adhesion, kinase and survival assays; human tissue; microarray; and statistics, see **Appendix B, SI Methods**.

APPENDIX A

SUPPLEMENTAL MATERIAL

APPENDIX A

SUPPLEMENTAL FIGURES

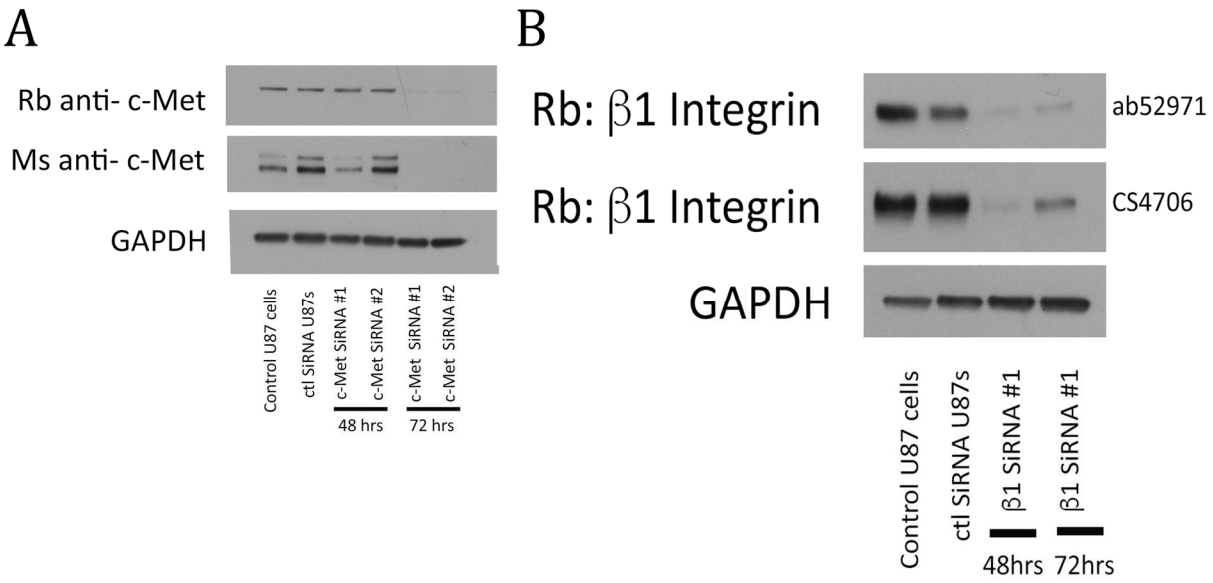

Figure S1. Validation of antibodies used with siRNA. Related to Figures 1-7. (A) Western blot of U87 cells that were untransfected (first lane), transfected with siRNA targeting control sequences (second lane), and transfected with siRNA targeting two different sequences in human c-Met and analyzed 48 (lanes three and four) and 72 (lanes five and six) hours later. Blotting was done to verify two different c-Met antibodies: rabbit ab51067 and mouse cst3148. **(B)** Western blot of U87 cells that were untransfected (first lane), transfected with siRNA targeting control sequences (second lane), and transfected with siRNA targeting humanβ1 integrin and analyzed 48 (lane three) and 72 (lane four) hours later. Blotting was done to verify two different rabbit anti-humanβ1 integrin antibodies: ab52971 and CS4706.

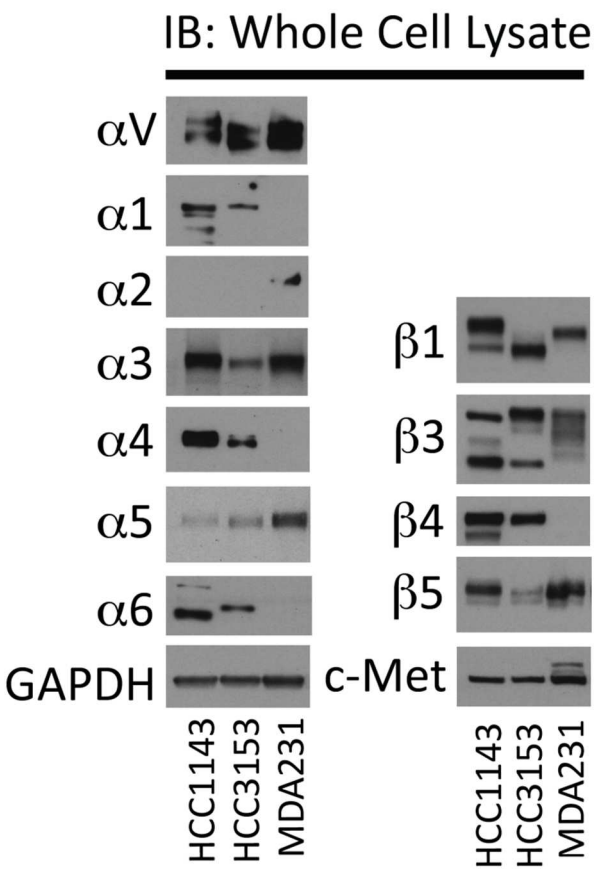

Figure S2. Western blot of integrin and c-Met expression in 3 different breast cancer cell lines. Related to **Figure 1A**. Western blotting of HCC1143, HCC3153, and MDA-MB-231 breast cancer cells was performed for 7 α integrins, 4 β integrins, and c-Met.

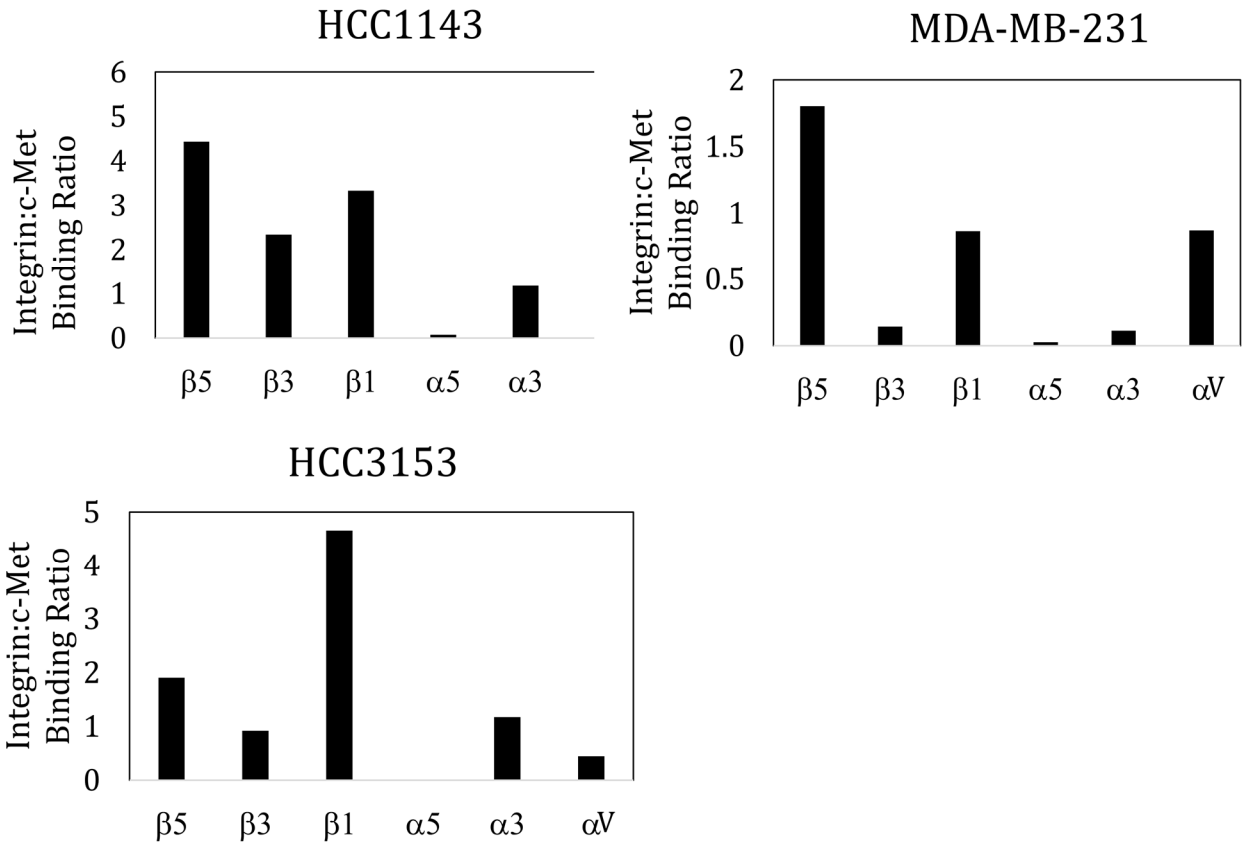

Figure S3. Western blot of integrin and c-Met expression in 3 different breast cancer cell lines. Related to **Figure 1A**. The c-Met IPs performed in Figure 1A were quantified with the ratio of densitometry of six different integrins to the c-Met densitometery calculated as integrin:c-Met binding ratios, with higher ratios suggesting more binding. Of the six integrins, four were deemed to bind c-Met significantly in HCC1143, two in HCC3153, and three in MDA-MB-231, withβ1 and β5 integrin the only two to bind strongly in all three cell lines. The former was chosen for further investigation based on greater supportive evidence for its role in cancer metastases.

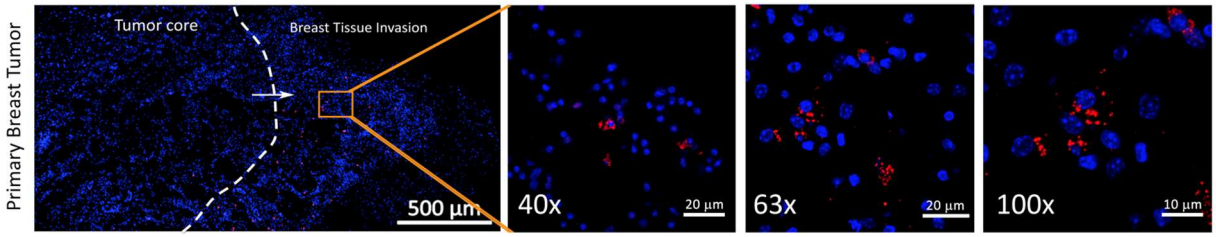

Figure S4. A second example of PLA for c-Met/β1 complex detection in a primary MDA-MB-231 mammary pad xenograft. Related to **Figure 1B**. After MDA-MB-231 breast cancer cells were implanted in the mammary pads of immunodeficient mice, PLA revealed c-Met/β1 integrin complex formation at the invasive edge of these xenografts. One representative tumor is shown in **Figure 1B** and another representative tumor is shown here.

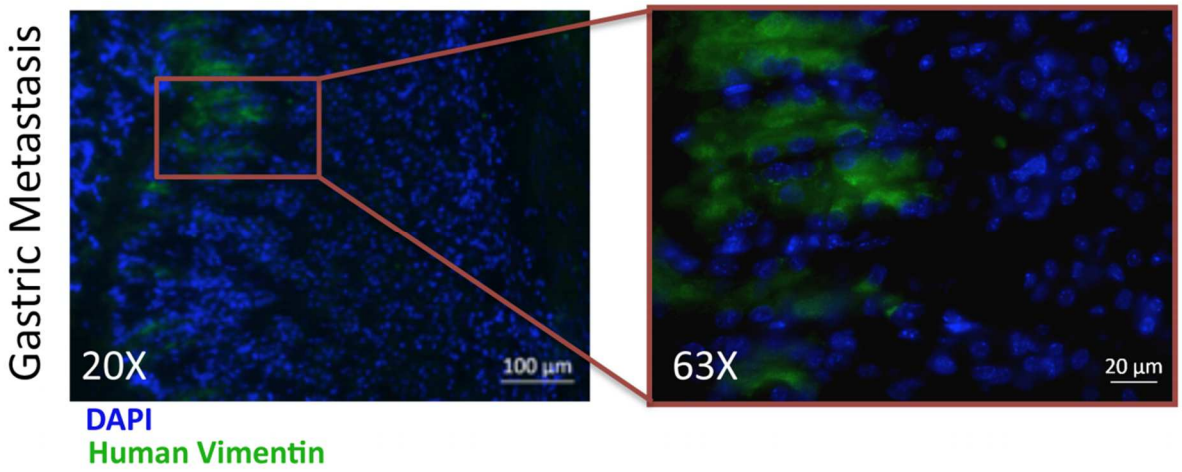

Figure S5. Vimentin staining reveals a gastric metastasis from MDA-MB-231 implanted in mammary pads of immunodeficient mice. Related to **Figure 1C**. After MDA-MB-231 breast cancer cells were implanted in the mammary pads of immunodeficient mice, one mouse developed a gastric metastasis as confirmed here by human vimentin (green) staining revealing the metastasis. PLA of this metastasis as shown in **Figure 1C** and quantified in **Figure 1D** revealed increased c-Met/β1 integrin complex formation in the metastasis relative to the primary tumor in the mammary pad.

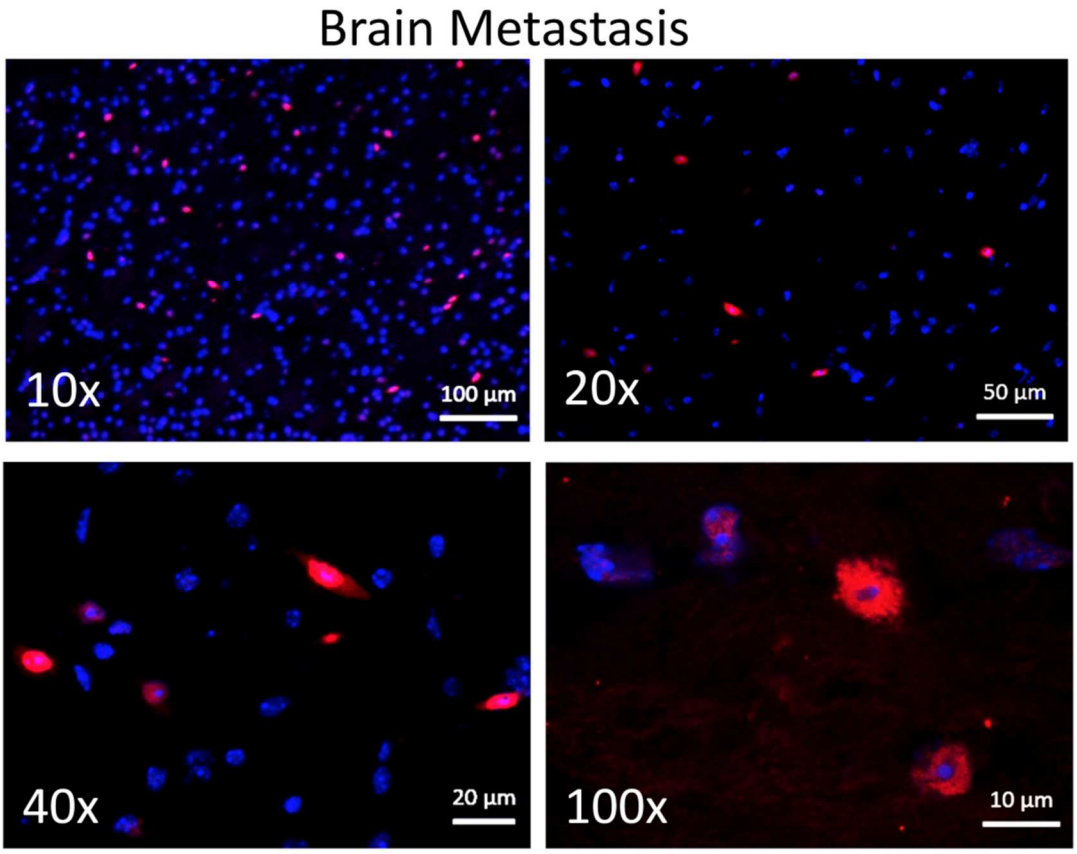

Figure S6. Additional PLA images of brain metastasis from MDA-MB-231 xenografts implanted in mammary pads. Related to **Figure 1C**. After MDA-MB-231 breast cancer cells were implanted in the mammary pads of immunodeficient mice, one mouse developed a brain metastasis. PLA of this metastasis as shown in **Figure 1C** and quantified in **Figure 1D** revealed increased c-Met/β1 integrin complex formation in the metastasis relative to the primary tumor in the mammary pad. The 10x and 40x images of the PLA of this metastasis are shown in **Figure 1C**, additional 20x and 100x images are added here.

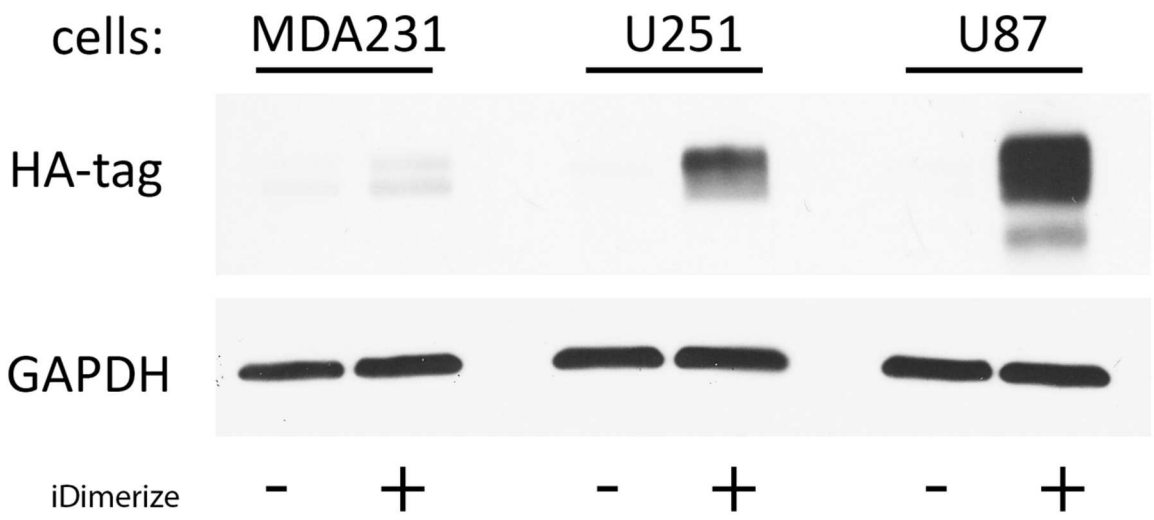

Figure S7. Engineered expression of inducible heterodimerization system. Related to **Figures 2**, **S7-S11**, and **S19-S23**. Western blot from MDA-MB-231, U251, and U87 cells engineered to express β1 integrin and c-Met fused to FRB (DmrC) and FKBP (DmrA) confirmed expression of the HA-tag fused to β1 integrin in all 3 cell lines transduced to express the inducible heterodimerizer system.

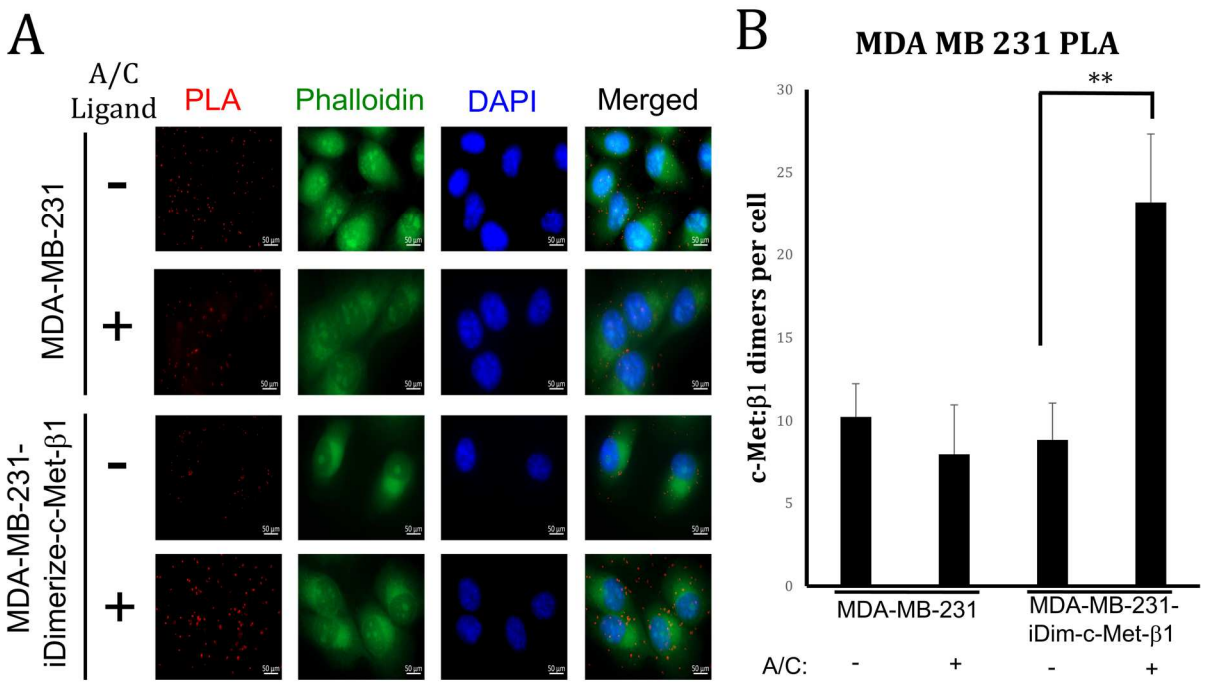

Figure S8. Use of PLA in cultured breast cancer cells to verify inducible heterodimerization system. Related to **Figure 2**. MDA-MB-231 and MDA-MB-231-iDimerize-c-Met-b1 cells were treated without or with the A/C ligand for 12 hours on chamber slides, after which PLAs were performed to assess c-Met/b1 complex formation. A/C ligand increased the presence of PLA red dots in MDA-MB-231-iDimerize-c-Met-b1 cells relative to the background seen in MDA-MB-231-iDimerize-c-Met-b1 cells without A/C ligand (*P*=0.002), with MDA-MB-231 cells with or without A/C ligand at the same background as MDA-MB-231 cells without A/C ligand (*P*=0.2). 100x magnification, scale bars 50 mm. * *P*<0.05; ** *P*<0.01 *** *P*<0.001.

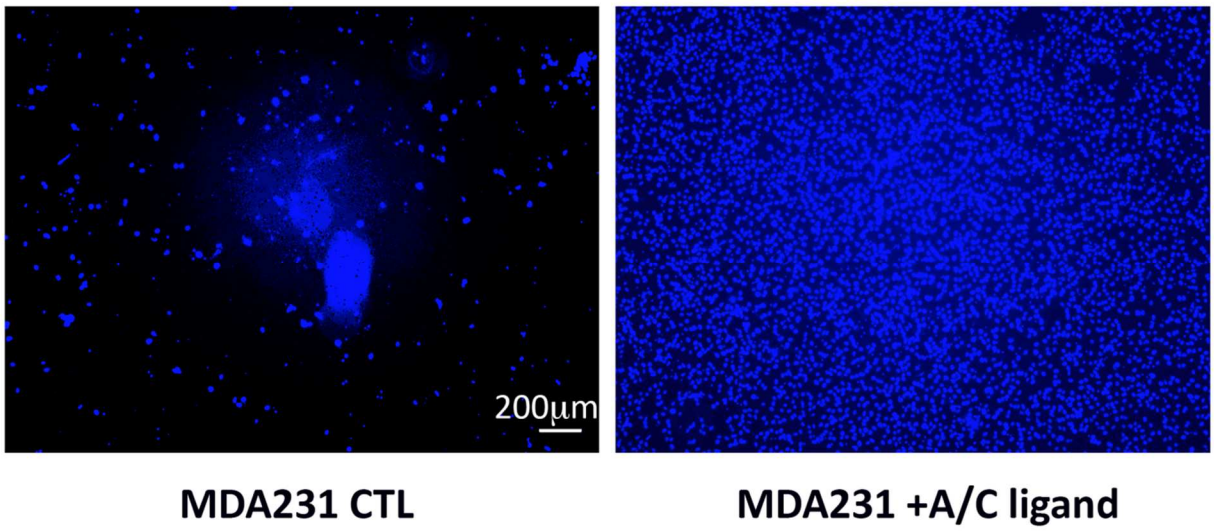

Figure S9. Matrigel images from MDA-MB-231-iDimerize-c-Met-β1 cells.
Related to **Figure 2E.** MDA-MB-231-iDimerize-c-Met-β1 cells were treated with AP21967 or vehicle (control), followed by matrigel invasion assays. AP21967increased MDA-MB-231-iDimerize-c-Met-β1 cell invasion in matrigel, as quantified in **Figure 2E** (n=6/group; P=0.007), with representative images from the assays shown here.

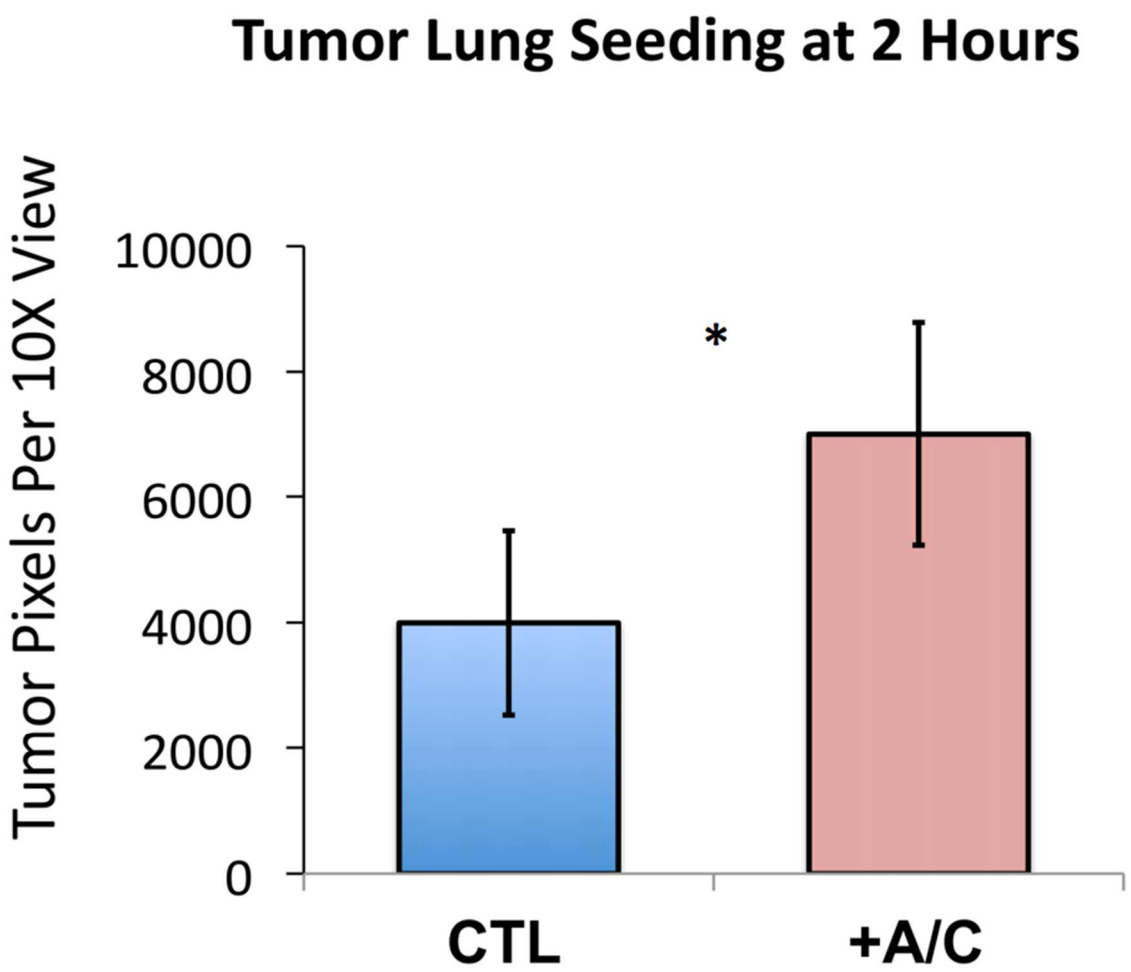

Figure S10. Quantification of lung tumor uptake by IHC assessed two hours after tail vein injection of MDA-MB-231-iDimerize-c-Met-β1 cells pre-treated with or without A/C ligand. Related to **Figure 2F**. MDA-MB-231-iDimerize-c-Met-β1 cells were pre-treated for two hours with or without AP21967, followed by tail vein injection into NSG mice (n=6 mice/group). After two hours, mice receiving AP21967-pretreated cells exhibited more human vimentin staining by IHC vs. those pre-treated with vehicle, as shown in images in **Figure 2F** and quantified here (P=0.02). * P<0.05; ** P<0.01 *** P<0.001.

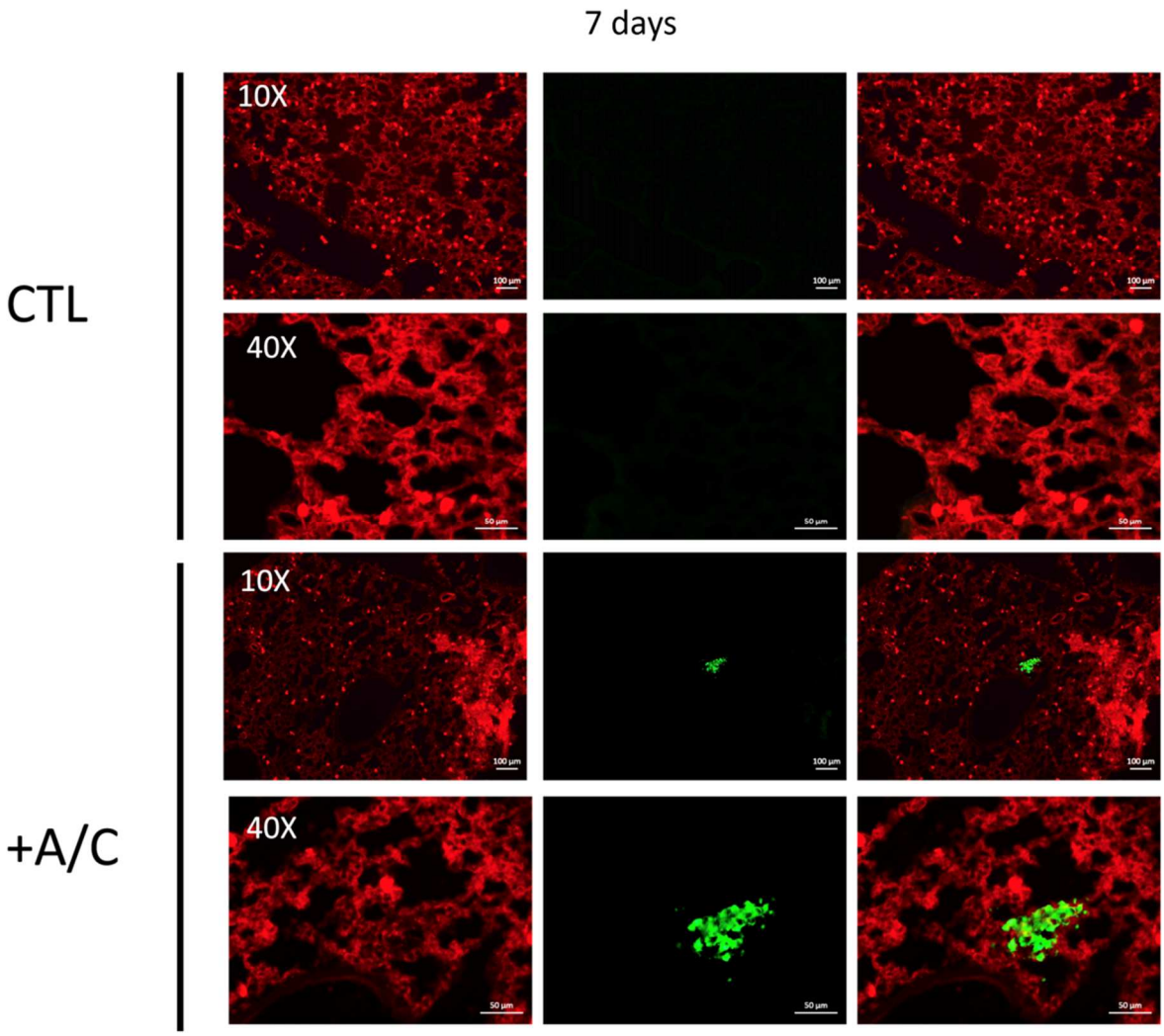

Figure S11. Additional images of lung tumor uptake by IHC assessed seven days after tail vein injection of MDA-MB-231-iDimerize-c-Met-β1 cells pre-treated with or without A/C ligand. Related to **Figure 2G**. MDA-MB-231-iDimerize-c-Met-β1 cells were pre-treated for two hours with or without AP21967, followed by tail vein injection into NSG mice (n=6 mice/group). After seven days, there were foci of nodular human vimentin staining after tail vein injection of cells pre-treated with AP21967 compared to no staining when injecting vehicle pre-treated cells (lack of staining in control group prevented statistical comparison). **Figure 2G** shows 40x magnification. Here we show 10x magnification alongside 40x.

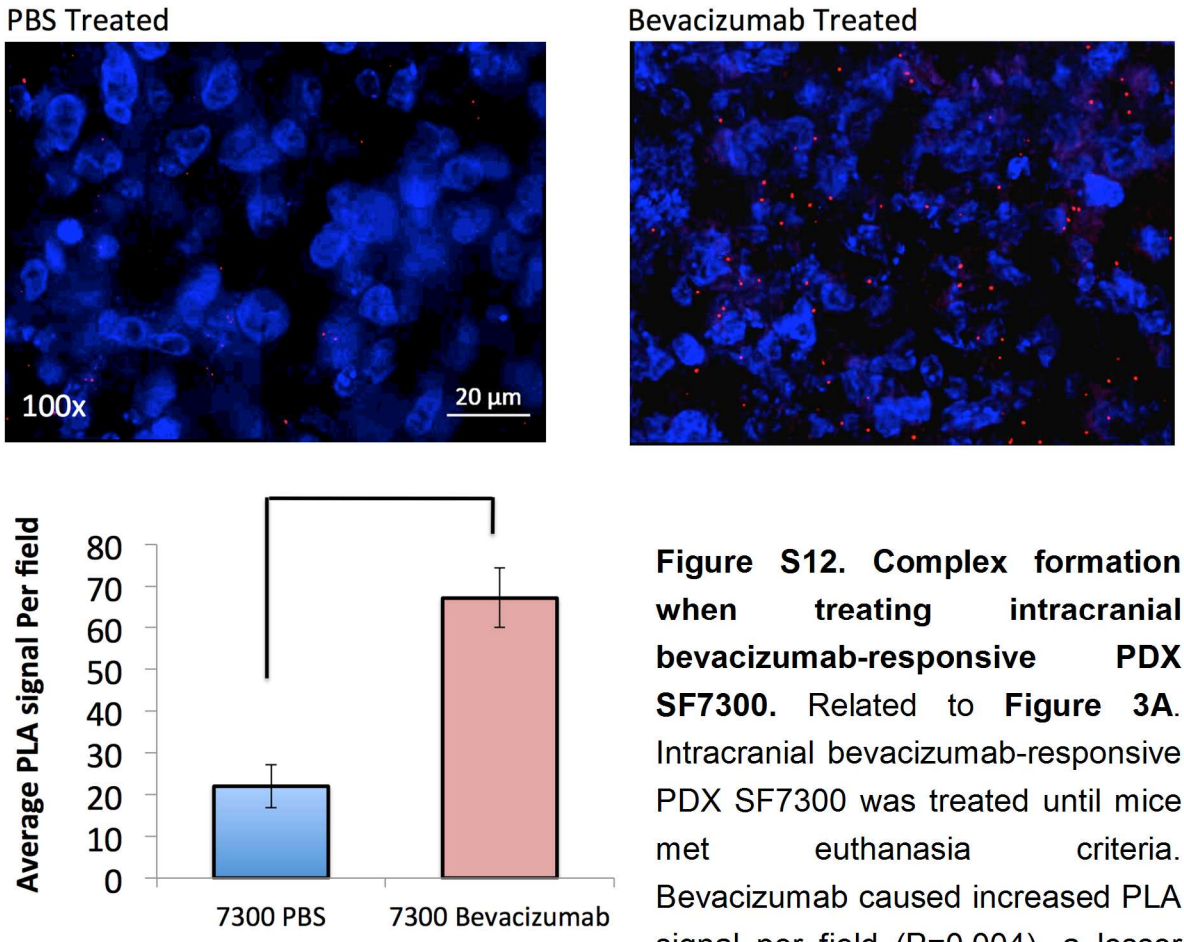

Figure S12. Complex formation when treating intracranial bevacizumab-responsive PDX SF7300. Related to **Figure 3A**. Intracranial bevacizumab-responsive PDX SF7300 was treated until mice met euthanasia criteria. Bevacizumab caused increased PLA signal *per field* (P=0.004), *a lesser* increase than seen when intracranial bevacizumab-resistant SF7796 PDXs were treated **(Figure 3),** suggesting that intracranial bevacizumab-responsive PDXs treated to endpoint exhibited early signs of the resistant phenotype that became more robustly established in the resistant PDXs.

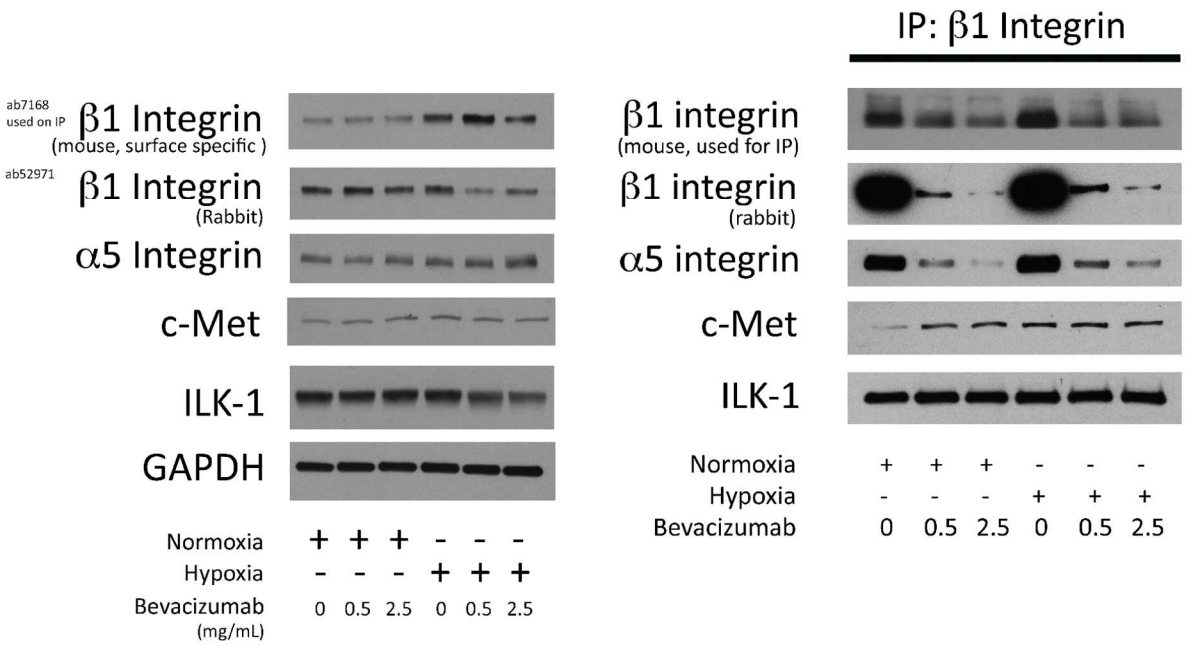

Figure S13. Western blots on whole cell lysates and immunoprecipitates of cultured GBM cells treated with bevacizumab in normoxia vs. hypoxia. Related to **Figure 3D**. U87 cells were treated in hypoxia (1% oxygen) or with bevacizumab (0.5 or 2.5 mg/mL) for 48 hours. Shown to the left are the western blots from whole cell lysates, while shown to the right are the blots from β1 integrin immunoprecipitates generated using mouse ab7168. Interestingly, bevacizumab reduced the ability of rabbit ab52971 to recognize β1 integrin in the immunoprecipitates, but β1 integrin levels did not change in response to bevacizumab based on the other blots.

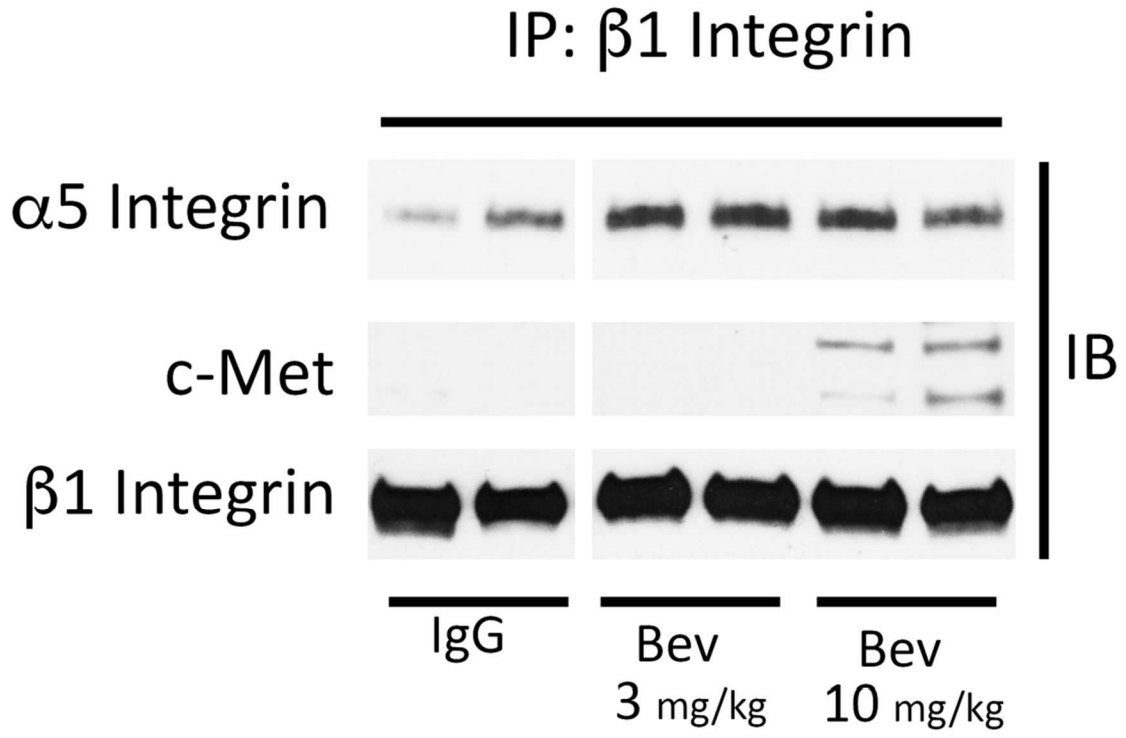

Figure S14. Western blots on whole cell lysates and immunoprecipitates of cultured GBM cells treated with bevacizumab in normoxia vs. hypoxia. Related to **Figure 3**. Subcutaneous U87 xenografts were treated with IgG and bevacizumab at 3 and 10 mg/kg, with tumor lysate IP revealing dosedependent c-Met/β1 integrin binding.

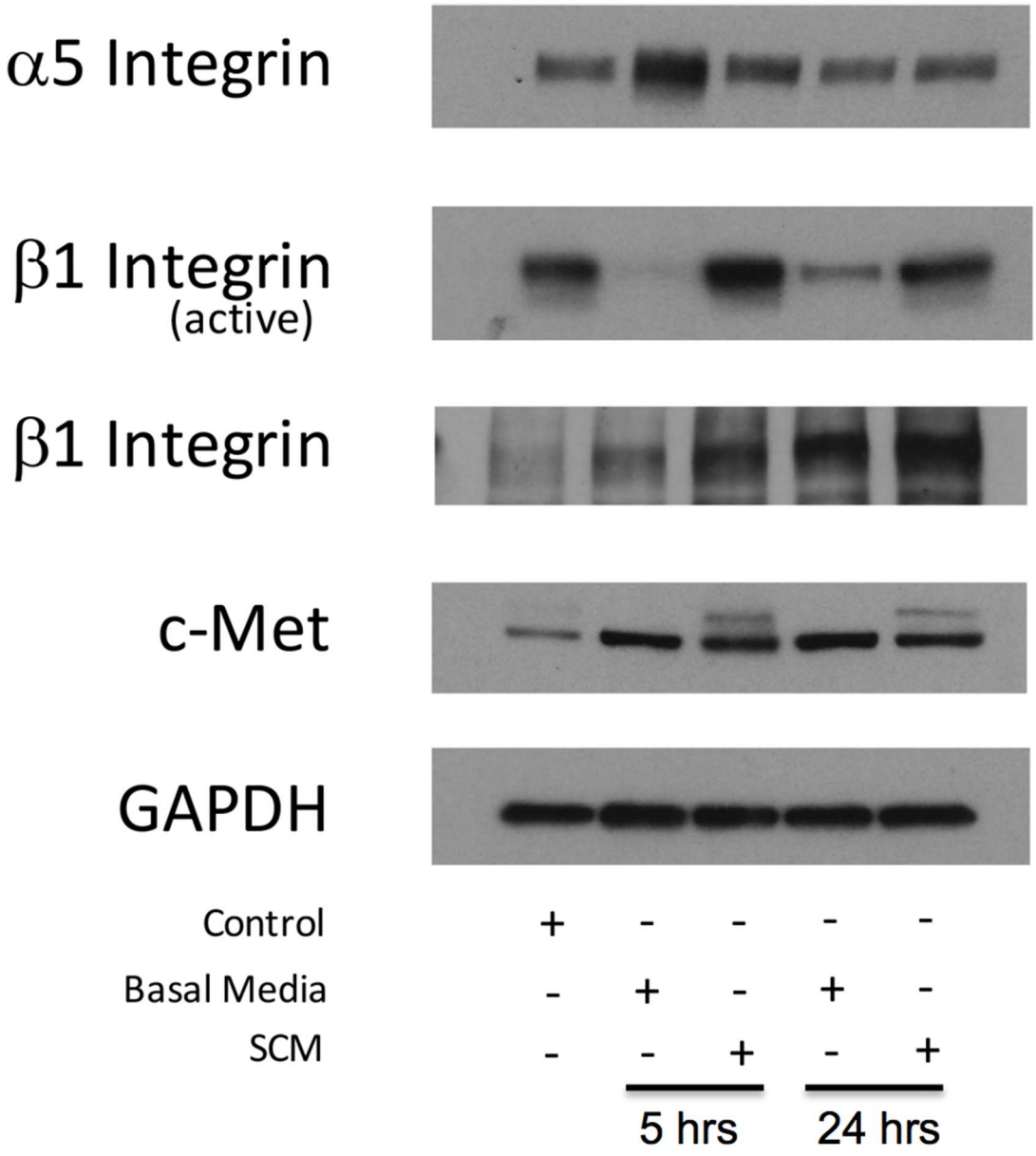

Figure S15. Western blots on whole cell lysates of cultured GBM cells treated with endothelial cell conditioned media. Related to **Figure 4A**. U87 cells were grown in basal HUVEC media or HUVEC serum conditioned media (SCM) for 5 or 24 hours, after which the whole cell lysates underwent western blotting for the antigens shown here.

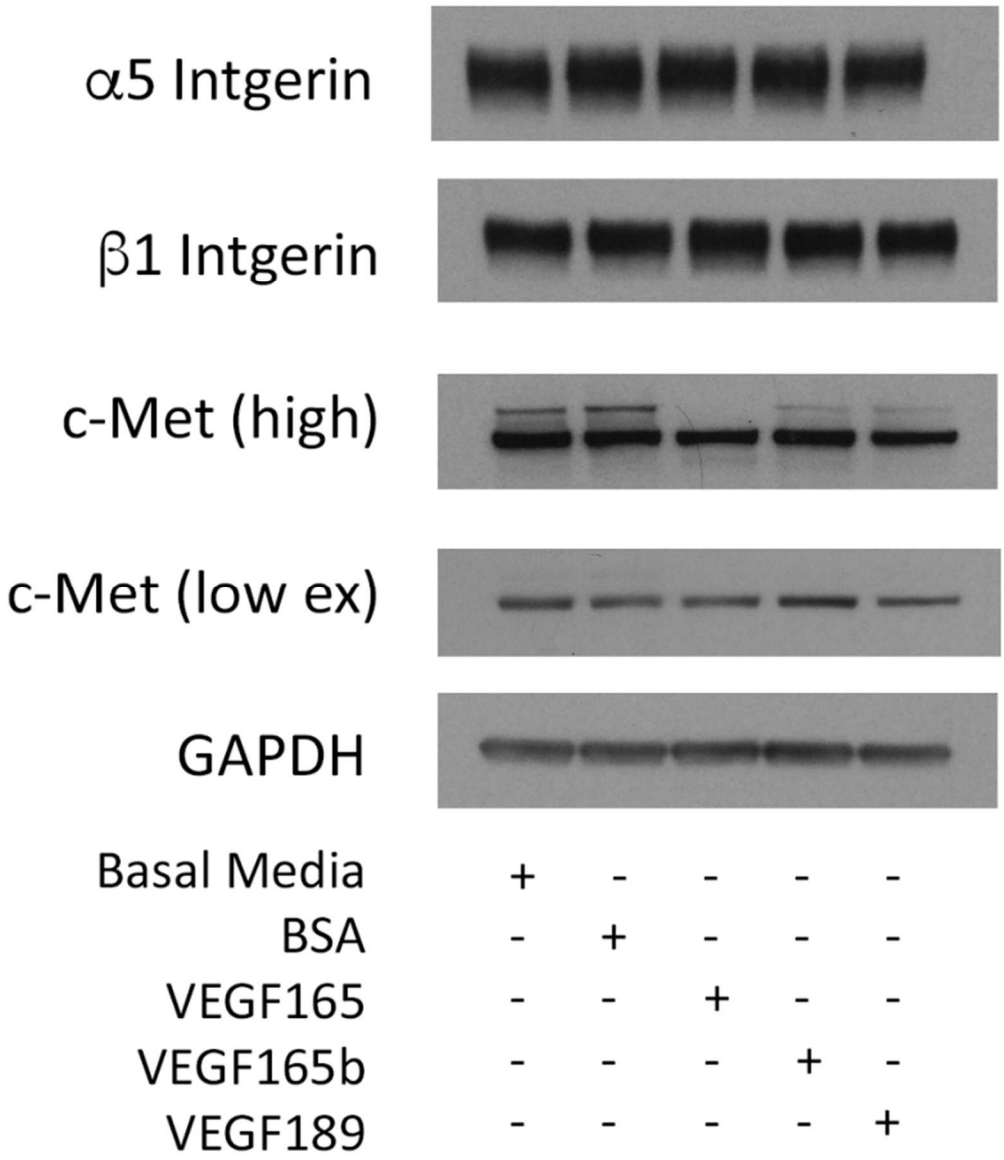

Figure S16. Western blots on whole cell lysates of cultured GBM cells treated with various VEGF isoforms. Related to **Figure 4B**. U87 cells were incubated with basal media or 100 ng/mL BSA, VEGF165, VEGF165b, or VEGF189 for 2 hours, as shown in **Figure 4B**, after which western blots were performed on the whole cell lysates for the antigens shown here.

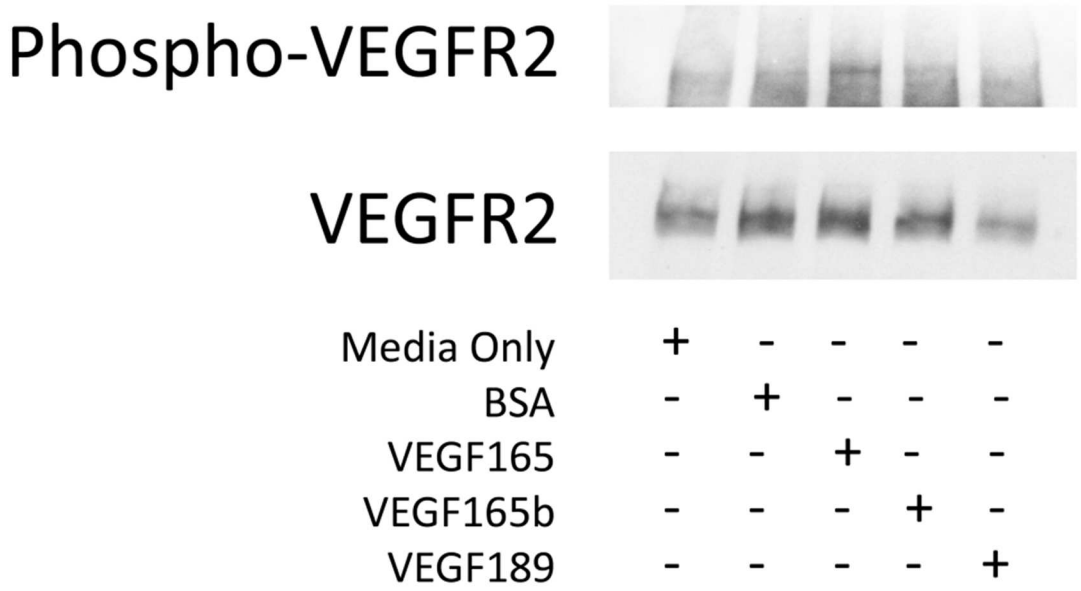

Figure S17. VEGF165 induces VEGFR2 phosphorylation more than VEGF165b or VEGF189 in cultured GBM cells. Related to **Figure 4B**. U87 cells were incubated with basal media or 100 ng/mL BSA, VEGF165, VEGF165b, or VEGF189 for 2 hours, as shown in **Figure 4B**, with levels of phosphorylated and total VEGR2 assessed by western blot.

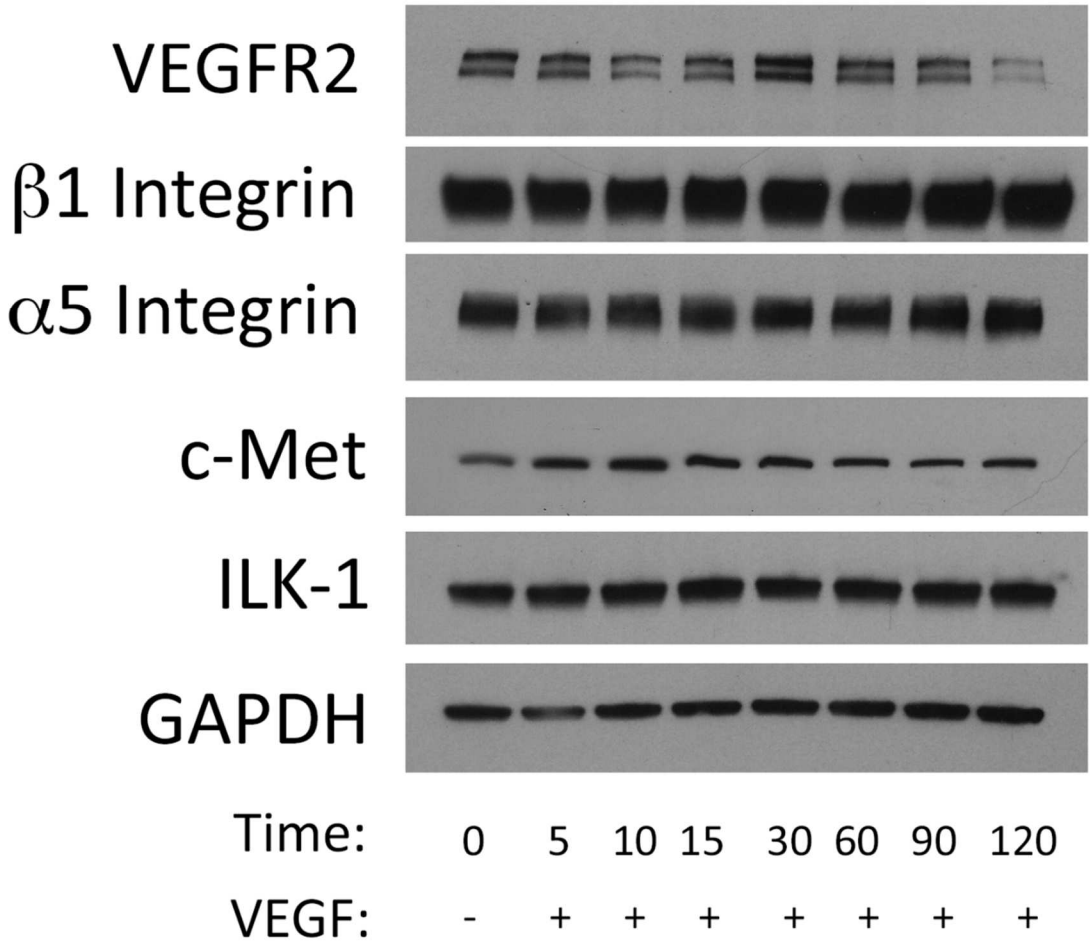

Figure S18. Western blots on whole cell lysates of cultured GBM cells treated with endothelial cell conditioned media or various VEGF isoforms. Related to **Figures 4C-D**. U87 cells were treated with VEGF165 for variable time points shown here in minutes, as described in **Figures 4C-D**. Western blots for the antigens listed here were then performed on the resulting whole cell lysates.

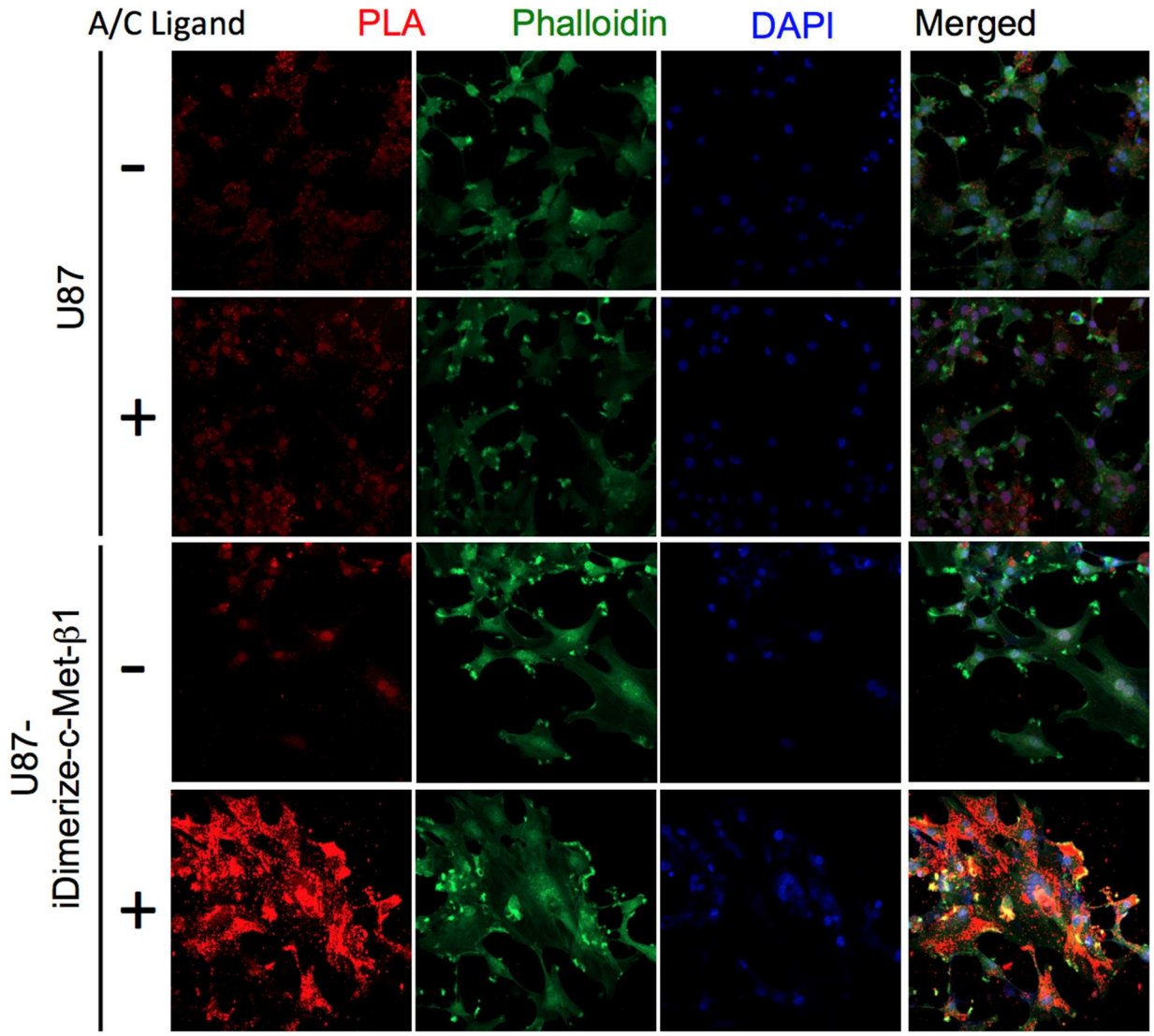

Figure S19. Induction of c-Met/b1 integrin binding assessed by PLA in GBM cells. U87 cells without or with inducible heterodimerization were plated on chamber slides and treated with or without A/C ligand for 12 hours, after which PLA was performed to measure c-Met/b1 integrin complex formation. At the same exposure used in **Figure S3**, the more robust expression of the inducible heterodimerization system in U87 cells compared to MDA-MB- 231 cells led to saturated red staining requiring lower exposure to quantify (**Figure S11**). 100x, scale bars 50 mm.

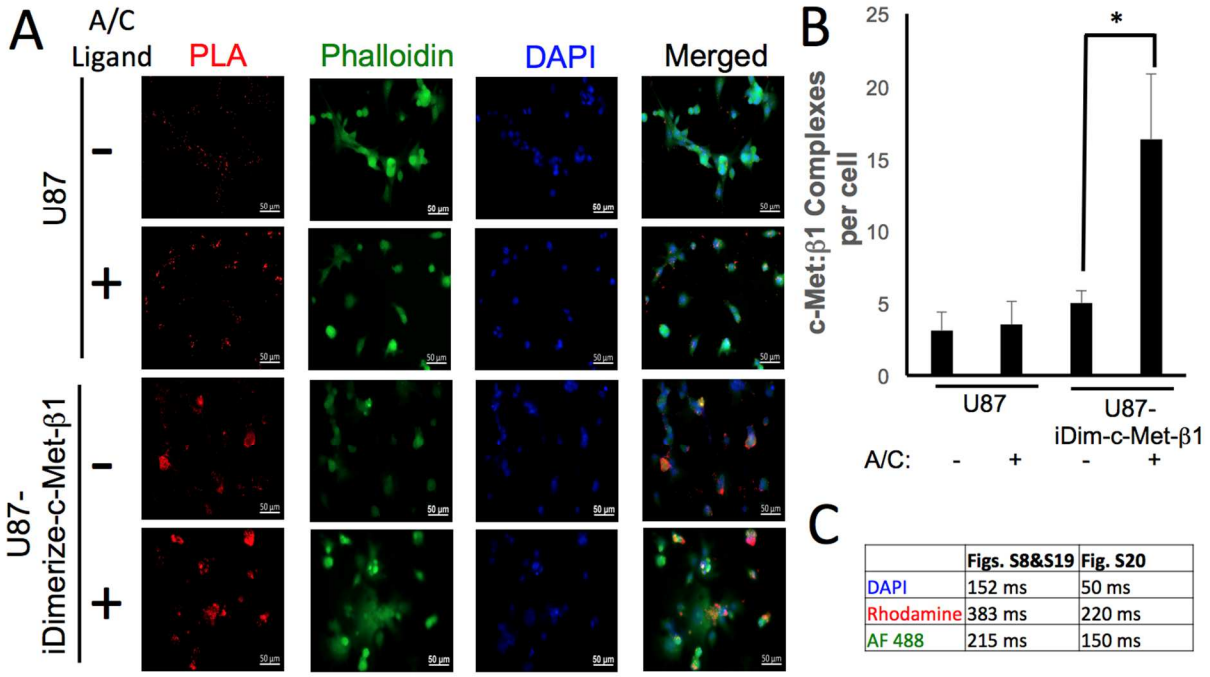

Figure S20. Induction of c-Met/β1 integrin binding assessed by PLA in GBM cells. **(A)** U87 cells without or with inducible heterodimerization were plated on chamber slides and treated with or without A/C ligand for 12 hours, after which PLA was performed to measure c-Met/β1 integrin complex formation. Using a lower exposure than used in **Figures S8 and S19** due to the more robust expression of the inducible heterodimerization system in U87 cells compared to MDA-MB- 231 cells, the red PLA staining could be visualized. **(B)** Quantification of PLA signals per cell revealed a robust increase when A/C was added to U87-iDimerize-c-Met-b1 (P=0.01), with no increase occurring when A/C was added to U87 (P=0.7). **(C)** Specific exposure times by channel used in **Figures S8 and S19** versus **S20**. 100x magnification, scale bars 50 μm. * P<0.05; ** P<0.01 *** P<0.001.

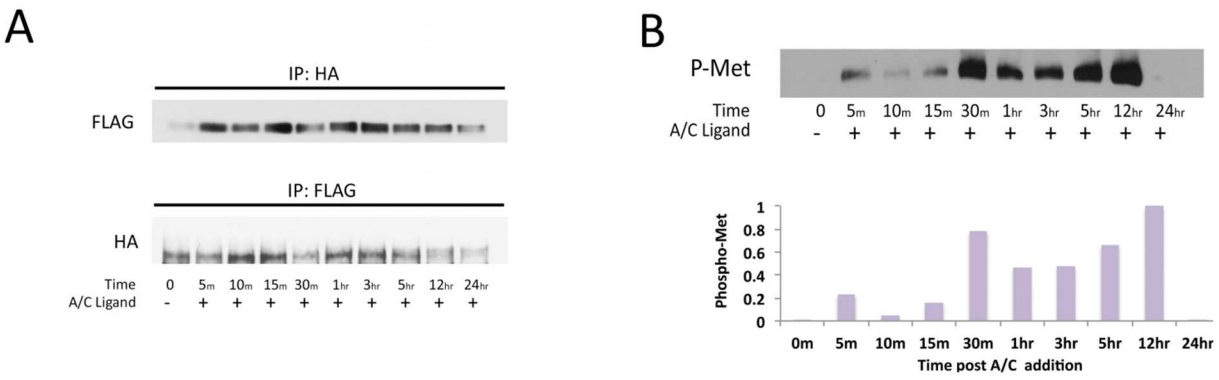

Figure S21. Inducing c-Met/β1 integrin binding in GBM cells. (A) U87 and U251 GBM cells were engineered to express HAtagged β1 integrin and FLAG-tagged c-Met fused to FRB (DmrC) and FKBP (DmrA) respectively. Engineered U87 cells were then treated with AP21967 or vehicle, after which HA and FLAG IP were used to confirm that AP21967 induced c-Met/β1 integrin binding. **(B)** Western blot was used to show increased c-Met phoshorylation after inducing c-Met/b1 integrin binding by treating U87-iDimerize-c-Met-β1 cells with AP21967.

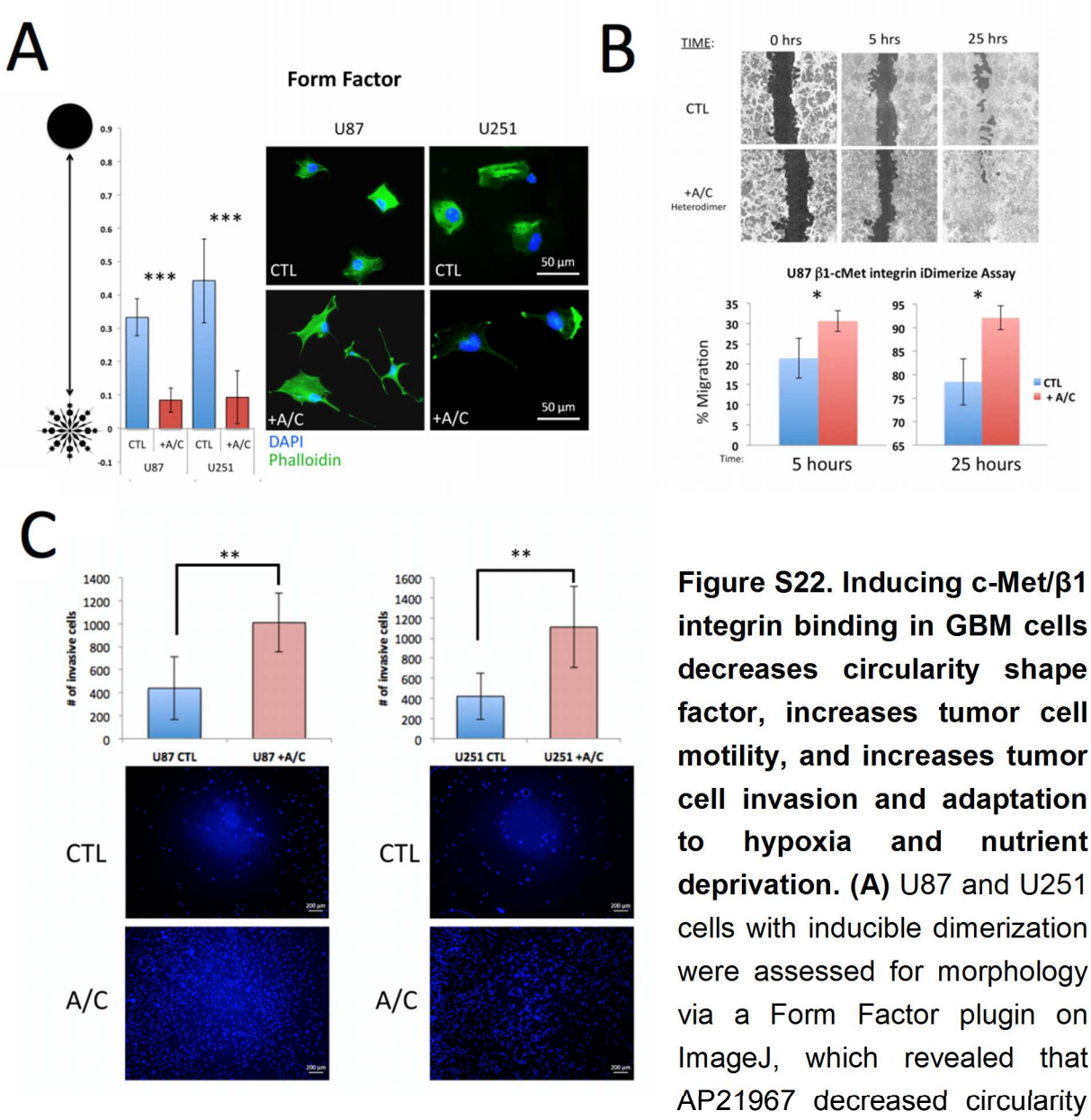

Figure S22. Inducing c-Met/β1 integrin binding in GBM cells decreases circularity shape factor, increases tumor cell motility, and increases tumor cell invasion and adaptation to hypoxia and nutrient deprivation. (A) U87 and U251 cells with inducible dimerization were assessed for morphology via a Form Factor plugin on ImageJ, which revealed that AP21967 decreased circularity shape factor in both (P=1.6 X10-6–2.1X10-7). **(B)** U87-iDimerize-c-Met-β1 cells were scratched, and assessed after 5 and 25 hours via mosaic imaging and analyzed using the T-Scratch software to confirm that AP21967 induced migration (P=0.006 at 5 and 25 hours; n=6/group). **(C)** AP21967 also increased invasion of U87 (P=0.004) and U251 (P=0.007) cells with inducible dimerization in matrigel chambers (n=6/group). * P<0.05; ** P<0.01 *** P<0.001.

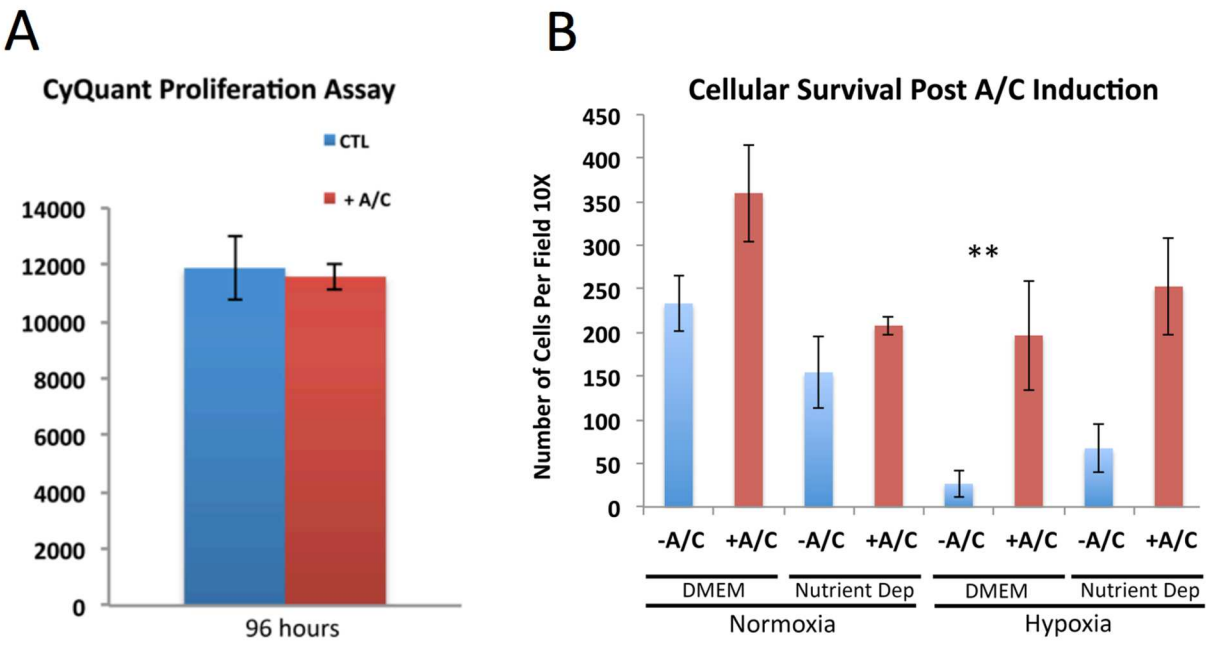

Figure S23. Inducing c-Met/β1 integrin binding does not alter tumor cell proliferation, and increases adaptation to hypoxia and nutrient deprivation. (A) U87 cells with inducible heterodimerization were allowed to proliferate up to 96 hours, and assessed via CyQuant proliferation kit with no change in proliferation (P=0.2). **(B)** AP21967 improved survival of U87-iDimerize-c-Met-β1 cells incubated in hypoxia, with effects in nutrient (serum) deprivation not reaching significance (P=0.008 three way ANOVA for AP21967-hypoxia interaction, P=0.4 three way ANOVA for AP21967-nutrient deprivation interaction; n=3/group). * P<0.05; ** P<0.01 *** P<0.001.

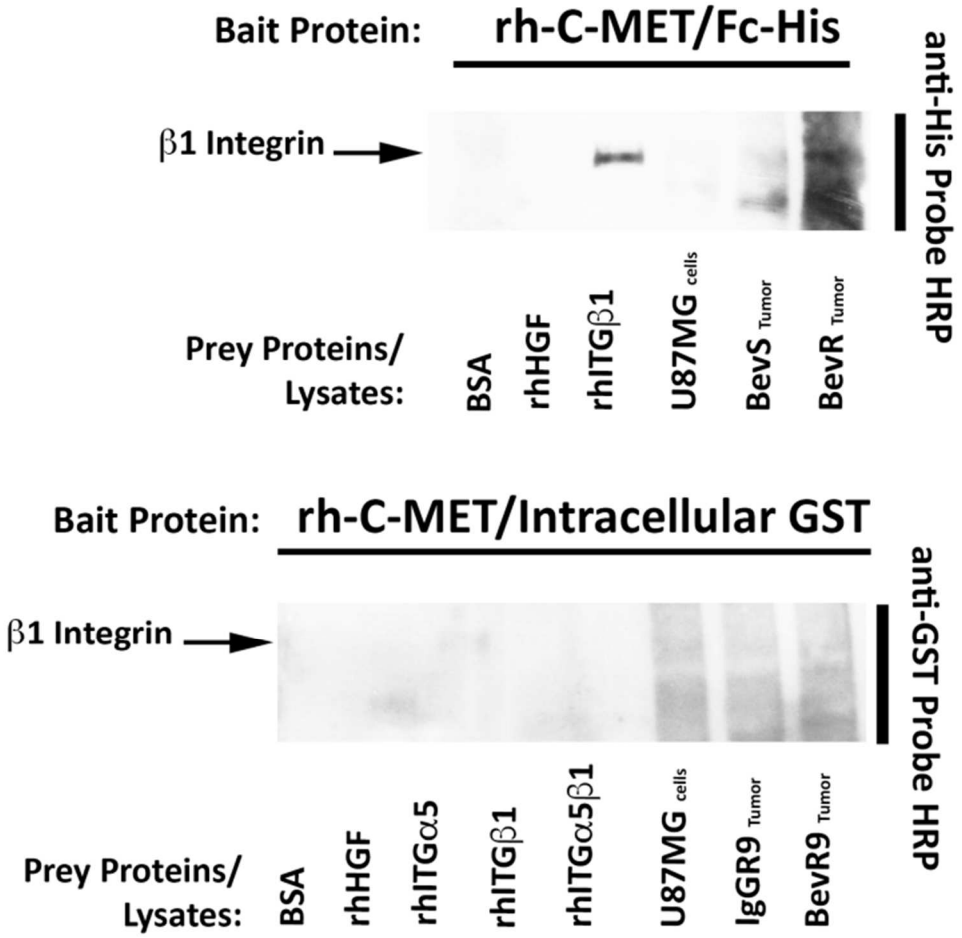

Figure S24. Expanded far western blot of xenografts reveals more robust β1 to bind the extracellular, not the intracellular, c-Met domain in U87-BevR, not U87-BevS, xenografts. Related to Figure 5B. Expansion of far western blot from Figure 5B showing that lysates from U87-BevR tumors bound exracellular, not intracellular, c-Met better than lysates from U87-BevS tumors or U87 parental GBM cells, likely indicating greater availability of β1 integrin in the U87-BevR lysates.

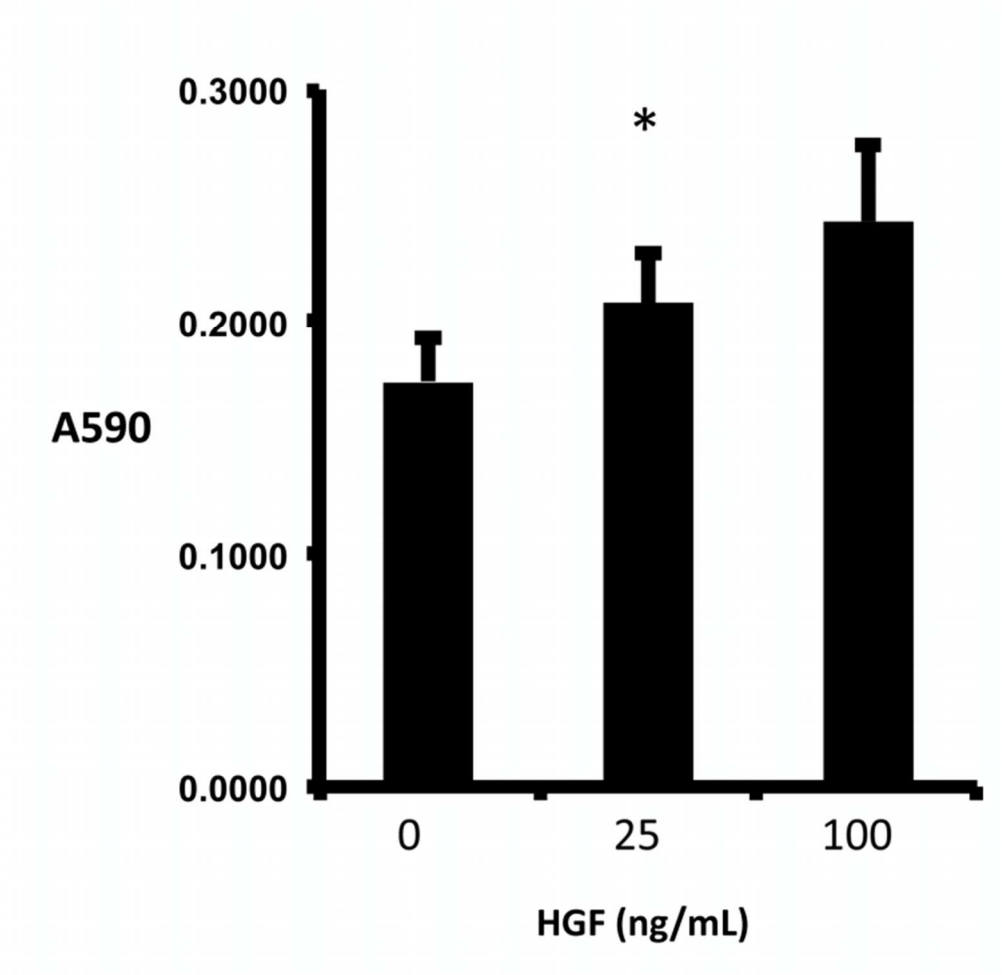

Figure S25. Impact of HGF on adhesion of U87 cells to fibronectin. Related to **Figure 5**. U87 cells exhibited increased adhesion to fibronectin in response to increasing HGF (P=0.02). * P<0.05; ** P<0.01 *** P<0.001.

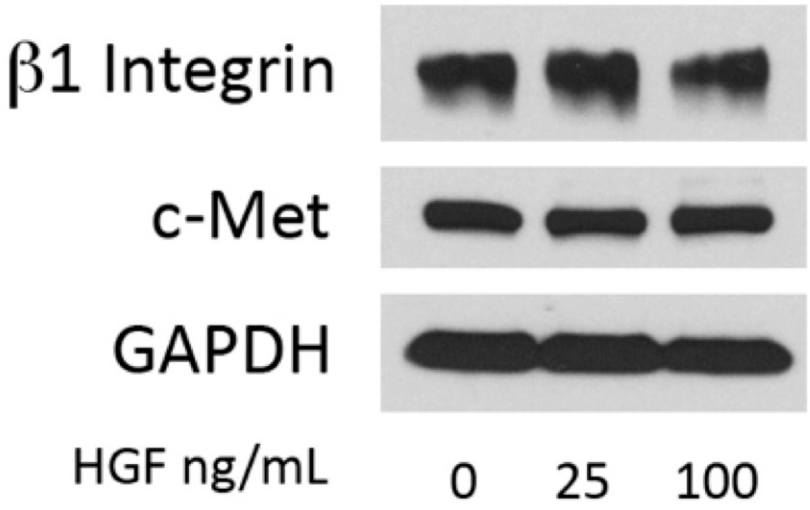

Figure S26. HGF does not alterβ1 integrin expression. Related to **Figure 6**. Western blot from U87 cells exposed to the same concentrations of HGF for the same durations as in **Figure 3b** revealed no changes inβ1 integrin expression, suggesting that the increased adhesion seen in **Figure 3b** reflected alteredβ1 integrin activation rather than expression.

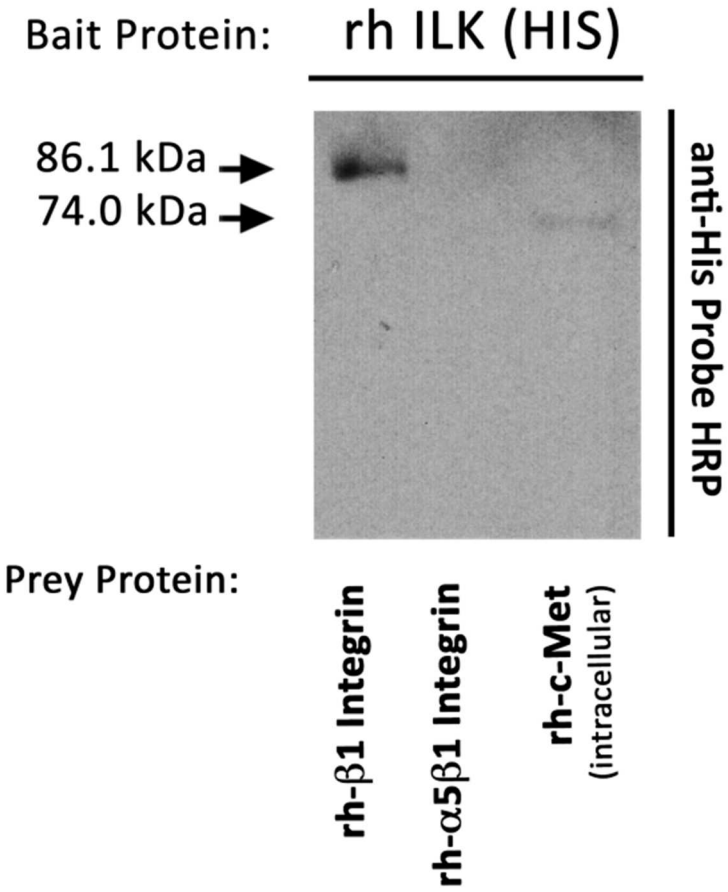

Figure S27. ILK binds c-Met. Related to **Figure 5.** Far western blot to assess whether ILK binds c-Met. His-tagged recombinant human ILK was bait with β1 integrin, α5β1 integrin, or c-Met as prey.

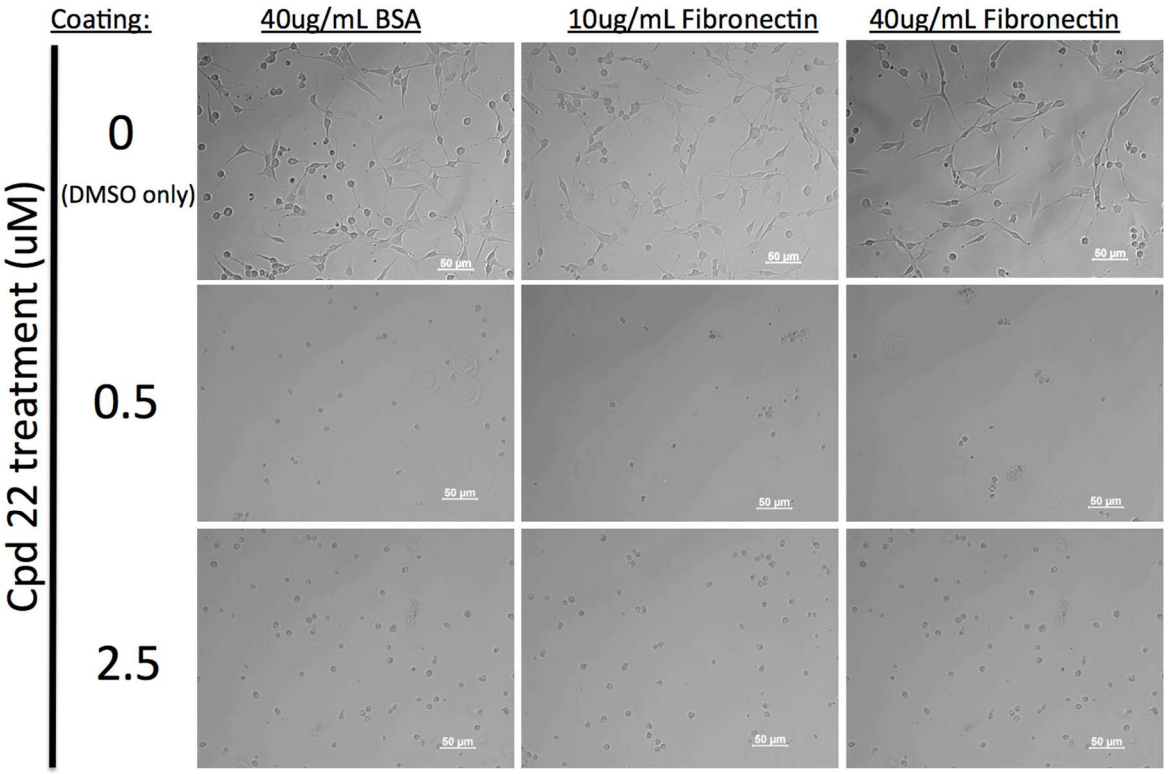

Figure S28. Impact of ILK inhibitor on tumor cell morphology and adhesion. Related to **Figure 5**. ILK inhibitor Cpd 22, which is shown in **Figure 6** to prevent fibronectin-induced c-Met phosphorylation, changed morphology of U87 cells to a more circular morphology and reduced adhesion to fibronectin. 20x magnification; scale bars 50 mm.

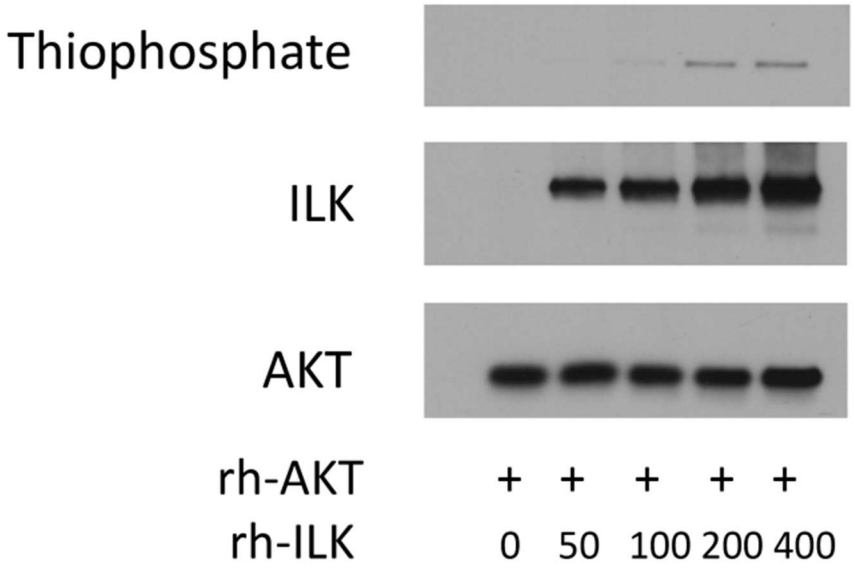

Figure S29. ILK phosphorylates AKT. Related to **Figure 5**. Recombinant ILK was incubated with recombinant kinase-null human AKT (ng of protein shown below each lane) and ATPγS. Thiophosphate western blotting revealed concentration-dependent increases in AKT phosphorylation.

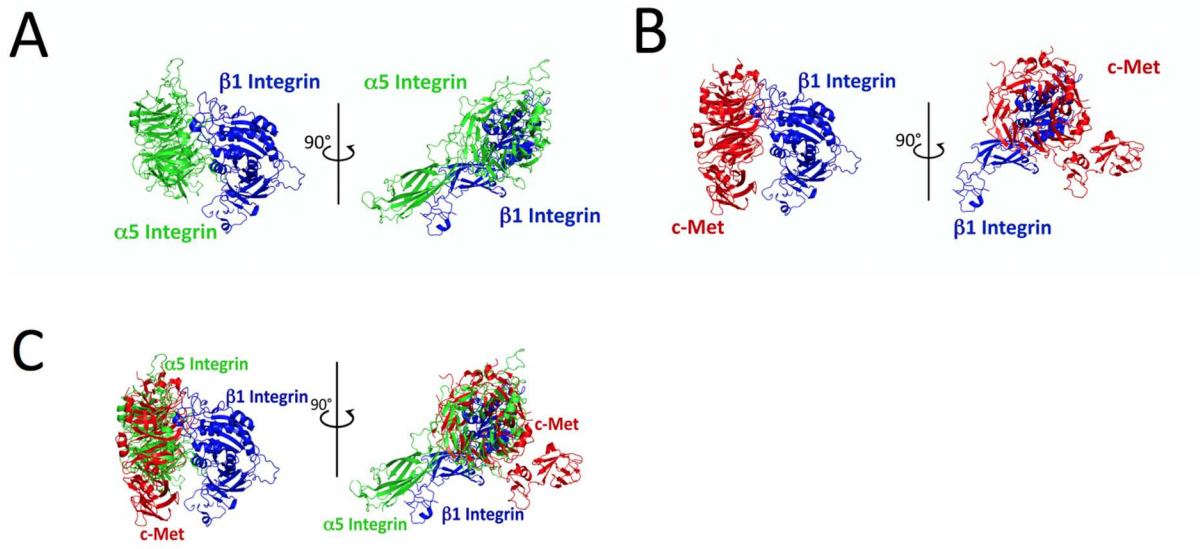

Figure S30. Structural modeling of α5/β1 and c-Met/β1 integrin complex. Related to **Figure 6**. PyMOL crystal structure software analysis defined **(A)** the structure of the heterodimer formed by α5 integrin (green) and β1 integrin (blue); **(B)** the structure of the c-Met/β1 complex; and **(C)** the likelihood that c-Met (red) displaces α5 (green) from its β1 (blue) binding site due to similar c-Met and α5 propeller regions.

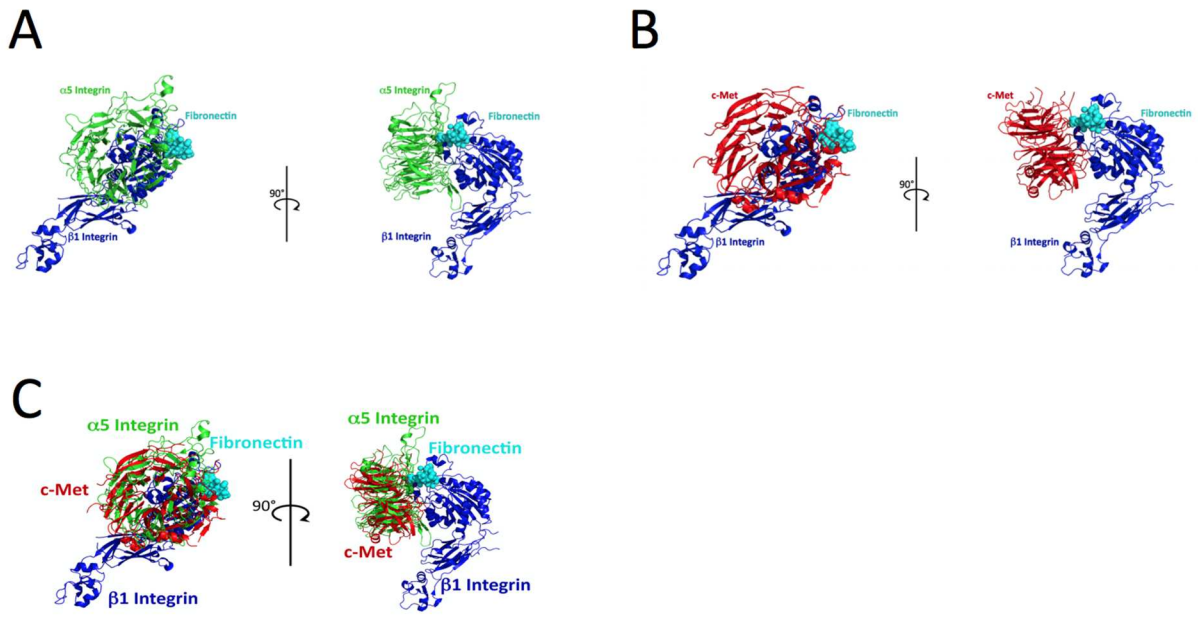

Figure S31. Structural modeling of α5/β1 and c-Met/β1 integrin complex as they bind to fibronectin. Related to **Figure 6.** PyMOL crystal structure software analysis defined **(A)** the structure of the heterodimer formed by α5 integrin (green) and β1 integrin (blue) as it binds to fibronectin (cyan); **(B)** the structure of the c-Met (red) and β1 complex, which creates a similar pocket allowing for fibronectin (cyan) to bind; and **(C)** the finding that c-Met, after replacing α5, binds fibronectin (cyan) through the same Arg-Gly-Asp motif as α5.

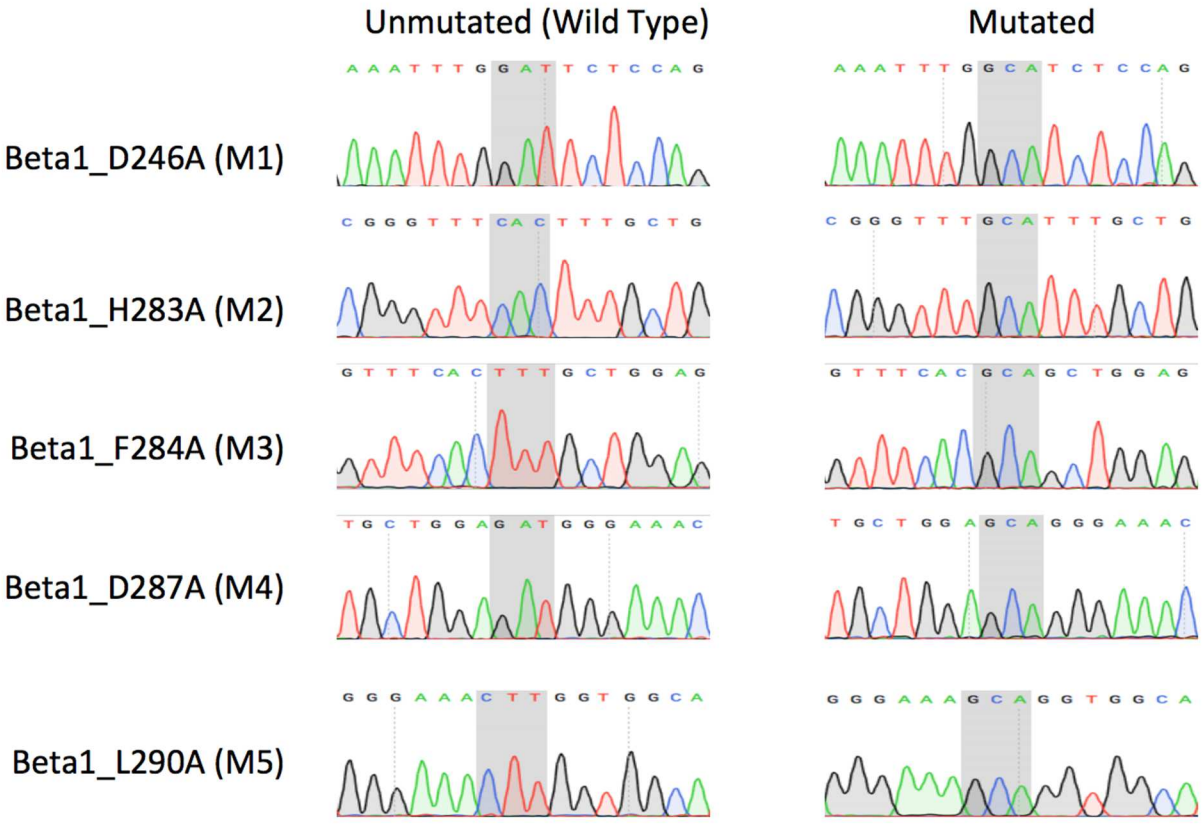

Figure S32. Sequencing results from engineered mutations inβ1 integrin created to disrupt c-Met/b1 integrin binding based on results of PyMOL modeling. Related to **Figure 6**. Based on PyMOL crystal structure software analysis, the Rosetta ALA scanning method was used to determine predicted changes in delta-delta-G that would arise by disrupting specific amino acids inβ1 integrin, with higher scores associated with more loss of c-Met/b1 integrin binding. The 3 nucleotides coding for the amino acids with the five highest scores were converted from their original sequence to 'GCA' in order to obtain alanine residues, with the resulting sequence changes shown here.

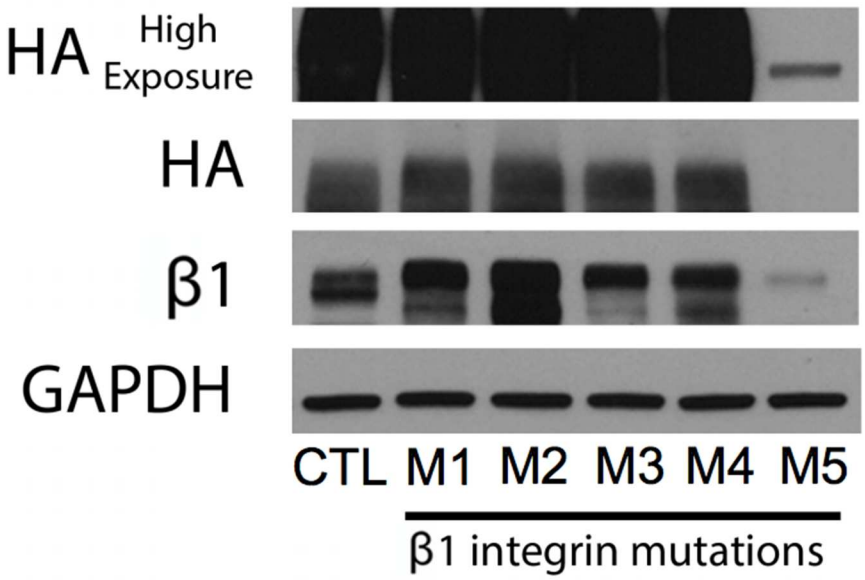

Figure S33. Whole cell lysates from HEK cells expressing wild type β1 integrin-HA fusion protein and five mutant β1 integrin-HA fusion proteins. Related to **Figure 6F**. The five β1 integrin mutations suggested by PyMOL crystal structure software and the Roseta ALA method were created in a β1 integrin-HA fusion protein with the resulting cDNAs transfected into HEK cells. After cell selection, whole cell lysates underwent western blotting for the proteins shown above. The presence of the HA tag was confirmed in HEK cells expressing wild type β1 integrin-HA fusion protein and the five mutations, with the M5 mutation-HA fusion protein less robustly expressed than wild type protein or mutations M1-M4, such that a higher exposure was required to visualize HA in HEK cells expressing the M5-HA fusion protein.

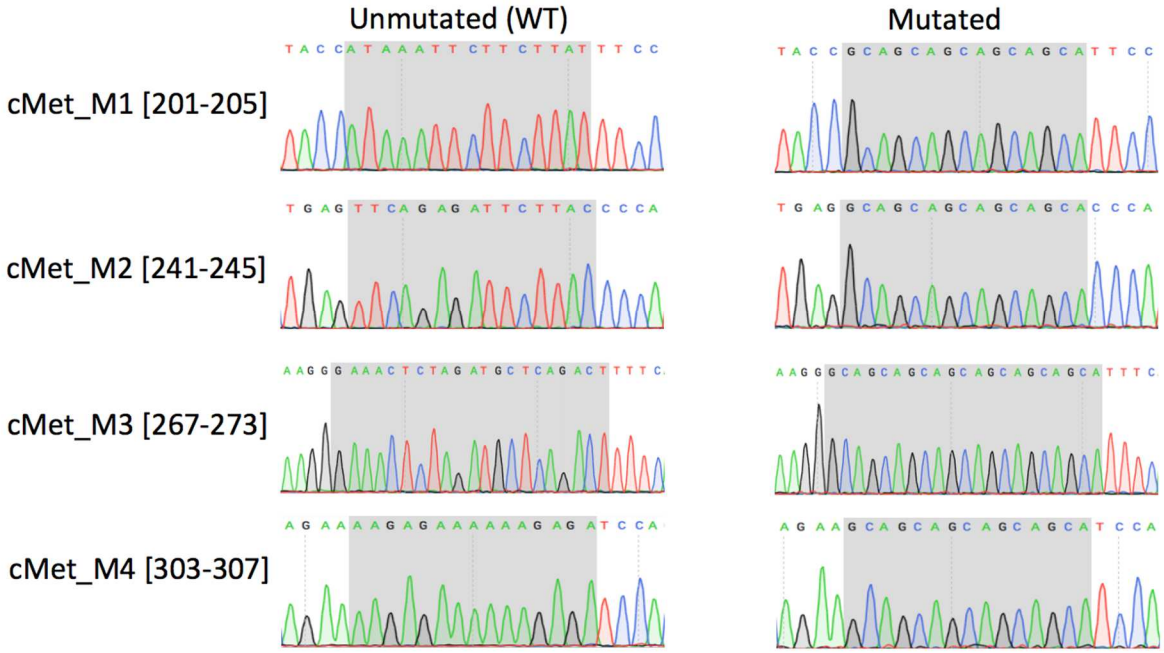

Figure S34. Sequencing results from engineered mutations in c-Met created to disrupt c-Met/b1 integrin binding based on PyMOL modeling. Related to **Figure 6**. Because the Rosetta ALA scanning method could not be used to predict changes in delta-delta-G that would arise by disrupting specific amino acids in c-Met due to the model interface not being sufficiently accurate, based on PyMOL analysis predicting that the loops on the top of the 7-bladed b-propeller domain of c-Met would contactβ1 integrin, we investigated whether disrupting these loops atop the b-propeller domain of c-Met would affect c-Met/b1 integrin binding. The nucleotides coding for the amino acids in four of these five loops were converted from their original sequences to a series of ‘GCA’s in order to obtain alanine residues, with the resulting sequence changes shown here. The genetic change required to alter the fifth loop in amino acids 348-359 failed to be established correctly after multiple attempts at mutagenesis and sequencing and was thus not used.

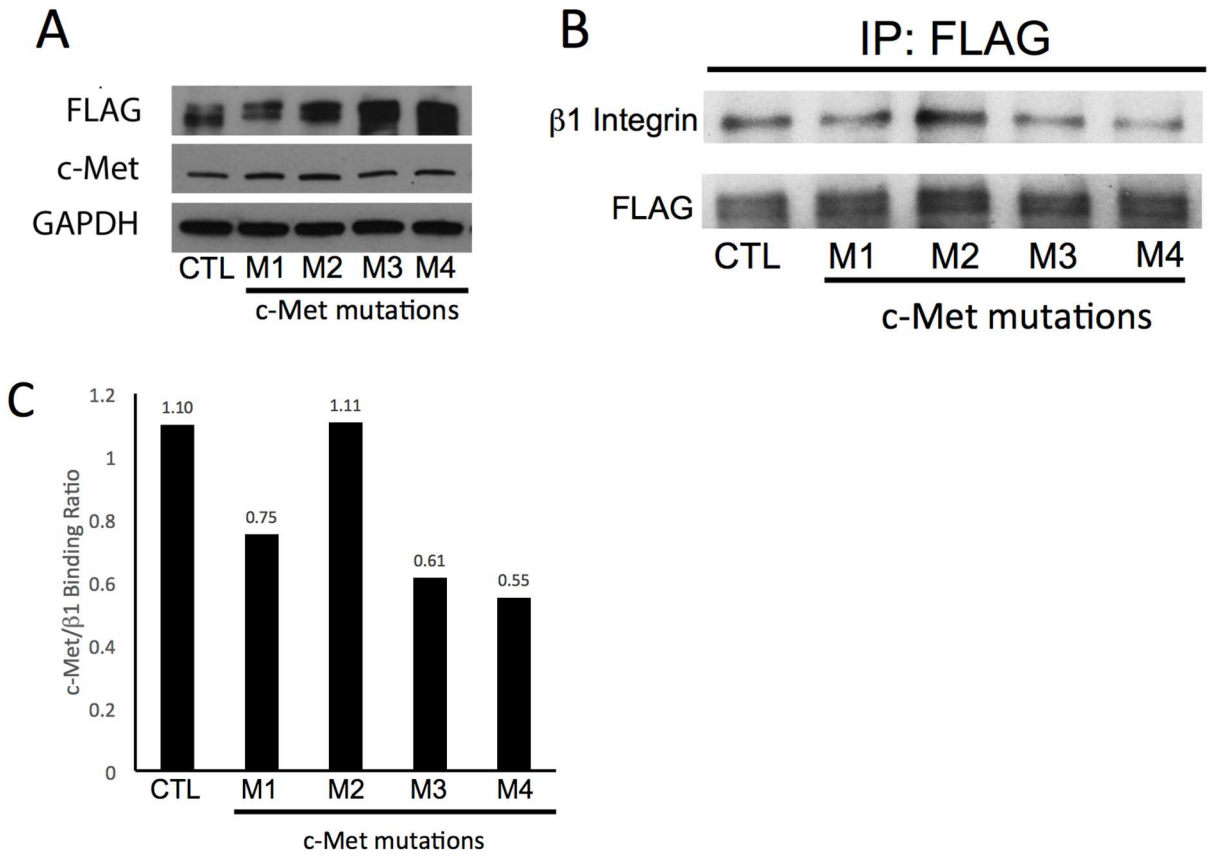

Figure S35. Mutations in the c-Met propeller residues affect c-Met/b1 integrin binding Related to **Figure 6**. The mutations in the upper loops of the propeller region of c-Met that we created in **Figure S20** were engineered into a c-Met-FLAG fusion protein and then transfected into HEK cells. (**A**) Western blot of resulting whole cell lysates revealed FLAG expression in cells with wild type and the four mutants analyzed. (**B**) Immunoprecipitates generated from these cells using a FLAG antibody were blotted forβ1 integrin and FLAG, revealing variable levels of c-Met/b1 binding depending on the mutation. (**C**) The c-Met/b1 binding ratio, representing the ratio ofβ1 integrin to FLAG band intensities calculated using densitometry of the bands in (**B**), was comparable to wild-type with c-Met mutant M2, but reduced with increasing magnitude from M1 to M3 to M4.

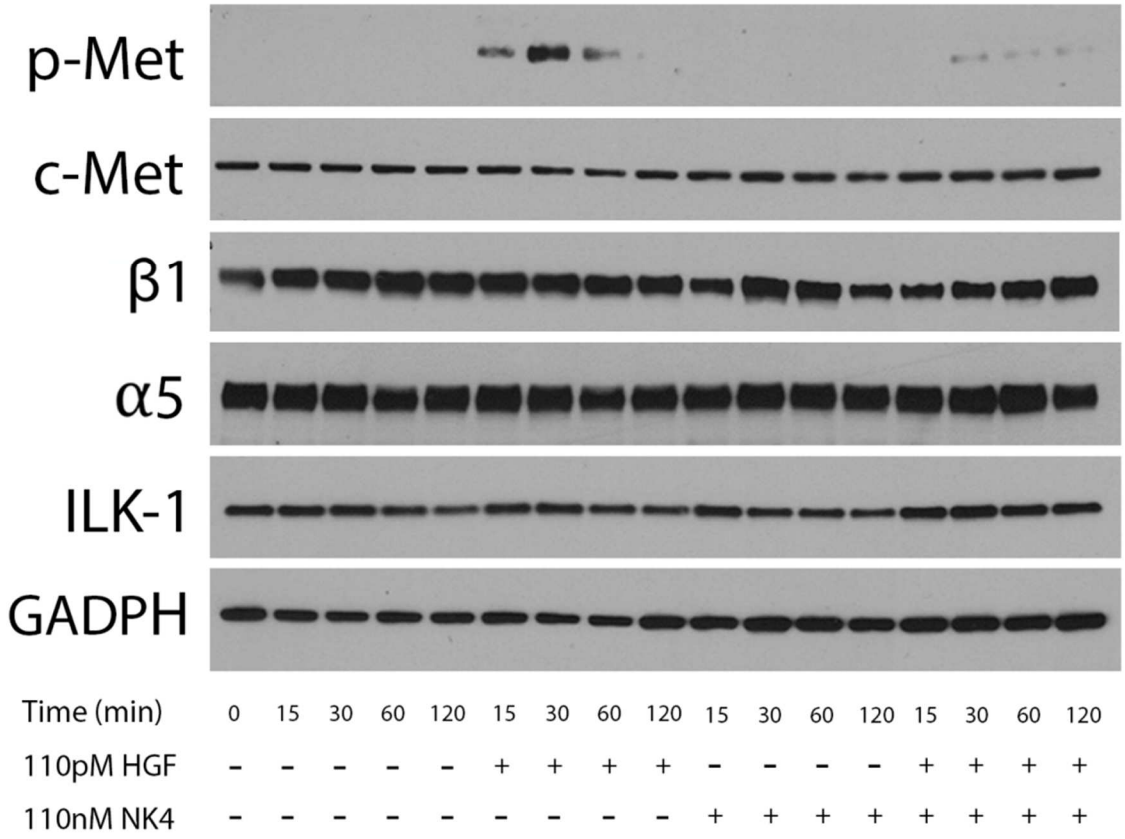

Figure S36. Effect of c-Met/HGF therapeutic antagonist NK4 on c-Met phosphorylation. Related to **Figure 6**. Cultured U87 cells were treated with 110 pM HGF and/or 110 nM of c-Met/HGF therapeutic antagonist NK4 for varying times. Western blots of whole cell lysates revealed that HGF led to c-Met phosphorylation peaking at 30 minutes, while NK4 did not affect c-Met phosphorylation and adding NK4 to HGF led to a diminished level of c-Met phosphorylation compared to HGF alone.

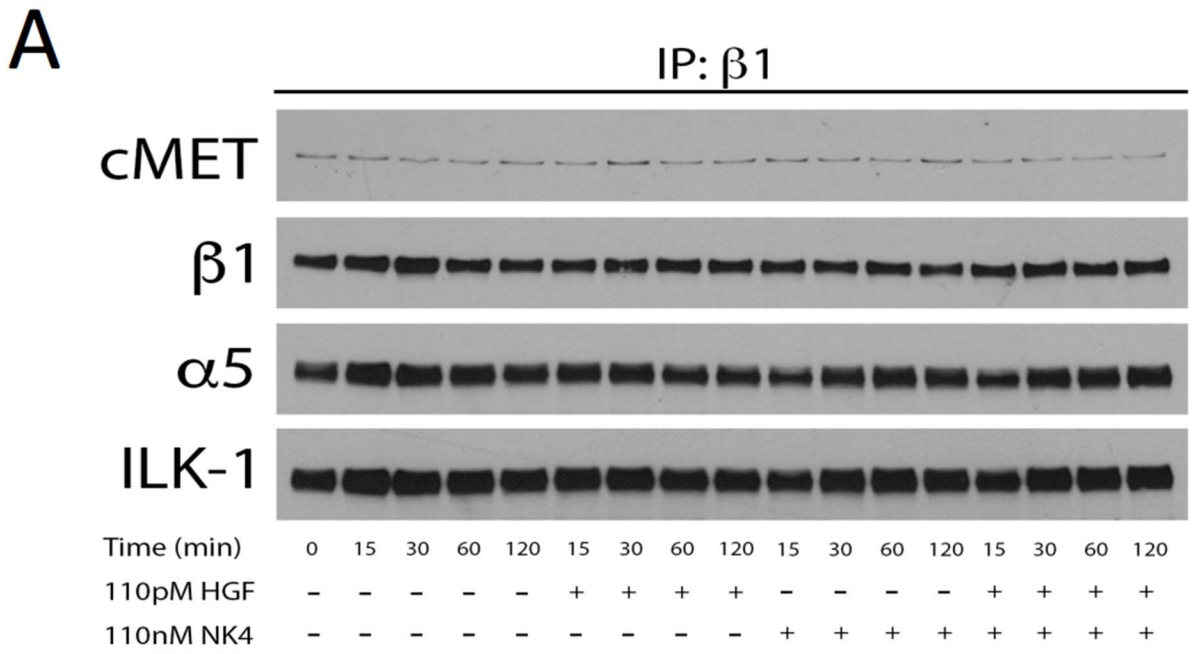

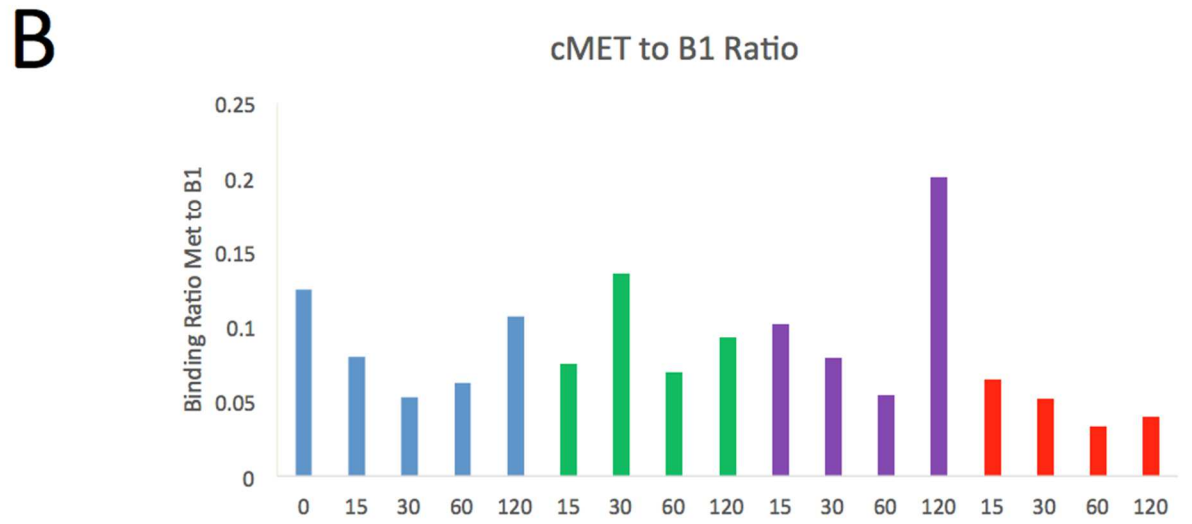

Figure S37. Effect of c-Met/HGF therapeutic antagonist NK4 on c-Met/b1 complex formation. Related to **Figure 6**. Cultured U87 cells were treated with 110 pM HGF and/or 110 nM of c-Met/HGF therapeutic antagonist NK4 for varying times. Immunoprecipitation forβ1 integrin followed by blotting of the precipitates revealed that HGF increased c-Met/b1 integrin complex formation at 30 minutes, corresponding to the time at which HGF induced c-Met phosphorylation. NK4 alone was associated with a delayed 120 minute spike in c-Met/b1 integrin complex formation, but adding NK4 to HGF suppressed HGF-induced complex formation.

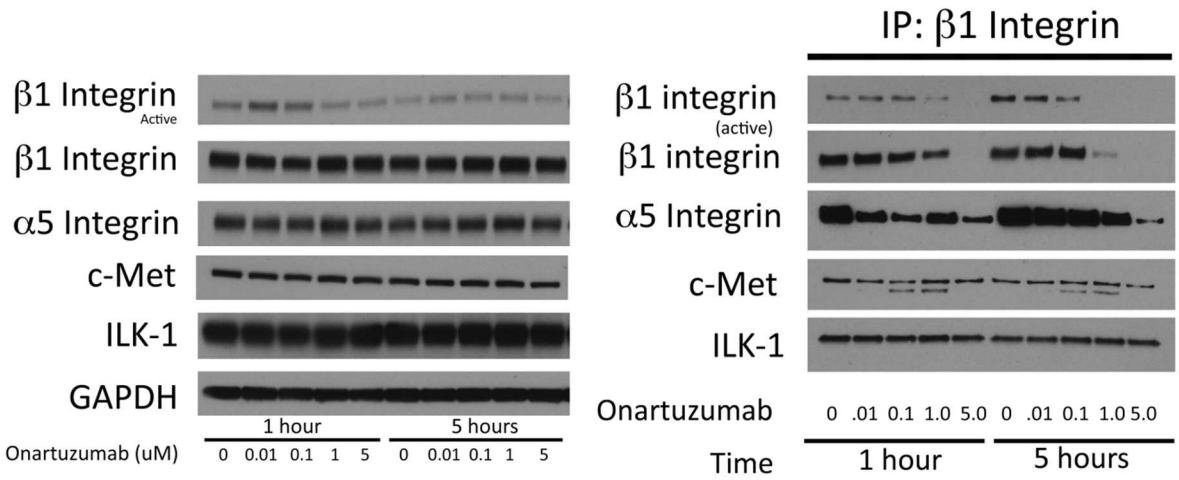

Figure S38. Effect of c-Met neutralizing antibody onartuzamab on c-Met/b1 complex formation. Related to **Figure 6**. Cultured U87 cells were treated with varying concentrations of c-Met neutralizing antibody onartuzamab for 1 and 5 hours. **(A)** Western blots of whole cell lysates from these cells revealed that onartuzamab reduced levels of activatedβ1 without affecting levels ofβ1 integrin detected with antibody ab52971 which reacts to an epitope spanning β1 amino acids 650-750, outside of the predicted area in β1 integrin that interacts with c-Met. **(B)** immunoprecipitation of these lysates with β1 integrin antibody ab7168 which binds extracellular β1 at an unknown epitope) revealed decreased binding of ab52971 to β1 integrin in the precipitates. This finding together with the whole cell lysate western blot result suggests that onartuzamab blocked the ability of ab7168 to detect its β1 integrin epitope, suggesting that ab7168's epitope falls in the β1 amino acids predicted to bind c-Met (amino acids 246-290). Similar results were observed when the IP was performed using ab24693 (not shown). Unfortunately, because ab52971 was the only antibody which produced a clean blot on the precipitates, an IP revealing the unchanged β1 integrin levels seen in the whole cell lysates could not be rendered, making it difficult to discern the impact of onartuzamab on c-Met/b1 binding. But the effect of onartuzamab on the ability of ab7168 and ab24693 to bind their β1 epitopes offered insight into c-Met/ β1 binding domains.

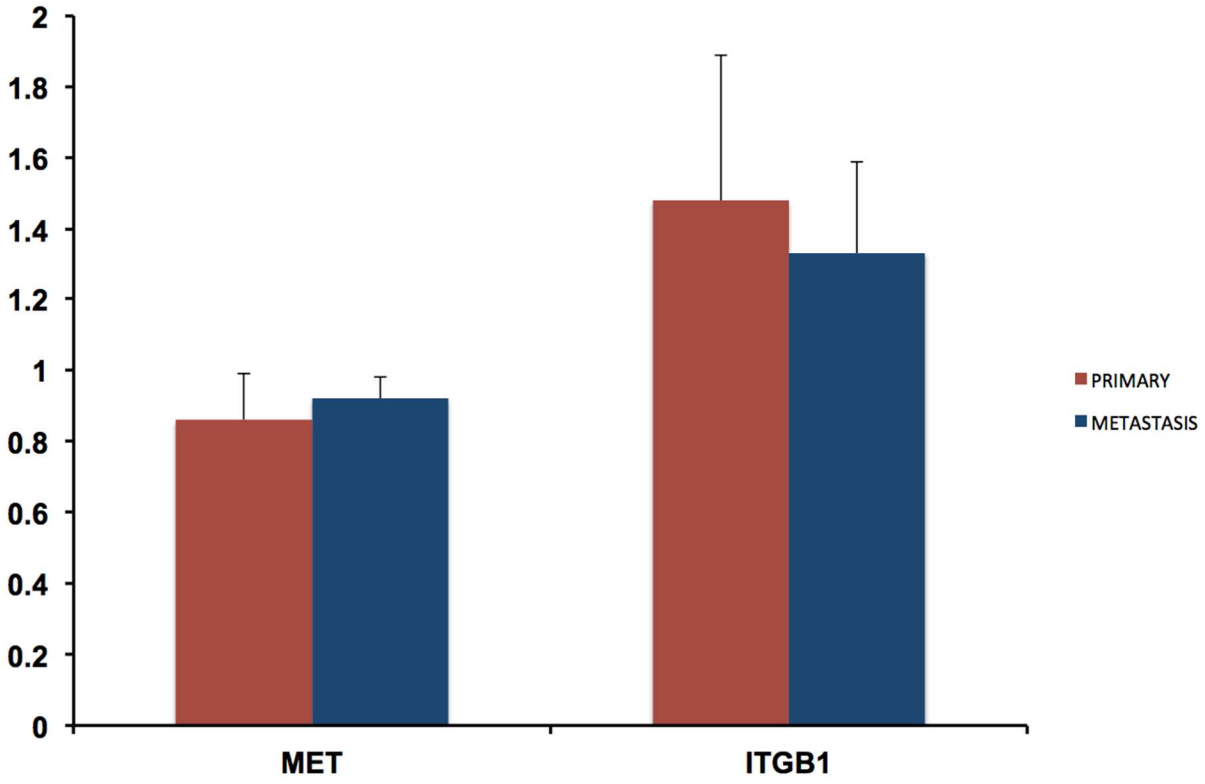

Figure S39. Microarray analysis of c-Met and b1 integrin expression in paired primary and metastatic breast cancer. Related to **Figure 7**. Analysis of publically deposited microarray data revealed no change in c-Met (P=0.3) or b1 integrin (P=0.4) expression in paired metastases and primary breast tumors (n=8 pairs).

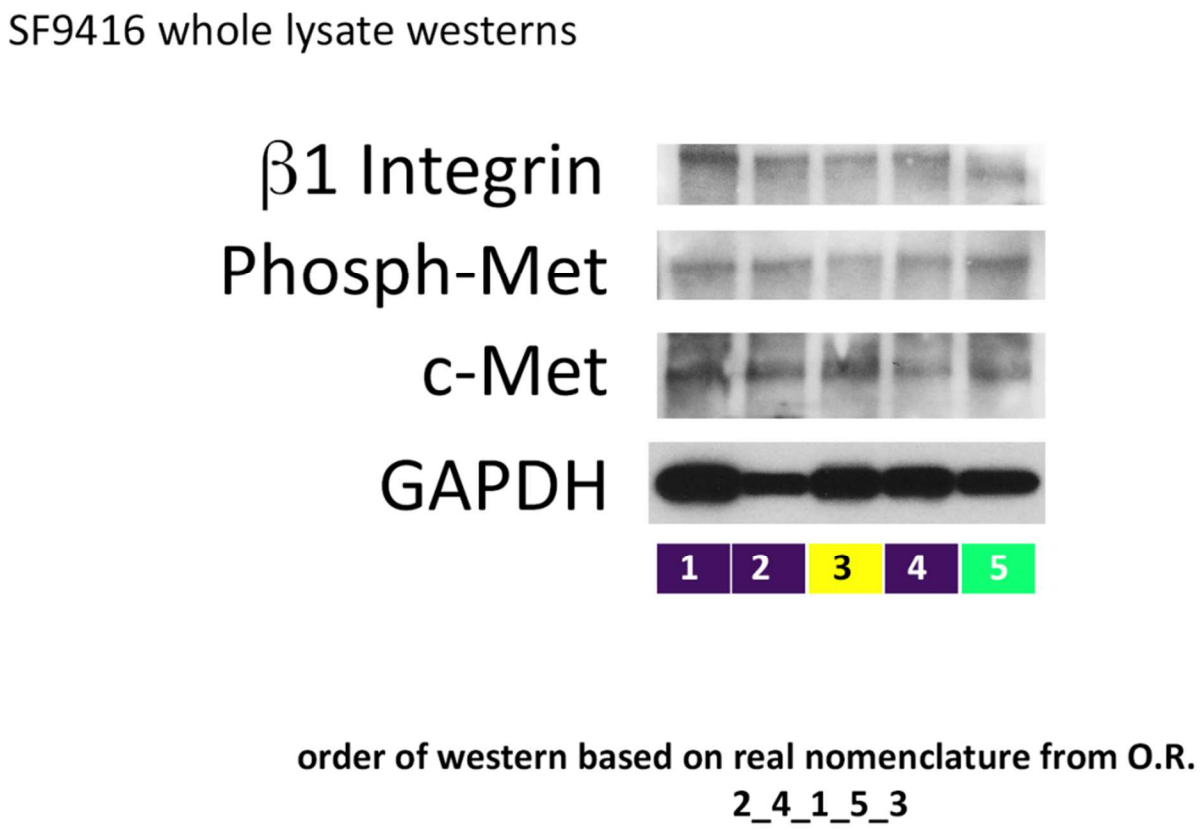

Figure S40. Western blots of lysates from site-directed biopsies of bevacizumab-resistant GBM. Related to **Figure 7*C***. Protein lysates from each location in **Figure 7*C*** were immunoblotted for the antigens shown here.

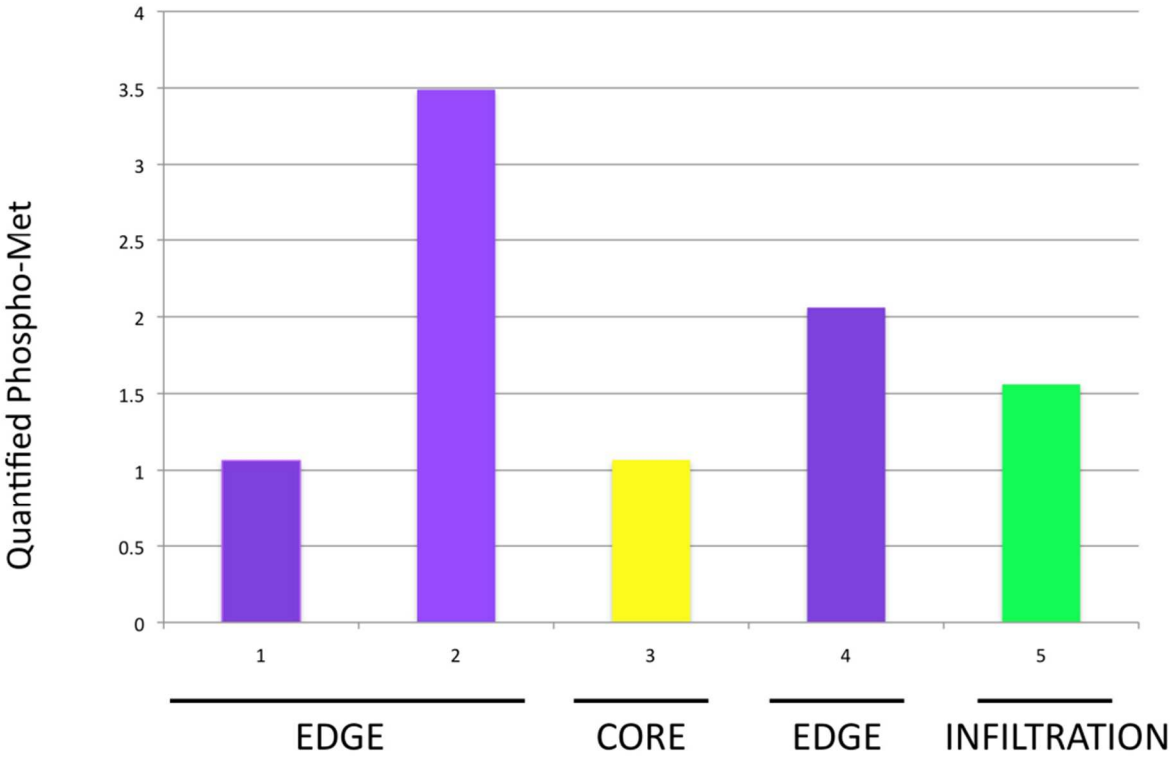

Figure S41. Quantified levels of phosphorylated c-Met bound to b1 integrin. Related to **Figure 7*C***. Protein lysates from each location in **Figure 7*C*** were used for immunoprecipitation with b1 integrin and immunoblotted for phosphorylated c-Met, quantified, and its levels shown.

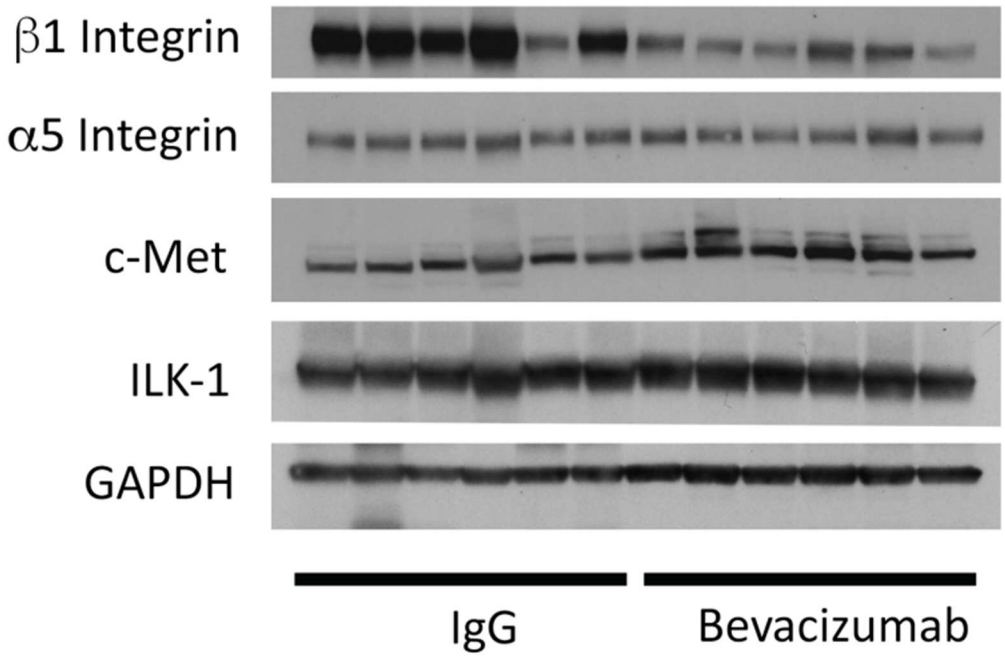

Figure S42. Western blots of lysates from patient-derived xenografts derived from bevacizumab-resistant GBM. Related to **Figure 8C.** Protein lysates from each xenograft in **Figure 8C** were immunoblotted for each of the antigens shown here. Note that bevacizumab reduced the ability of rabbit ab52971 to recognize β1 integrin in the whole cell lysates as occurred in **Figure S13** but no such issues occurred with the combination of antibodies used in the IP in **Figure 8C**.

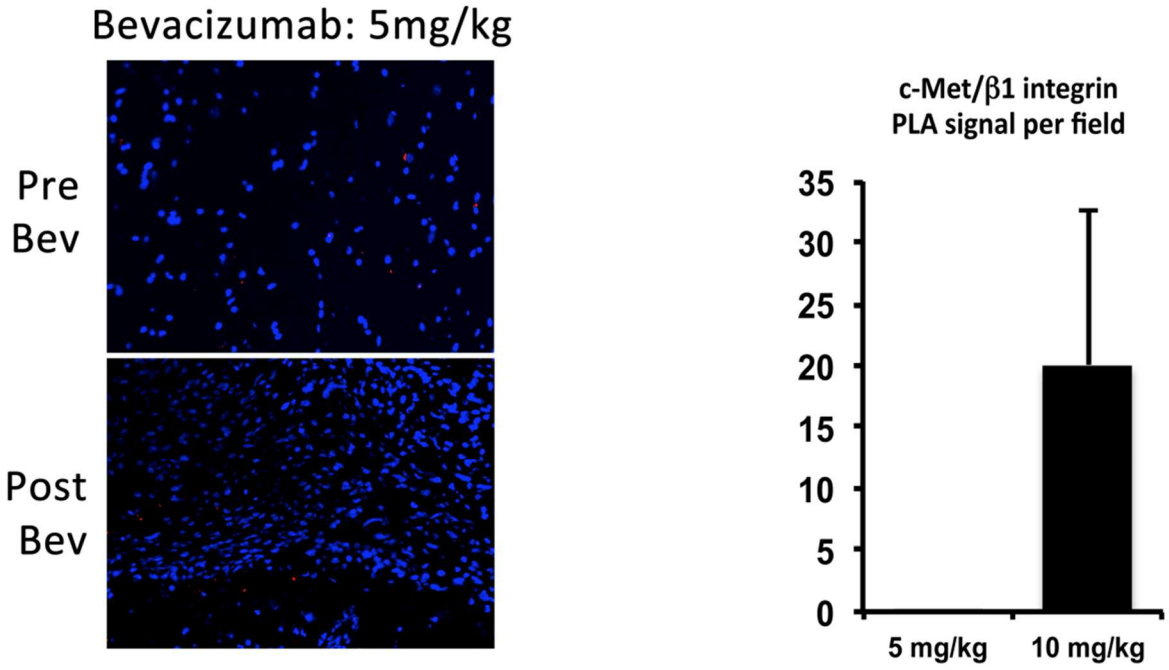

Figure S43. Complex formation occurs in a dose-dependent manner in bevacizumab-resistant patient GBM specimens. Related to **Figure 7**. PLA from a patient treated with 5 mg/kg bevacziumab twice weekly revealed decreased c-Met-b1 integrin complex relative to pre-treatment, unlike the increase seen at 10 mg/kg (same cases analyzed in **Figure 7*B***).

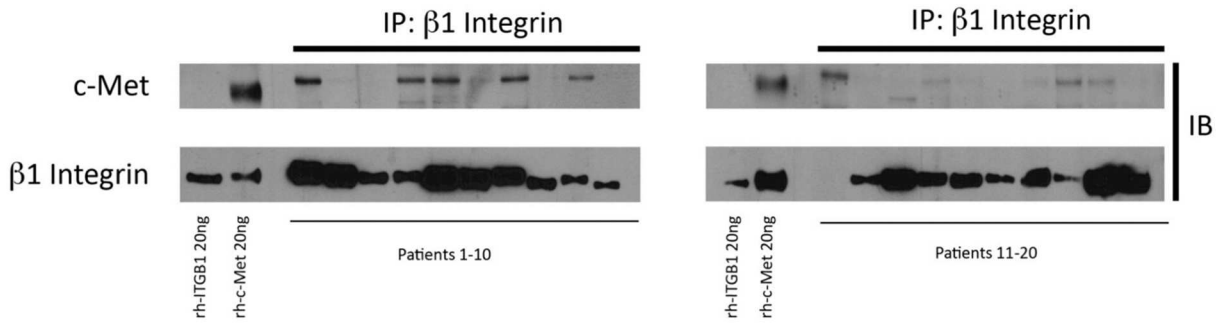

Figure S44. Immunoprecipitation to quantify c-Met/b1 integrin complex in protein lysates from newly diagnosed glioblastomas. Related to **Figure 7*F***. Band densitometries of c-Met pulled down in a b1 IP were normalized relative to the intensity of 20 ng of purified c-Met and then divided by the band intensity of b1 integrin in the IP normalized to the intensity of 20 ng of purified b1 integrin. The result, reflecting percentage of b1 integrin bound to c-Met, correlated inversely with survival as illustrated in **Figure 7*F***.

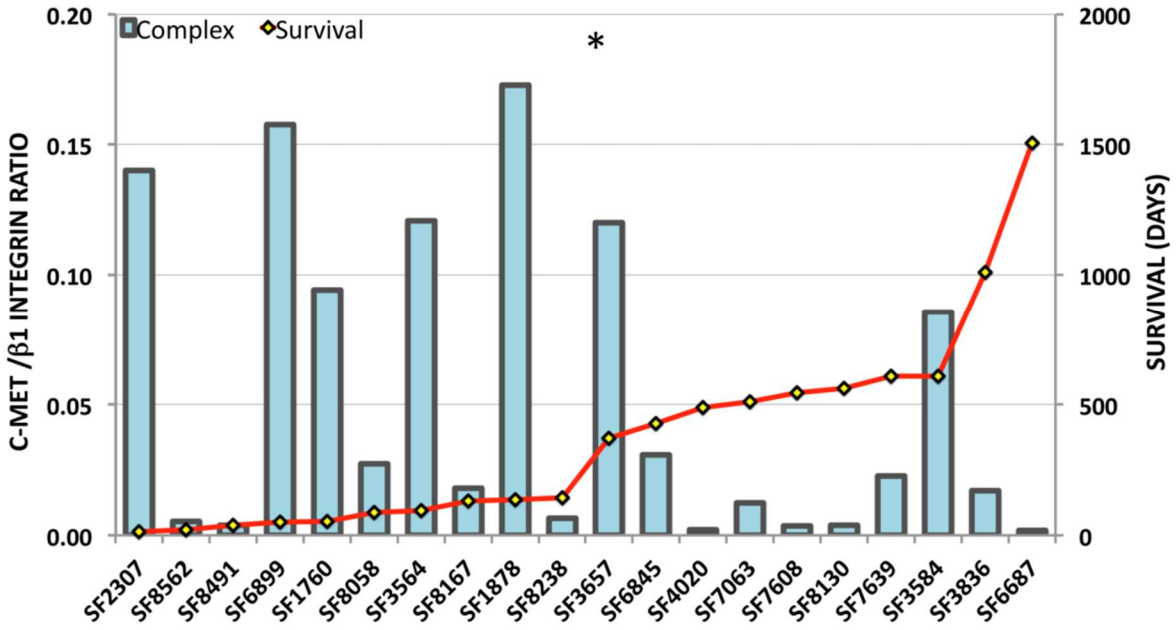

Figure S45. Immunoprecipitation to quantify c-Met/β1 integrin complex in protein lysates from newly diagnosed glioblastomas. Related to **Figure S44**. 20 GBM patients presented in order of increasing survival (right-hand vertical axis, red line graph) after diagnosis. Levels of cMet/β1 integrin protein complex from lysates of tumors resected at diagnosis, normalized to recombinant levels (IP results shown in **Figure S44**), are presented in blue bar graphs with complex levels noted on the left y-axis ($P<0.05$). * $P<0.05$; ** $P<0.01$ *** $P<0.001$.

APPENDIX B

SUPPLEMENTAL MATERIAL

Supplemental Table S1. Amino acids targeted by antibodies and engineered mutations used in this study.

Antibody (purpose)	**Human Antigen**	**Amino acids targeted**	**Technical issues arising with results**
Onartuzamab (therapeutic)	c-Met	328, 331, 337, 338 (Sema domain)	None
OS2966 (therapeutic)	β1 integrin	211 (β1 βI domain)	None
ab52971 (research)	β1 integrin	650-750	Bevacizumab, but not onartuzamab, affected ability of ab52971 to detect β1 integrin in cultured U87 cells.
ab7168 (research)	β1 integrin	Extracellular domain (exact amino acids unknown)	Onartuzamab, but not bevacizumab, affected ability of ab7168 to detect β1 integrin in cultured U87 cells
ab24693	β1 integrin	Exact amino acids unknown	Onartuzamab, but not bevacizumab, affected ability of ab24693 to detect β1 integrin in cultured U87 cells
Engineered Mutation	**cDNA**	**Amino acids targeted**	**Notes from results**
c-Met mutation #1	c-Met-FLAG	201-205	None
c-Met mutation #2	c-Met-FLAG	241-245	None
c-Met mutation #3	c-Met-FLAG	267-273	None
c-Met mutation #4	c-Met-FLAG	303-307	None
Proposed c-Met #5	c-Met-FLAG	348-359	Could not successfully alter this part of the sequence
β1 mutation #1	β1 integrin-HA	246	None
β1 mutation #2	β1 integrin-HA	283	None
β1 mutation #3	β1 integrin-HA	284	None
β1 mutation #4	β1 integrin-	287	None

β1 mutation #5	β1 integrin-HA	290	None

Supplemental Table S2. Antibodies used in these studies. Shown are antibodies used in their studies, their specific usage, species of origin, dilution used, and vendor/catalog number.

Antigen	Usage	Species	Dilution	Provider	Catalog #
β_1 Integrin (human)	Immunoprecipitation	Rabbit-Monoclonal	1:20	Abcam	ab52971
β_1 Integrin (human)	Immunoblotting	Rabbit-Monoclonal	1:1000	Abcam	ab51729
β_1 Integrin (human)	Immunoblotting	Mouse-Monoclonal	1:1000	Abcam	ab24693
β_1 Integrin (human)	Immunoblotting	Rabbit-Polyclonal	1:1000	Cell Signaling	4706
β_1 Integrin (human)	Immunohistochemistry(PLA)	Mouse-Monoclonal	1:100	Abcam	ab30394
c-Met (Human)	Immunoblotting	Rabbit-Monoclonal	1:1000	Abcam	ab51067
c-Met (Human)	Immunoblotting	Mouse Monoclonal	1:1000	Cell Signaling	3148
c-Met (Human)	Immunohistochemistry(PLA)	Rabbit-Monoclonal	1:250	Abcam	ab51067
p-MET (Tyr1234/1235; Human)	Immunoblotting	Rabbit-Monoclonal	1:1000	Cell Signaling	3126
ILK (human)	Immunoblotting	Rabbit-Monoclonal	1:1000	Cell Signaling	3856
α_5 Integrin (human)	Immunoblotting	Rabbit-Monoclonal	1:1000	Cell Signaling	54705
Thio-phosphate	Immunoblotting	Rabbit-Monoclonal	1:2000	Abcam	ab92570
AKT1 (human)	Immunoblotting	Rabbit-Monoclonal	1:1000	Cell Signaling	2138
Vimentin (human)	Immunohistochemistry	Rabbit-Monoclonal	1:250	Abcam	ab16700
Activated β1 integrin (human)	Immunoblotting	Mouse-Monoclonal	1:1000	Millipore	MAB20792
GAPDH	Immunoblotting	Mouse-Monoclonal	1:50,000	Millipore	MAB374
α1 integrin (human)	Immunoblotting	Mouse-Monoclonal	1:1000	Millipore	MAB1973

α2 integrin (human)	Immunoblotting	Rabbit Monoclonal	1:1000	Cell Signaling	13807
α3 integrin (human)	Immunoblotting	Rabbit	1:1000	Millipore	MAB1920
α4 integrin (human)	Immunoblotting	Rabbitt	1:1000	Cell Signaling	4600
α5 integrin (human)	Immunoblotting	Rabbitt	1:1000	Cell Signaling	4705
α6 integrin (human)	Immunoblotting	Rabbitt	1:1000	Cell Signaling	#3750
αV integrin (human)	Immunoblotting	Rabbitt	1:1000	Cell Signaling	4711
β3 integrin (human)	Immunoblotting	Rabbitt	1:1000	Cell Signaling	4702
β4 integrin (human)	Immunoblotting	Rabbitt	1:1000	Cell Signaling	4707
β5 integrin (human)	Immunoblotting	Rabbitt	1:1000	Cell Signaling	4708
Human VCAM	Immunoblotting	Rabbitt	1:1000	Cell Signaling	13662
Human Osteo-pontin	Immunoblotting	Rabbitt	1:1000	Abcam	ab8448
Human phosphorylated VEGFR2 (Tyr1175)	Immunoblotting	Rabbitt	1:1000	Cell Signaling	2478

Supplemental Table S3. Plasmids and constructs used in these studies. Shown are plasmids, their usage, and the source from which they were obtained.

Plasmid Name	Usage	Source
pRK5-ITGB1	Used as source cDNA to create integrin β_1 PCR fragments for cloning	Addgene®
pENTR-D-TOPO-cMET	Used as source cDNA to amplify *MET* PCR fragments	Addgene®
pLVX-Het1-DmrC	Part of Clontech Lenti-X iDimerize™ plasmid kit	Clontech®
pLVX-Het2-DmrA	Part of Clontech Lenti-X iDimerize™ plasmid kit	Clontech®
pCR4-Blunt-TOPO	Topoisomerase cloning of blunt PCR products	Invitrogen®
pCR4- β_1-HA	HA-tagged integrin β_1 cDNA	Author Generated
pCR4-cMET-His	6xHis-tagged *MET* cDNA	Author Generated
pLVX-Het1-β_1-HA	HA-tagged integrin β_1 lentiviral construct for constitutive expression	Author Generated
pLVX-Het1-β_1	Integrin β_1 lentiviral construct for constitutive expression	Author Generated
pLVX-Het2-cMET	Lentiviral construct for stable expression of DmrA-fused *MET*	Author Generated
pLVX-Het2-cMET-His	Lentiviral construct for stable expression of DmrA-fused *MET* with 6xHis tag	Author Generated
pLVX-Het2-cMET-FLAG	Lentiviral construct for stable expression of DmrA-fused *MET-FLAG*	Author Generated

Supplemental Table S4. Primers used in the studies. Shown are forward and reverse primers, their usage, and their sequences.

Primer Name	Use	Sequence 5' to 3'
B1(NotI)Fw	Amplification of ITGB1 cDNA from pRK5-Beta1 conserving in-frame status with pLVX-Het1-DmrC at the 3' MCS and NotI restriction site	CTCGATTGCGGCCGCATGAATTTACAACCAATTTTCTG
B1(BamHI) RV	Amplification of ITGB1 cDNA from pRK5-Beta1 conserving in-frame status with pLVX-Het1-DmrC at the 3' MCS and BamHI restriction site	GAAATTAGGATCCTTTTCCCTCATACTTCGGAT
B1(BamHI)-HA RV	Amplification of ITGB1 cDNA from pRK5-Beta1 conserving in-frame status with pLVX-Het1-DmrC at the 3' MCS with the addition of hemagglutinin tag sequence and BamHI restriction site.	GAAATTAGGATCCAGCGTAATCTGGAACATCGTATGGGTATTTTCCCTCATACTTCGGAT
cMET(NotI)-FW	Amplification of cMET cDNA from pENTR-cMET conserving in-frame status with pLVX-Het2-DmrA at the 3' MCS with the addition of NotI restriction site.	GCCGACGGCGGCCGCATGAAGGCCCCCGCTGTGCT
cMET(NotI)-RV		GTCATCAGCGGCCGCTTGATGTCTCCCAGAAGGAGGCT
cMET(NotI)-His RV	Amplification of cMET cDNA from pENTR-cMET conserving in-frame status with pLVX-Het2-DmrA at the 3' MCS with the addition of 6xHis amino acid sequence and NotI restriction site.	GTCATCAGCGGCCGCTGTGGTGGTGGTGGTGGTGTGATGTCTCCCAGAAGGAGGCT
cMET-pLVX2-FW	Amplification of cMET cDNA with primers containing 15bps of pLVX-Het2-DmrC arms for Gibson assembly at the 3' MCS utilizing NotI digestion.	AGCTTCTAAAACTGGAAAGCATGAAGGCCCCCGCTGTGCT
cMET-pLVX2-RV		GGCGGTCATACGTAGGATGATGTCTCCCAGAAGGAGGCT
FKBP-cMET_PCR7-FW	Amplification of fusion region between FKBP(Het2-DmrA)-cMET - forward primer in FKBP and reverse primer in cMET such that amplification only occurs in cells with the iDimerize™ system, used to quantify metastatic breast cancer cells expressing the iDimerize™ system in the lungs after tail vein injection of these cells into mice.	CCACATGCCACTCTCGTCTTC
FKBP-cMET_PCR7-RV		GTTTCCGCGGTGAAGTTGG
cMet_Mut1_FW	Mutagenesis primers designed using NEB BaseChanger software to replace specified strings of amino acids (**Supplemental Table S1**) to alanine residues in pLVX-Het-MET-FLAG.	AGCAGCATTCCCAGATCATCCATTG
cMet_Mut1_RV		GCTGCTGCGGTATTGCCTACAAAGAAG
cMet_Mut2_FW		AGCAGCACCCATTAAGTATGTCCATG

cMet_Mut2_RV		GCTGCTGCCTCAGGTAAAACATCAATG
cMet_Mut3_FW		AGCAGCAGCATTTCACACAAGAATAATCAGGTTC
cMet_Mut3_RV		GCTGCTGCTGCCCTTTGGACCGTCAAGAAG
cMet_Mut4_FW		AGCAGCATCCACAAAGAAGGAAGTG
cMet_Mut4_RV		GCTGCTGCTTCTGTGAGAATACACTC
cMet_Mut5_FW		GCAGCAGCAGCAGCAGCATCTGCCATGTGTGCATTC
cMet_Mut5_RV		TGCTGCTGCTGCTGCTGCTGCGAACACCCCGAAAAG
B1_Mut1_FW	Mutagenesis primers designed using NEB BaseChanger software to create point mutations in pLVX-Het1-β_1-HA, replacing specified amino acids (**Supplemental Table S1**) with alanine residues.	TGGAAATTTGGCATCTCCAGAAGGTG
B1_Mut1_RV		GATATGCGCTGTTTTCCAAC
B1_Mut2_FW		TGCCGGGTTTGCATTTGCTGGAGATGG
B1_Mut2_RV		TCTGTGGAAAACACCAGC
B1_Mut3_FW		CGGGTTTCACGCAGCTGGAGATG
B1_Mut3_RV		GCATCTGTGGAAAACACC
B1_Mut4_FW		CTTTGCTGGAGCAGGGAAACTTGG
B1_Mut4_RV		TGAAACCCGGCATCTGTG
B1_Mut5_FW		AGATGGGAAAGCAGGTGGCATTGTTTTACC
B1_Mut5_RV		CCAGCAAAGTGAAACCCG

SUPPLEMENTARY METHODS

Chamber Slides

We plated 10,000 U87 or MDA-MB-231 cells with or without the iDimerize system per well in chamber slides (Labtek by Thermo, #177402). Cells were incubated for 24 hours to allow them to adhere, after which they were treated with or without 500 nM A/C ligand for 12 hours. Following completion of PLA per protocol from main paper methods, cells were then stained with 2.5 μg/mL phalloidin (Sigma #P5282) in TNB buffer (100 mM Tris-HCl pH 7.5, 200 mM NaCl, 1% BSA) for one hour, after which the stain was washed and slides were Fluoromount-DAPI mounted.

Morphology Assessment.

Transduced MDA-MB-231 or U87 cells were plated on fibronectin coated (10 μg/mL for one hour) 8-well chamber slides and induced with 500 nM AP219667 (Takara Bio, 635055) (24 hrs). Cells were fixed with 3.7% paraformaldehyde (15 min), PBS washed, and blocked with 1% BSA (1 hr), permeabilized with 0.1% Triton-X 100 in PBS (10 min), washed three times, and incubated with Alexa488-conjugated phalloidin (Life Technologies, A12379) (30 mins). The stain was washed and slides were Fluoromount-DAPI mounted. ImageJ Form Factor plugin was used

to calculate circularity shape factor (isoperimetric quotient), defined as $4X\pi X(\text{area})/(\text{perimeter})^2$ (13). The circularity shape factor of a circle is 1, and becomes much less than one for a starfish.

Survival Assays.

To assess cell survival in hypoxia and nutrient (serum) deprivation. U87-iDimerize-c-Met-β1 cells were plated on 100 mm dishes at 500K cells/dish. Cells were allowed to adhere over night. Plates were incubated in DMEM F12 high glucose media with 10% FBS for 2 hours. Media was aspirated and each plate was washed with 10mL PBS twice. Appropriate media was added to each plate with or without FBS (for nutrient deprivation). 500 nM A/C ligand was added to complete or serum-free media for half of the dishes. Cells were incubated in normoxic or hypoxic (1% oxygen) incubators for 24 hours, then media was aspirated gently, and washed with 5 mL PBS. Light microscopy was used to image six sections of each plate at the same coordinates at 10X. De-identified images were loaded into ImageJ. Cells at 24 hours were counted per each image using the Cell Counter ImageJ plugin and averaged.

qPCR

Tissue digestion buffer was made with RPMI 1640 with 10% FBS and 10 mg/mL of both DNAse and Collagenase IV. Left lobe of the lung was severed and minced in petri dish with 300 μL of

added digestion buffer. Minced lung tissue was transferred to 7 mL of digestion buffer and incubated with rotation at 37°C for 40 minutes. Cell suspension was filtered through a 40 micron filter and washed once with PBS. Cells were pelleted and treated with 1X RBC lysis buffer to remove red blood cell contamination. Cells were then washed twice and pelleted down. The cell pellet was then resuspended in Buffer ATL (Qiagen) and DNA was extracted from the cells following manufacturer's protocol for DNeasy Blood and Tissue kit. DNA concentration was measured using a Take3 microspot plate and a working stock of all samples at 10 ng/μL was created to allow for identical DNA input in each reaction. Quantitative PCR was carried out using Power Syber Green Master Mix and amplified using an Applied Biosystems StepOne Real-Time PCR cycler following the recommended guidelines for Syber: 95°C for 10 minutes, followed by 40 cycles of 95°C for 15 seconds and 60°C for 1 minute. Samples were prepared with three technical replicates for each primer pair and used Actb as a control housekeeping gene. Each AC-treated sample was normalized to both Actb and its paired posit-treatment time point, with fold change calculated using the 2^(-ΔΔCt) method.

Site-directed mutagenesis

Addgene plasmid stocks were used to obtain constructs containing ITGB1 and MET (#16042 and #31786 respectively). Primers were created to amplify cMet from its vector, with hanging

sequences added to attach a FLAG (DYKDDDDK) tag to the 3' end of the gene, as well as to create *NotI* digestion sites at both 5' and 3' ends. This process was repeated for β1, adding an EcoRI site to the 5' end and an HA (YPYDVPDYA) tag and XbaI sequence to the 3' end. These amplified sequences were cloned into separate pLVX-IRES-Puro empty vectors, creating pLVX-cMet-FLAG and pLVX-Beta1-HA. For β1 integrin, the Rosetta ALA scanning method (21, 44) was used to predict changes in delta-delta-G (the higher the better) when altering individual residues, with the following residues chosen to alter to alanine based on their high delta-delta-G values: ASP 226 (1.71), HIS 263 (1.76), PHE 264 (2.77), ASP 267 (3.45), and LEU 270 (2.41). For c-Met, the PyMOL model suggested that the loops atop its propeller structure make contact with β1, so we mutated these loop residues: 201-205, 241-245, 267-273, 303-307, and 348-359. All positions were converted from their original sequence to 'GCA' in order to obtain single/sequential alanine residues. Mutagenesis PCR was performed using the NEB Q5 Site Directed Mutagenesis Kit (E0554S), following manufacturer's protocol and utilizing NEB BasecChanger™ to create mutagenic primers (**Supplemental Table S4**). Mutations were confirmed by miniprep and sequencing of selected colonies before growth of larger stocks for transfection into HEK cells.

Immunofluorescence

Frozen tissue sections were stained as previously described (5). For primary antibodies, we used rabbit monoclonal anti-vimentin (1:250, Abcam, ab16700) and Alexa594 conjugated isolectin GS-IB_4 (1:250, Life Technologies, I21413). For secondary antibody, we used donkey anti-rabbit Alexa 488 (1:250, Life Technologies, A21206).

Far-Western Blotting

Lysates were first harvested into radio immunoprecipitation buffer (RIPA) containing 20mM Tris-HCl (pH 7.5), 150mM NaCl, 1mM Na_2EDTA, 1% NP-40, 1% sodium deoxycholate, 2.5mM sodium pyrophosphate, 1mM beta-glycorophosphate, 1mM Na_3VO_4, 1μg/ml leupeptin (RIPA Buffer, 10x, Cell Signaling, Technology, MA; #9806) and one tablet each of PhoStop and Complete Mini (Roche, IN). Removal of insoluble materials was achieved by centrifugation at 14,000 rpm for 20 min at 4°C. Protein concentration was then determined using the bicinchronic acid (BCA) assay (Pierce Biotechnology, Rockford, IL). Resulting lysates were electrophoresed on an SDS-PAGE gel. After transfer the PVDF blot was prepared for far-western probing as described by Wu et al. (16). Briefly, the PVDF membrane was treated with decreasing amounts of Guanidine HCl to denature and then renature the proteins within the membrane. The blots were then incubated for variable time with recombinant extracellular (SINO Biologicals; #10692-

H08H-5) or intracellular c-Met (Abcam, ab42612) and then probed for the histidine repeat tag using the HisProbe™-HRP kit (Pierce Biotechnology, IL; #15165).

Dot Blotting

One µg of the following proteins were spotted onto a PVDF membrane: rh-α4-integrin (Origene Technologies, #TP314408), rh-α5-integrin (Novoprotein Scientific, #C478), rh-β1-integrin (Origene Technologies, #TP303818), and rh-c-Met (Abcam, cat. #ab42612). PVDF membranes were completely dried at room temperature before blocking with 5% non-fat dry milk. Membranes were then probed with fibronectin-GST (Kerafast, cat. #EUR108) in protein binding buffer described by Wu et al. (16) overnight at 4ºC. Resulting membranes were detected using HRP-conjugated GST antibody (Cell Signaling, #5474) using radiographic film.

Biotinylation of Cell Proteins

To biotinylate all extracellular portions, U87 cells were treated with a biotinylation kit (Life Technologies, #21115) per protocol, after which cell lysates were incubated with avidin-conjugated beads (Life Technologies) and eluted. The non-biotinylated proteins in the eluant and the biotinylated proteins bound to beads were then run on a gel and blotted with HRP-conjugated streptavidin (Perkin Elmer, #FP1047) to confirm the effectiveness of the biotinylation

reaction. The non-biotinylated proteins in the eluant then underwent immunoblotting for β1 and c-Met, along with β1 and c-Met immunoprecipitation for both proteins followed by blotting of the precipitant for β1 and c-Met.

Adhesion Assay

96 well plates were coated with 20 μg/mL fibronectin overnight at 4°C. After blocking with blocking buffer (0.5% BSA in DMEM), plates were washed with washing buffer (0.1% BSA in DMEM), and then chilled. Tumor cells (50 μL at 4 X 10^5 cells/mL) were pre-incubated with varying concentrations of HGF, then added to wells and incubated for 30 minutes at 37°C. Plates were shaken at 2000 rpm for 10-15 seconds, washed 3 times in washing buffer, fixed with 4% paraformaldehyde for 10 minutes at room temperature, washed with washing buffer, stained with crystal violet for 10 minutes, washed with water, dried upside down, incubated in 2% SDS for 30 minutes at room temperature, and absorbance was read at 590 nm.

Kinase Assay

Recombinant human ILK (400 ng used with c-Met, 0, 100, 200, 300, and 400 ng used with ILK; Abcam, MA, USA; ab83119) and/or recombinant target protein (1.5 μL of 0.2 mg/mL recombinant intracellular c-Met amino acids 956-1390; Abcam ab42612 or 300 nM of unactive

human AKT-1; SignalChem, cat#A16-14G). 1 μL of 10x TBS was added to each reaction, followed by 1 μL of 50 mM of $MgCl_2$ or 100mM $MnCl_2$. Each reaction then received 1 μL of 5 mM ATPγS (Boehringer-Mannheim). Nuclease-free water was added to each reaction to bring it to a final volume of 10 μL. The reactions were then incubated at room temperature under gentle agitation for 1 hour. Each reaction was then quenched with 2.5 μL of EDTA for a total of 5 minutes. This was followed by the addition of 0.5 μL of 12 mg/mL PNBM (Abcam ab138910) to all three reactions and incubated for 45 minutes. During this time 1x loading sample was made by adding 4.3 μL of 4X LDS NuPage loading buffer to 0.7 μL of DTT stock (Cell Signaling). Loading buffer was added to each sample. The samples were then run on a standard immunoblotting assay as described below.

Drug treatment of cultured cells

OS2966 (Oncosynergy), ornatuzamab (Genentech), and NK4 (K. Matsumoto, Kringle Pharma) were kindly provided by manufacturing companies through MTAs. Cpd 22 (Calbiochem) was dissolved in DMSO. U87 cells were plated in 10 cm dishes, allowed to adhere overnight, serum starved for 2 hours, and then treated with drugs in serum-free media at concentrations and time points specified in figure legends. Lysates were then harvested for western blots and IPs.

Human Tissue Procurement and Clinical Data

Site-directed tumor biopsies were performed utilizing a 3-dimensional intraoperative navigation system. All other human tissue was obtained through the UCSF breast and brain tumor research center tissue banks, who acquired the tissue through informed consent. Patient survival data was obtained through the available clinical databases at UCSF and analyzed as described in the statistics section.

Deposited microarray analysis

We extracted archived microarray data (GEO accession number GSE79446) containing comparative genomic hybridization analysis on 8 sets of paired primary and metastatic breast tumor samples (45). That analysis was performed on paraffin-embedded tumor chunks prepped for array labelling using Agilent Oligonucleotide Array-Based CGH for Genomic DNA Analysis kit, with probes hybridized to the Human Whole Genome 8x60k chip. We downloaded the data for each sample, displayed as the log (fold change), with fold change for each gene reported as the value of the gene of interest in the sample divided by the value of the gene of interest in the reference genome. This log (fold change) value was extracted for Beta-1 (ITGB1) and c-Met (MET). All primary tumor values for each gene were converted to raw fold change and averaged to create a single primary fold change value for each of the two genes. This process was

repeated for the eight metastatic tumor samples.

References

1. Barrow-McGee R*, et al.* (2016) Beta 1-integrin-c-Met cooperation reveals an inside-in survival signalling on autophagy-related endomembranes. *Nat Commun* 7:11942.
2. Mitra AK*, et al.* (2011) Ligand-independent activation of c-Met by fibronectin and alpha(5)beta(1)-integrin regulates ovarian cancer invasion and metastasis. *Oncogene* 30(13):1566-1576.
3. Gupta GP & Massague J (2006) Cancer metastasis: building a framework. *Cell* 127(4):679-695.
4. Bergers G & Hanahan D (2008) Modes of resistance to anti-angiogenic therapy. *Nat Rev Cancer* 8(8):592-603.
5. Carbonell WS, Delay M, Jahangiri A, Park CC, & Aghi MK (2013) beta1 Integrin Targeting Potentiates Antiangiogenic Therapy and Inhibits the Growth of Bevacizumab-Resistant Glioblastoma. *Cancer research* 73(10):3145-3154.
6. Jahangiri A*, et al.* (2013) Gene expression profile identifies tyrosine kinase c-Met as a targetable mediator of antiangiogenic therapy resistance. *Clinical Cancer Research* 19(7):1773-1783.
7. DeLay M*, et al.* (2012) Microarray analysis verifies two distinct phenotypes of glioblastomas resistant to antiangiogenic therapy. *Clinical cancer research : an official journal of the American Association for Cancer Research* 18(10):2930-2942.
8. Paez-Ribes M*, et al.* (2009) Antiangiogenic therapy elicits malignant progression of tumors to increased local invasion and distant metastasis. *Cancer cell* 15(3):220-231.
9. Kreisl TN*, et al.* (2009) Phase II trial of single-agent bevacizumab followed by bevacizumab plus irinotecan at tumor progression in recurrent glioblastoma. *J Clin Oncol* 27(5):740-745.
10. Park CC, Zhang HJ, Yao ES, Park CJ, & Bissell MJ (2008) Beta1 integrin inhibition dramatically enhances radiotherapy efficacy in human breast cancer xenografts. *Cancer research* 68(11):4398-4405.
11. Gupta P, Adkins C, Lockman P, & Srivastava SK (2013) Metastasis of Breast Tumor Cells to Brain Is Suppressed by Phenethyl Isothiocyanate in a Novel In Vivo Metastasis Model. *PLoS One* 8(6):e67278.
12. Muthuswamy SK, Gilman M, & Brugge JS (1999) Controlled dimerization of ErbB receptors provides evidence for differential signaling by homo- and heterodimers. *Molecular and cellular biology* 19(10):6845-6857.

13. Levi-Schaffer F, Slovik D, Armetti L, Pickholtz D, & Touitou E (2000) Activation and inhibition of mast cells degranulation affect their morphometric parameters. *Life Sci* 66(21):PL283-290.
14. Herve MA*, et al.* (2008) Overexpression of vascular endothelial growth factor 189 in breast cancer cells leads to delayed tumor uptake with dilated intratumoral vessels. *The American journal of pathology* 172(1):167-178.
15. Woolard J*, et al.* (2004) VEGF165b, an inhibitory vascular endothelial growth factor splice variant: mechanism of action, in vivo effect on angiogenesis and endogenous protein expression. *Cancer research* 64(21):7822-7835.
16. Wu Y, Li Q, & Chen XZ (2007) Detecting protein-protein interactions by Far western blotting. *Nat Protoc* 2(12):3278-3284.
17. Fukuda K, Knight JD, Piszczek G, Kothary R, & Qin J (2011) Biochemical, proteomic, structural, and thermodynamic characterizations of integrin-linked kinase (ILK): cross-validation of the pseudokinase. *J Biol Chem* 286(24):21886-21895.
18. Nagae M*, et al.* (2012) Crystal structure of alpha5beta1 integrin ectodomain: atomic details of the fibronectin receptor. *J Cell Biol* 197(1):131-140.
19. Rickert KW*, et al.* (2011) Structural basis for selective small molecule kinase inhibition of activated c-Met. *J Biol Chem* 286(13):11218-11225.
20. Xia W & Springer TA (2014) Metal ion and ligand binding of integrin alpha5beta1. *Proc Natl Acad Sci U S A* 111(50):17863-17868.
21. Kortemme T, Kim DE, & Baker D (2004) Computational alanine scanning of protein-protein interfaces. *Sci STKE* 2004(219):pl2.
22. Clark AJ*, et al.* (2011) Neurosurgical management and prognosis of patients with glioblastoma that progress during bevacizumab treatment. *Neurosurgery*.
23. Erdogan B*, et al.* (2017) Cancer-associated fibroblasts promote directional cancer cell migration by aligning fibronectin. *J Cell Biol* 216(11):3799-3816.
24. Takeuchi H*, et al.* (2003) c-MET expression level in primary colon cancer: a predictor of tumor invasion and lymph node metastases. *Clinical cancer research : an official journal of the American Association for Cancer Research* 9(4):1480-1488.
25. Carbonell WS, Ansorge O, Sibson N, & Muschel R (2009) The vascular basement membrane as "soil" in brain metastasis. *PLoS One* 4(6):e5857.
26. Lu KV*, et al.* (2012) VEGF inhibits tumor cell invasion and mesenchymal transition through a MET/VEGFR2 complex. *Cancer cell* 22(1):21-35.
27. Klemke RL, Yebra M, Bayna EM, & Cheresh DA (1994) Receptor tyrosine kinase signaling required for integrin alpha v beta 5-directed cell motility but not adhesion on vitronectin. *J Cell Biol* 127(3):859-866.

28. Howe A, Aplin AE, Alahari SK, & Juliano RL (1998) Integrin signaling and cell growth control. *Current opinion in cell biology* 10(2):220-231.
29. Nagano M, Hoshino D, Koshikawa N, Akizawa T, & Seiki M (2012) Turnover of focal adhesions and cancer cell migration. *Int J Cell Biol* 2012:310616.
30. English BC, Price DK, & Figg WD (2009) VEGF inhibition and metastasis: possible implications for antiangiogenic therapy. *Cancer Biol Ther* 8(13):1214-1225.
31. Dai Y & Siemann DW (2012) Constitutively active c-Met kinase in PC-3 cells is autocrine-independent and can be blocked by the Met kinase inhibitor BMS-777607. *BMC Cancer* 12:198.
32. Pines G, Kostler WJ, & Yarden Y (2010) Oncogenic mutant forms of EGFR: lessons in signal transduction and targets for cancer therapy. *FEBS Lett* 584(12):2699-2706.
33. Schiller HB, Friedel CC, Boulegue C, & Fassler R (2011) Quantitative proteomics of the integrin adhesome show a myosin II-dependent recruitment of LIM domain proteins. *EMBO Rep* 12(3):259-266.
34. Legate KR, Montanez E, Kudlacek O, & Fassler R (2006) ILK, PINCH and parvin: the tIPP of integrin signalling. *Nat Rev Mol Cell Biol* 7(1):20-31.
35. Wickstrom SA*, et al.* (2010) Integrin-linked kinase controls microtubule dynamics required for plasma membrane targeting of caveolae. *Dev Cell* 19(4):574-588.
36. Hannigan GE, McDonald PC, Walsh MP, & Dedhar S (2011) Integrin-linked kinase: not so 'pseudo' after all. *Oncogene* 30(43):4375-4385.
37. Hannigan G, Troussard AA, & Dedhar S (2005) Integrin-linked kinase: a cancer therapeutic target unique among its ILK. *Nat Rev Cancer* 5(1):51-63.
38. de Groot JF (2011) High-dose antiangiogenic therapy for glioblastoma: less may be more? *Clinical cancer research : an official journal of the American Association for Cancer Research* 17(19):6109-6111.
39. Wen PY*, et al.* (2009) A Phase 2 Study of XL184, an Inhibitor of Met, VEGFR2, and RET, in patients with progressive glioblastoma multforme. *Society for Neuro-Oncology Annual Meeting*.
40. Stupp R*, et al.* (2014) Cilengitide combined with standard treatment for patients with newly diagnosed glioblastoma with methylated MGMT promoter (CENTRIC EORTC 26071-22072 study): a multicentre, randomised, open-label, phase 3 trial. *Lancet Oncol* 15(10):1100-1108.
41. Liang CC, Park AY, & Guan JL (2007) In vitro scratch assay: a convenient and inexpensive method for analysis of cell migration in vitro. *Nat Protoc* 2(2):329-333.
42. Shatsky M, Nussinov R, & Wolfson HJ (2004) A method for simultaneous alignment of multiple protein structures. *Proteins* 56(1):143-156.

43. Gront D*, et al.* (2012) Assessing the accuracy of template-based structure prediction metaservers by comparison with structural genomics structures. *J Struct Funct Genomics* 13(4):213-225.
44. Kortemme T & Baker D (2002) A simple physical model for binding energy hot spots in protein-protein complexes. *Proc Natl Acad Sci U S A* 99(22):14116-14121.
45. Manso L*, et al.* (2016) Analysis of Paired Primary-Metastatic Hormone-Receptor Positive Breast Tumors (HRPBC) Uncovers Potential Novel Drivers of Hormonal Resistance. *PLoS One* 11(5):e0155840.

Publishing Agreement

It is the policy of the University to encourage the distribution of all theses, dissertations, and manuscripts. Copies of all UCSF theses, dissertations, and manuscripts will be routed to the library via the Graduate Division. The library will make all theses, dissertations, and manuscripts accessible to the public and will preserve these to the best of their abilities, in perpetuity.

I hereby grant permission to the Graduate Division of the University of California, San Francisco to release copies of my thesis, dissertation, or manuscript to the Campus Library to provide access and preservation, in whole or in part, in perpetuity.

Author Signature  Date 05/29/2018